STRUCTURE AND REACTIVITY OF GAS PHASE BIMETALLIC CLUSTERS TOWARDS CO_2

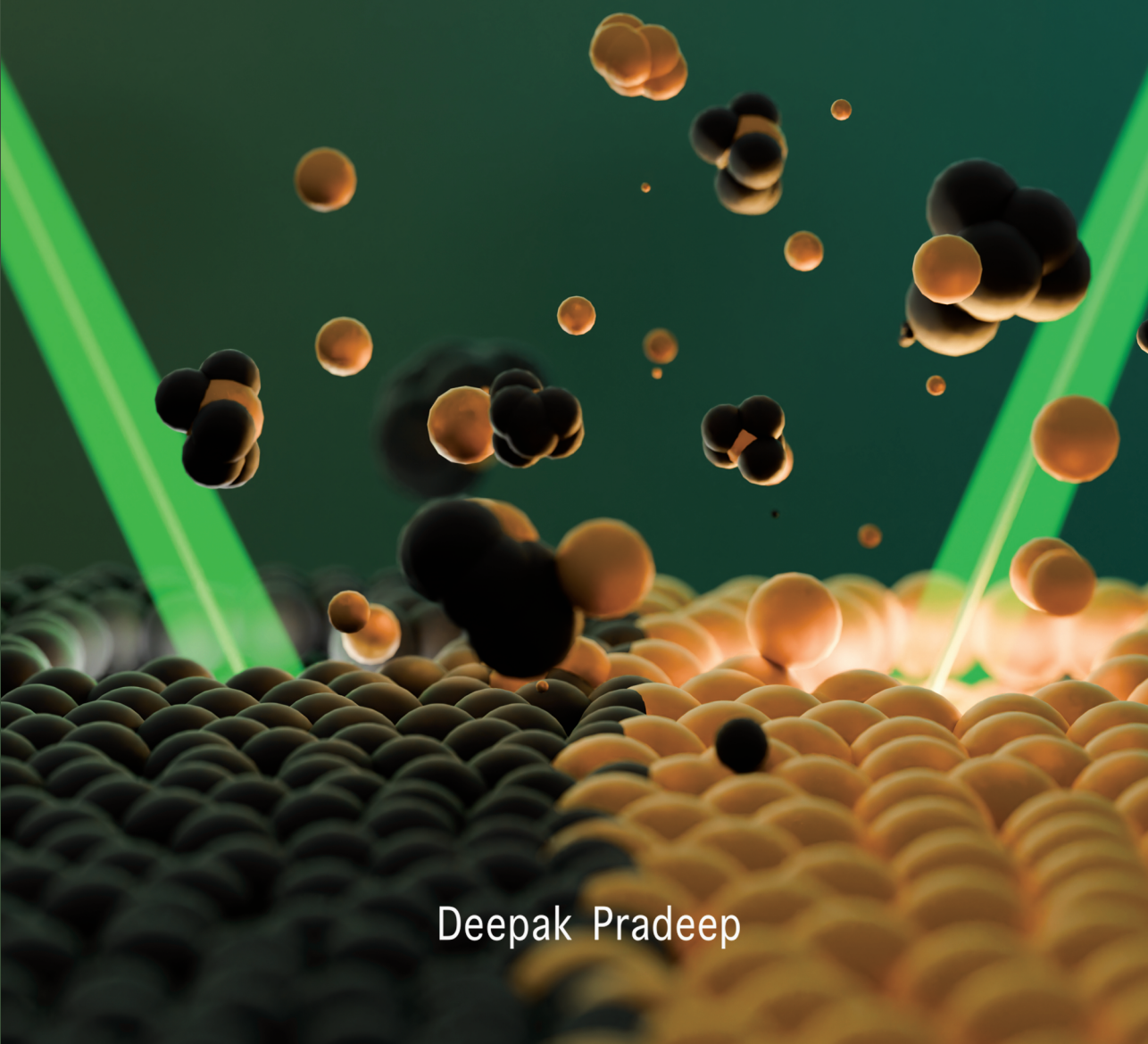

Deepak Pradeep

Structure and reactivity of gas-phase bimetallic clusters towards CO_2



Radboud Universiteit





Printed by: www. proefschriftmaken.nl

Cover design by: Auline Designs

About cover: The front cover shows two lasers creating tiny metal clusters (black) doped with a second metal (yellow). The back cover shows these clusters reacting with CO_2 (white and red), studied using infrared spectroscopy to reveal their structure.

This work is part of the European Union's Horizon 2020 CATCHY Innovative Training Network (ITN) under the Marie Skłodowska-Curie Actions (MSCA) grant agreement number 955650.

Structure and reactivity of gas-phase bimetallic clusters towards CO_2

Proefschrift ter verkrijging van de graad van doctor

aan de Radboud Universiteit Nijmegen

op gezag van de rector magnificus prof. dr. J.M. Sanders,

volgens besluit van het college voor promoties

in het openbaar te verdedigen op

dinsdag 20 oktober 2026

om 16.30 uur precies

door

Deepak Pradeep

geboren op 5 januari 1997

te Arpookara, Kerala (India)

Promotor:

dr. J.M. Bakker

Copromotor:

dr. P.A. Ferrari Ramirez

Manuscriptcommissie:

dr. J.A.A.W. Elemans

prof. dr. E. Janssens (KU Leuven, België)

prof. dr. S.M. Lang (Universität Ulm, Duitsland)

Table of Contents

1 Introduction 9

1.1. Atmospheric CO_2 9

1.2. CO_2 hydrogenation 10

1.3. Reaction mechanisms for CO_2 hydrogenation to methanol 12

1.4. Clusters as a model system 14

1.5. Clusters in CO_2 activation 15

1.6. Doping of metal clusters 16

1.7. Scope of this thesis 17

2 Spectroscopy and Theoretical Methods 19

2.1. Infrared spectroscopy 19

2.1.1 Harmonic Oscillator 19

2.1.2 Anharmonic Oscillator 20

2.1.3 The vibrations of a polyatomic molecule 21

2.1.4 Action spectroscopy 23

2.1.5 Infrared multiple photon dissociation and messenger tagging spectroscopy 23

2.2. Experimental approach 25

2.2.1 Cluster source 26

2.2.2 FELICE beam characteristics 28

2.2.3 Interaction region 30

2.2.4 Mass detection 32

2.2.5 Signal optimization 34

2.2.6 Signal interpretation and analysis 38

2.3. Density Functional Theory 40

3 Size-selective CO_2 activation by vanadium-doped cobalt clusters 45

3.1. Introduction 46

3.2. Experimental and computational methods 47

3.3. Results and discussions 49

3.3.1 Mass spectrometry: CO_2 adsorption on pure Co_n^+ and VCo_{n-1}^+ clusters… 49
3.3.2 Spectroscopy of $Co_n^+ \cdot CO_2$ and $VCo_{n-1}^+ \cdot CO_2$ products 53
3.3.3 Reaction paths for the adsorption and activation of CO_2 on Co_n^+ and VCo_{n-1}^+ clusters 57
3.4. Conclusions 61
A.3. Appendix to Chapter 3 63
4 IR spectroscopy of cationic MCo_n^+–CO_2 (M=Fe, Mn, Cr; *n*= 2-7) cluster complexes. 69
4.1. Introduction 70
4.2. Methods 72
4.2.1 Experimental 72
4.2.2 Computational 73
4.3. Results and discussion 74
4.3.1 $FeCo_n^+$ 74
4.3.2 $MnCo_n^+$ 77
4.3.3 $CrCo_n^+$ 79
4.4. Conclusions 88
5 Far-infrared spectroscopy of cationic vanadium-doped cobalt clusters 89
5.1. Introduction 90
5.2. Methods 92
5.2.1 Experimental 92
5.2.2 Computational 93
5.3. Results and discussion 94
5.4. Conclusions 103
6 Summary and outlook 105
Samenvatting 109
References 113
Research data management 127

List of Publications 127
Acknowledgements 131
Curriculum Vitae 135

1 Introduction

1.1. Atmospheric CO_2

Greenhouse gases (GHGs), such as water vapour, carbon dioxide (CO_2), methane (CH_4), and nitrous oxide (N_2O), are vital for maintaining our planet's suitable temperature for life. The Earth and atmosphere re-emit the absorbed energy from the sun as infrared radiation (heat) into space, and GHGs absorb this radiation, re-radiating a portion back down to the planet, creating a greenhouse effect.[1] However, since the Industrial Revolution, human activities have significantly increased the concentration of greenhouse gases, particularly CO_2, in the atmosphere, leading to global warming and climate change. Primary sources include burning fossil fuels, agriculture, industrial activities, and deforestation. **Figure 1.1** displays the atmospheric CO_2 levels recorded by the National Oceanic and Atmospheric Administration (NOAA) at Mauna Loa Observatory, Hawaii, since 1958. The level of CO_2 has increased from 365 parts per million (ppm) in 2002 to over 420 ppm at present.[2]

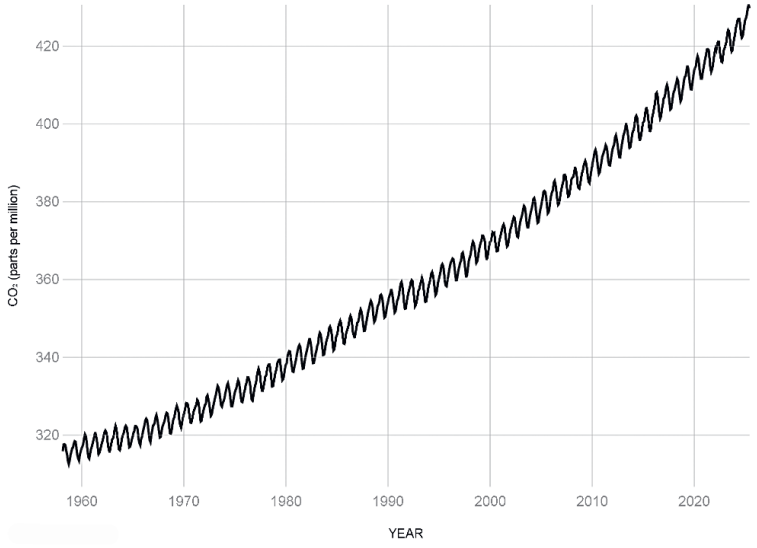

***Figure 1.1**: CO_2 concentration (in ppm) in the atmosphere measured since 1958 at Mauna Loa Observatory, Hawaii.[3] The seasonal cycle of peaks and troughs results from the Northern Hemisphere summer vegetation growth, which reduces atmospheric CO_2, and winter decay, which increases it. Data source: climate.nasa.gov.*

Two primary ways to control the CO_2 concentration in the atmosphere are reducing ongoing emissions and extracting existing CO_2 from the atmosphere. Reducing emissions can be achieved by shifting to renewable energy sources. At the same time, carbon dioxide removal can be accomplished through natural methods, such as planting trees, and technological solutions, like direct air capture (DAC).[4] The directly captured CO_2 can either be stored or utilised. Carbon capture and storage involves capturing CO_2 and permanently storing it underground; however, it presents high costs, technical challenges, and risks of CO_2 leakage. Therefore, carbon capture and utilisation, i.e., captures CO_2 and converts it into valuable chemicals, is a viable solution.[5] The captured CO_2 can be combined with green hydrogen to produce methanol and other chemicals, which then serve as building blocks for a wide range of materials.[6] However, due to the very stable molecular structure of CO_2 and its high dissociation energy (approximately 750 kJ/mol),[7] breaking the C=O double bond is difficult under standard temperatures and pressures. Therefore, a significant amount of energy is necessary for the reaction to occur.

1.2. CO_2 hydrogenation

Reacting carbon dioxide with hydrogen can, in principle, produce a range of chemicals, including methane, formic acid, carbon monoxide, and methanol. Of these, methanol has attracted the most attention because it is a versatile product that remains liquid at ambient conditions, making it easy to store and transport. Additionally, it is used as a chemical feedstock for various products, including formaldehyde, olefins, and acetic acid. The direct hydrogenation of CO_2 into methanol is an exothermic process:

$$CO_2 + 3H_2 \rightarrow CH_3OH + H_2O, \ \Delta H_{298K} = -49.5\ kJ/mol.$$

The equilibrium conversion of CO_2 requires high temperatures (typically below 300°C) and high pressures to shift the equilibrium towards the product side. Unfortunately, under these conditions, the above reaction competes with the endothermic reverse water-gas shift (RWGS) reaction, which produces the undesired side product, carbon monoxide (CO).[8]

$$CO_2 + H_2 \rightarrow CO + H_2O, \ \Delta H_{298K} = 41.2\ kJ/mol.$$

To favour CO_2 hydrogenation and reduce energy input, catalysts are utilised in the reaction, offering an alternative reaction pathway with lower energy barriers than the uncatalyzed reaction, resulting in higher selectivity of the end product.[9-11] The hydrogenation of CO_2 is primarily promoted by heterogeneous catalysts, where the

catalyst is a solid, and the reactants are gases or liquids. On the solid catalyst surface, CO_2 and H_2 adsorb; their bonds are weakened or broken, making them more prone to react. Generally, catalysts are dispersed on a support, which usually plays a crucial role in determining the activity, selectivity, and stability of the catalyst. Metal-support interactions can modify the electronic properties of the active metal, affecting how it adsorbs and activates reactant molecules.[12]

In industry, the synthesis of methanol from synthesis gas (syngas), a mixture of CO, CO_2, and H_2, is achieved over Cu/ZnO nanoparticles on an alumina substrate at temperatures ranging from 200 to 300°C and pressures of 50 to 100 bar.[13] The thermodynamics of producing methanol from CO_2 are less favourable than those from CO, so the one-pass methanol yield of the CO_2-based process is lower than that of the syngas-based process. For example, at 200°C, the equilibrium yield of methanol from CO_2 is just under 40%, whereas the yield from CO exceeds 80%.[14] Nevertheless, the performance of the Cu/ZnO/Al_2O_3 catalyst remains unsatisfactory for long-term use. Some reasons for catalyst deactivation include Cu particle sintering at high reaction temperatures,[15] and the formation of water as a by-product promotes ZnO agglomeration.[16] Furthermore, the reaction mechanism for industrial methanol synthesis as well as the nature of the active sites of Cu/ZnO-based catalysts remain subjects of considerable debate.[13, 17] Additionally, the high energy requirements of the reaction make this process costly. Therefore, developing new catalysts for CO_2 hydrogenation to methanol under mild conditions is crucial for a sustainable future.

As an alternative to the commercial Cu/ZnO/Al_2O_3 catalysts, a wide variety of other catalytic materials have been explored. Most of them are Cu-based catalysts, followed by Pd-based and some bimetallic catalysts. In Cu-based catalysts, ZrO_2 is used as an alternative support or promoter in CO_2 hydrogenation to methanol because of its good thermal and mechanical stability, as well as its higher methanol selectivity compared to the Cu/ZnO/Al_2O_3 catalyst.[18, 19] Pd-based catalysts have been suggested as an alternative to Cu-based catalysts because of their exceptional stability and resistance to sintering and poisoning.[20] Various supports, including metal oxides (such as ZnO) and carbon materials, have been used to enhance the catalytic activity of Pd-based catalysts.[21] In recent decades, many bimetallic catalysts (for example, CuZn, PdZn, and NiGa alloys)[22-24] have been tested for methanol synthesis from CO_2 hydrogenation because of their unique structural, chemical, and electronic properties, as well as the synergistic effects they exhibit compared to monometallic catalysts. Different heterogeneous catalysts used for CO_2

hydrogenation to methanol up to 2020 have been discussed in a review by Zhong et al.[25]

Copper remains the traditional catalyst for CO_2 hydrogenation to methanol, but cobalt is attracting interest for its activity at low temperatures and lower cost.[26, 27] Due to their high hydrogenation capacity and lack of RWGS activity, Co catalysts have an advantage for methanation.[28-31] In recent years, it has been found that Co-based catalysts are effective at producing products such as low-carbon olefins and long-chain alkanes.[32-35] Advances in cobalt-based catalysts for CO_2 hydrogenation, along with their future directions, are discussed in a review by Xixue He et al.[36] Therefore, cobalt is interesting and is selected as the primary element for this work.

1.3. Reaction mechanisms for CO_2 hydrogenation to methanol

The reaction mechanism and intermediates involved in CO_2 hydrogenation to methanol are still not fully understood, with various mechanisms proposed but not conclusively proven or disproven. As discussed in the review by Zhong et al,[25] the first, conventional pathway that is proposed is the formate pathway, in which CO_2 reacts with preadsorbed surface atomic H to produce the formate (HCOO*) intermediate via either an Eley-Rideal (ER) mechanism[37, 38] or Langmuir-Hinshelwood (LH) mechanism.[39] In the Langmuir–Hinshelwood mechanism, both CO_2 and hydrogen are adsorbed on the catalyst surface before reacting to form the HCOO*. In contrast, in the Eley–Rideal mechanism, gas-phase CO_2 directly reacts with preadsorbed hydrogen species on the surface to form HCOO*. The formed intermediate is then hydrogenated to produce dioxomethylene (H_2COO*), followed by loss of oxygen to generate formaldehyde (H_2CO*). Again, hydrogenation produces a methoxy (CH_3O*) intermediate, which is further hydrogenated to form methanol (CH_3OH). For example, density functional theory (DFT) calculations suggest that methanol synthesis on Cu (111) surfaces and unsupported Cu_{29} nanoparticles occurs via a formate intermediate,[37] with the overall reaction rate being limited by both formate and dioxomethylene hydrogenation.

A second or revised pathway via formate is also considered,[40] where the formate (HCOO*) is preferentially hydrogenated to formic acid (HCOOH*) instead of dioxomethylene (H_2COO*). The HCOOH* is further hydrogenated to produce H_2COOH*, and then the C-O bond in H_2COOH* is broken to generate H_2CO* and OH*. This then follows the same pathway as above to form methanol via the methoxy (CH_3O*) intermediate. It has been calculated that the energy barrier for

forming H_2COO^* from $HCOO^*$ is higher than that for forming $HCOOH^*$ from $HCOO^*$ by approximately 67.54 kJ/mol.[40]

A third proposed pathway is the HOCO-mediated reverse water-gas shift (RWGS) pathway, with carboxyl species ($HOCO^*$) as the key intermediate for the generation of CO,[41] followed by CO hydrogenation to methanol via intermediates such as formyl (HCO^*), formaldehyde (H_2CO^*), and methoxy (H_3CO^*). Furthermore, CO can also be produced from CO_2 ($CO_2 \rightarrow CO^* + O^*$) through direct dissociation without the intermediate $HOCO^*$, which is then hydrogenated to methanol via HCO^*, H_2CO^*, and H_3CO^* intermediates. First-principles kinetic Monte Carlo simulations on Cu/ZrO_2 reveal that methanol is produced through two pathways: the RWGS pathway, which involves CO from CO_2 dissociation, and the formate pathway.[42]

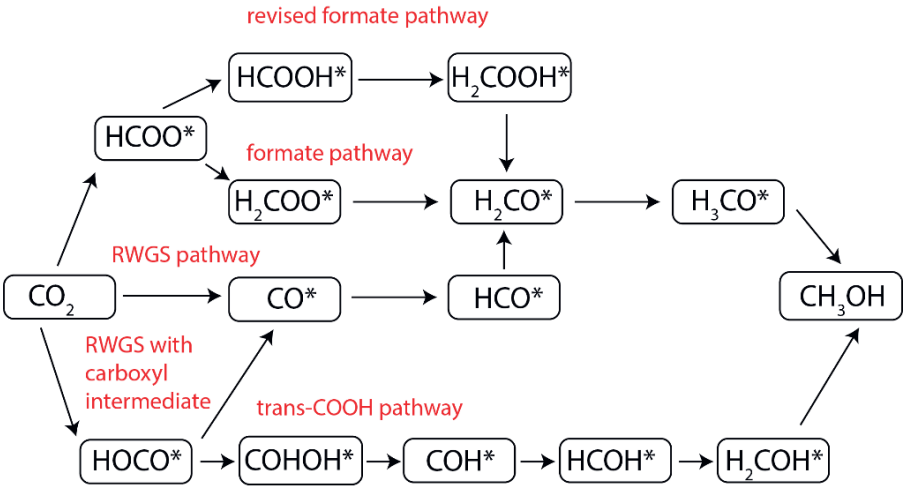

***Figure 1.2**: The proposed pathways for CO_2 hydrogenation to methanol over a catalyst.*

The last predicted potential pathway is the trans-COOH mechanism,[43] where the hydrocarboxyl ($COOH^*$) species is the initial hydrogenated form. This pathway involves H_2O; the $COOH^*$ species forms when adsorbed CO_2 reacts with H atoms provided by H_2O. The $COOH^*$ is further hydrogenated to dihydroxycarbene ($COHOH^*$). The dissociation of COHOH yields hydroxymethylidyne (COH^*), and methanol is produced via the hydroxymethylene ($HCOH^*$) and hydroxymethyl (H_2COH^*) intermediates.

Three main pathways have been proposed for cobalt-based catalysts in the production of C_1 products. The first is the formate pathway, which produces methanol, or alternatively, hydrogenation of the C-O bond after cleavage can form

$^{*}CH_x$, resulting in CH_4.[44] The second pathway involves the Reverse Water Gas Shift (RWGS) with a carboxyl intermediate, which is further hydrogenated to yield methanol.[45] The third pathway is the direct hydrogenation route, where *CO serves as the intermediate; it can either dissociate into CO or be further hydrogenated to produce CH_4.[44]

In conclusion, numerous potential pathways have been predicted so far, but no single pathway has been proven to be universally true. The efficiency and selectivity of CO_2 hydrogenation catalysts depend on reaction mechanisms and active sites, which are most likely influenced by chemical composition, electronic structure and geometry, as well as operating conditions. This cannot be easily studied or controlled in conventional bulk catalysts.

1.4. Clusters as a model system

Particles composed of a countable number of atoms, having properties that evolve atom-by-atom, are typically called clusters. They can serve as an ideal model system for studying reactions occurring on complex catalysts, in which small steps, kinks, or structural defects are usually the most active sites.[13] In clusters, such reactive sites can be mimicked and controlled by changing size, charge state and chemical composition.[46] Therefore, clusters can bridge the gap between molecular and bulk properties, as well as allowing the possibility of depositing them on a substrate, which can then be used as a catalyst for reactions.

By the 70s, it was already recognised that the reactivity of small clusters varied strongly with size.[47, 48] However, the characterisation of size-dependent properties of clusters only became possible after the possibility to form broad size distributions of clusters in molecular beams,[49] as for example, famously shown for sodium clusters.[50, 51] Later, Haruta and coworkers demonstrated that the inert bulk gold becomes highly reactive when its size is reduced to a few nanometres.[52] For instance, gold nanoparticles with an average size smaller than 10 nm can catalyse CO oxidation at room temperature.[53] Several other examples of size-dependent properties of clusters are available in the literature.[46, 54, 55]

Understanding the reaction mechanisms and active sites of metal clusters supported on a substrate is highly challenging due to the difficulty of maintaining stability under reaction conditions and the limitations of atomic-level characterisation techniques. In addition, clusters can oxidise or become contaminated unless studied in situ, and a strong metal-support interaction (SMSI) could alter their electronic and geometric

properties on the support.[56] Therefore, gas-phase clusters serve as an effective model system for investigating active sites and the reaction mechanism of a complex catalyst.[57, 58, 59] Controlled studies of reactions under isolated conditions will help elucidating the roles of the electronic structure and geometry of catalyst materials, as well as the impact of the size and chemical composition of the catalysts.

With the introduction of the laser vaporisation technique in 1981,[60, 61] the vaporisation of almost any type of metal and the formation of clusters over a wide range of sizes, even in different charge states, became feasible. This enables intensive studies on isolated metal clusters and cluster-molecule complexes.[62] Numerous experimental techniques have been developed to date to characterise metal ions, clusters, and their complexes in the gas phase.[63-66] Among these, photoelectron spectroscopy is primarily used to study the electronic structure of anionic and neutral ions or clusters.[65] In addition, photodissociation spectroscopy in the ultraviolet and visible regions reveals the behaviour of cluster complexes in their excited states, while in the infrared region, spectroscopy provides information on the geometry of clusters and cluster-molecule complexes.[66] The advent of quantum-chemical calculations, combined with efficient search strategies for geometrical configurations, has made the structures of clusters and complexes accessible. Benchmarking experimental data against quantum-mechanical predictions is nowadays a widely used and successful approach in cluster science.

1.5. Clusters in CO_2 activation

There have been some previous studies on CO_2 reduction on size-selected supported metal clusters. For instance, CO_2 reduction to methanol has been previously studied on copper clusters deposited on an alumina surface.[67, 68] Similarly, the conversion of CO_2 has been investigated on gold-based and silver cluster catalysts.[69-71] However, the atomic-level understanding of catalytic reactions on clusters has not been explored.

As discussed, CO_2 activation is considered the initial step in the hydrogenation of CO_2 to valuable products. Finding a robust catalytic system capable of activating CO_2 and subsequently reacting with H_2 at room temperature would be ideal. Upon the adsorption on a cluster, CO_2 can be present in three different forms: physisorbed, activated, or dissociated. A physisorbed or intact CO_2 is when CO_2 is in a linear structure with a 180 ° O-C-O angle. Activated CO_2 remains intact but does not retain its structure, which features a bent O-C-O angle. Dissociated CO_2 consists of a

separated carbon monoxide and an oxygen atom. A significant number of studies have investigated the size- and charge-dependence of the activity of isolated metal ions and clusters towards CO_2.[72-81] It has been observed that anionic metal ions or clusters can activate CO_2, while late transition metal cations like Co^+, Fe^+, Rh^+, Ir^+, Ni^+ ions and Cu_n^+ clusters (where *n* is the number of atoms) cannot. This difference is attributed to the ability of the anion to donate electron density into the π* antibonding orbitals of CO_2, activating the CO_2 and yielding a bent structure. The activity of neutral clusters has not yet been studied experimentally.

Catalytic materials often contain locally charged active sites, but the magnitude and distribution of these charges strongly depend on the charge transfer capabilities of the support. Metal clusters are usually deposited as ions, which allows the clusters to be accelerated, focused, and size-selected using electric fields, ensuring a uniform deposition. Upon soft landing, these clusters interact with the support, which may change their charge state.[82] Moreover, catalyst materials are much more complex than a single-element picture of the clusters, as evident from the bimetallic nature of the industrial $Cu/ZnO/Al_2O_3$ catalyst.[13, 83] Therefore, relying solely on cluster sizes and charges would not aid in designing an effective catalyst for CO_2 reduction; the catalyst's chemical composition also plays a role.

1.6. Doping of metal clusters

Single metal clusters often lack the necessary stability and activity criteria for catalysis. Doping of metal clusters can alter their electronic and geometric properties, thereby enhancing their activity,[84, 85] something that can already occur with the introduction of a single dopant atom. Studies of doped-metal clusters became feasible following the development of bimetallic cluster sources.[86-89] Kaya and coworkers first investigated the activity of bimetallic clusters compared to single-metal clusters, by reacting H_2 with vanadium-doped cobalt clusters.[90] Later, various studies investigated the structure and reactivity of doped clusters.[91-102]

Still, the main focus of this thesis, i.e., the CO_2 activation on bimetallic clusters, has mainly been explored theoretically. Given that copper is the conventional catalyst for CO_2 hydrogenation to methanol, these computational studies have focused on the CO_2 activation on doped copper clusters.[85, 103-106] Importantly, experimental studies on the CO_2 activation by bimetallic clusters are very limited. For instance, anionic copper oxide clusters and carbon-doped copper clusters can activate or dissociate the adsorbed CO_2 molecule,[77, 79] but the specific effect of the dopant could

not be confirmed through comparison with pure copper anions. Therefore, it is interesting to understand the dopant effect on CO_2 activation by reacting CO_2 with pristine and doped clusters and comparing their activity.

1.7. Scope of this thesis

As previously discussed, CO_2 activation can occur on anionic clusters due to electron donation from the cluster to CO_2. It is important to identify an alternative mechanism for activating CO_2 on cationic or neutral clusters. Therefore, this thesis investigates how a dopant atom doped into cationic single-element clusters can alter their activity towards CO_2. For this, the structures of the clusters, cluster-CO_2 complexes, and intermediates were examined using infrared spectroscopy, complemented by DFT calculations. The experimental and computational details are described in **Chapter 2**.

To investigate CO_2 activation on bimetallic clusters, CO_2 is reacted with cationic vanadium-doped cobalt clusters and pure cobalt clusters, and their activity is compared in **Chapter 3**. Cobalt is used as the main element, as CO_2 activation is observed on anionic cobalt clusters,[76] and it is also used as a catalyst for CO hydrogenation to long-chain hydrocarbons.[107] Vanadium is selected as a dopant because of its oxophilic nature with a strong V-O bond energy compared to late transition metals.[108] To understand the trend in the reactivity of 3d transition metals towards CO_2, different dopant atoms (M) are introduced onto cobalt clusters (MCo_{n-1}^+), and their activity towards CO_2 is studied in **Chapter 4**. Here, elements between vanadium and cobalt atoms in the periodic table, such as chromium, manganese, and iron, are used as dopant atoms. Since we identify vanadium as the most reactive dopant for CO_2 activation, the structure of the pure and vanadium-doped cobalt clusters is examined in **Chapter 5**. This is obtained by measuring the infrared spectra of their complexes with argon, which acts as a messenger. The activity of the different cationic doped cobalt clusters towards CO_2 is discussed, and the structure of the most active doped cobalt cluster is studied. The thesis is summarised (English and Dutch) in **Chapter 6**.

2 Spectroscopy and Theoretical Methods

2.1. Infrared spectroscopy

Infrared (IR) spectroscopy is an analytical technique used for structural characterisation of molecules based on the absorption of infrared light by molecular vibrations. These vibrations are at specific frequencies, depending on the masses of the atoms and the strength of the bonds involved. Frequencies of vibrational modes are typically in the range between 10 and 4000 cm^{-1} (2.5 – 1000 µm), which corresponds to the mid- and far-IR regions of the electromagnetic spectrum. For a vibration to be IR-active, it must cause a change in the dipole moment of the molecule.

2.1.1 Harmonic Oscillator

The absorption of IR radiation by a diatomic molecule can be modelled by two atoms connected by a massless spring, separated by an equilibrium distance r_0. Suppose in the first approximation, the bond is stretched or compressed from its equilibrium length r_0 to a new length r. The bond, similar to a spring, obeys Hooke's law, and the restoring force f is given by:

$$f = -kx,$$

where k is the force constant, and x = r-r_o is a small displacement from the equilibrium position. The potential energy of the molecule in this case is parabolic:

$$V(x) = \frac{1}{2}kx^2.$$

This model of a vibrating diatomic molecule is known as the simple harmonic oscillator model (**Figure 2.1a**). An elastic bond has a specific vibrational frequency given by:

$$\omega = \sqrt{\frac{k}{\mu}},$$

where μ is the reduced mass of the two atoms. Although the harmonic potential is idealised, the harmonic vibrational frequency provides a good first approximation.

Similar to other molecular energies, vibrational energies are quantised, and the permitted vibrational transition energies can be calculated from the Schrödinger equation. For the simple harmonic oscillator, these turn out to be:

$$E_v = \left(v + \frac{1}{2}\right)\hbar\omega \quad (v = 0, 1, 2, \ldots),$$

where *v* is the so-called vibrational quantum number. The energy levels are evenly spaced with a separation of $\hbar\omega$. At room temperature, the majority of the molecules are in the ground state (v= 0), thus with an energy equal to:

$$E_0 = \frac{1}{2}\hbar\omega,$$

which is known as the zero-point energy of the harmonic oscillator.

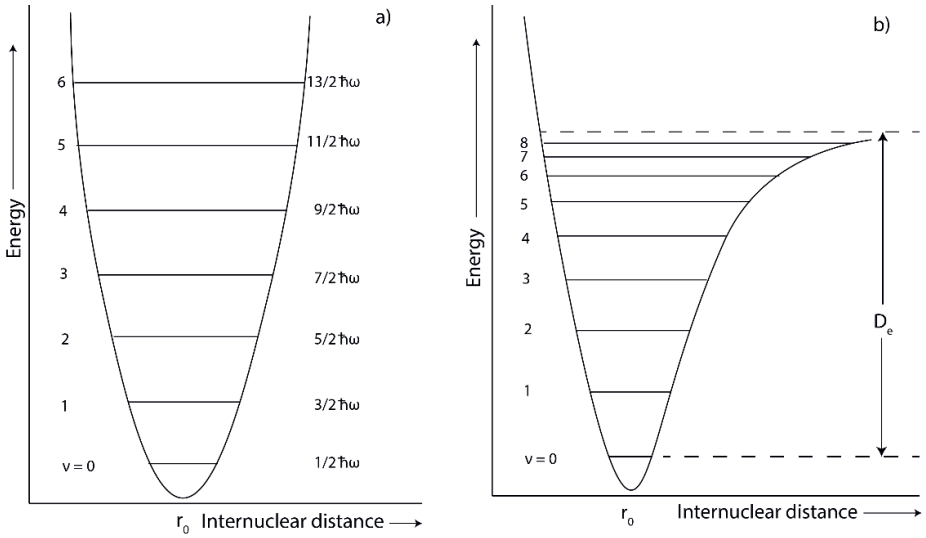

***Figure 2.1**: The vibrational energy levels for a diatomic molecule in a harmonic (a) and anharmonic potential (b).*

2.1.2 Anharmonic Oscillator

Real molecules do not obey the laws of a simple harmonic oscillator, because this would prevent a molecule from dissociating into atoms. Therefore, the motion becomes anharmonic, meaning that the restoring force is no longer proportional to

the displacement enough to follow Hooke's law. One method for calculating the energy levels considering anharmonicity is to use a function that more accurately resembles the true potential energy. The expression that fits this curve is the Morse function (**Figure 2.1b**):

$$V(r) = D_e\left[1 - e^{-\beta x}\right]^2,$$

where D_e and β are parameters that vary depending on the molecule. The parameter D_e represents the dissociation energy from the minimum of V(r), while β indicates the curvature of V(r) at that minimum. The harmonic oscillator approximation predicts a single vibrational line in the spectrum of a diatomic molecule. Experimentally, however, there is a primary (fundamental) line, along with weaker overtones at integer multiples of this fundamental. These vibrations can only be predicted by an anharmonic oscillator model. If anharmonic terms are included in the Schrödinger equation, the allowed vibrational energy levels are found to be:

$$E_v = \left(v + \tfrac{1}{2}\right)\omega_e - \left(v + \tfrac{1}{2}\right)^2 \omega_e\chi_e + \cdots \qquad (v = 0, 1, 2, \ldots),$$

where ω_e is the frequency, and χ_e is the anharmonicity constant, which is positive. Therefore, the vibrational energy levels become more closely spaced as the vibrational quantum number v increases. The harmonic oscillator approximation is most applicable for small values of v, which are the most significant at room temperature.

2.1.3 The vibrations of a polyatomic molecule

Molecules with more than two atoms have several vibrational normal modes. The number of normal modes depends on the number of atoms (N) and the geometry (linear or non-linear). Consider a molecule containing N atoms, where each atom has three coordinates (x, y, and z); the total number of degrees of freedom is therefore 3N. Of these, translational movement accounts for three degrees of freedom. For a non-linear molecule, rotations also require three degrees of freedom, leaving the molecule with 3N-6 vibrational modes. In contrast, for a linear molecule, there are 3N-5 vibrational modes because there is no rotation about the bond axis. For example, the linear CO_2 molecule has three atoms; therefore, it has four vibrational modes. The normal modes can be categorised by the type of motion: stretching (symmetric and asymmetric) and bending (in-plane and out-of-plane), and each mode has its own vibrational frequency. By convention, for the CO_2 molecule, the symmetric stretch is denoted by v_1, the bending motion by v_2, and the

asymmetric stretch by v_3. The in-plane and out-of-plane bending vibrations of CO_2 are identical except for their direction, so they are degenerate. All three vibrational modes of CO_2 are shown in **Figure 2.2**.

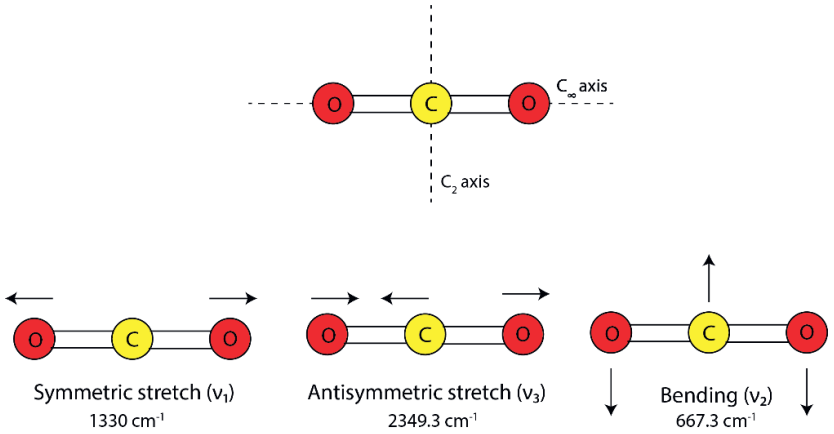

***Figure 2.2**: The symmetry and fundamental vibrations of the CO_2 molecule.*

Each vibrational mode of CO_2 is labelled as symmetric or antisymmetric based on the molecule's symmetry. For CO_2, there are two sets of symmetry axes: an infinite number of twofold axes (C_2) passing through the carbon atom at right angles to the bond direction, and an ∞-fold axis (C_∞) passing through the bond axis itself. If we rotate the vibrating molecule by 180° along the C_2 axis and the vibration remains largely unchanged, it is called a symmetric vibration. The bending vibration (v_2) is also symmetric. The rotation of the stretching motion, which is out of phase with the original, is described as an antisymmetric stretching mode. The symmetric stretch vibration causes no change in the dipole moment and is therefore infrared inactive. However, this vibration is Raman-active because the symmetric stretch vibration changes the polarizability of the CO_2 molecule. In the Raman spectra, this vibration has been observed as part of the Fermi resonance with the overtone of the bending vibration (v_1 *and* $2v_2$).[109] This is because the symmetry of v_1 is the same as $2v_2$, which results in a resonance through anharmonic coupling.[110] Importantly, when CO_2 is adsorbed onto a metal cluster, the CO_2 symmetry is broken, and the symmetric stretch vibration becomes IR-active. Similar to molecules, the metal clusters also exhibit vibrational modes at specific frequencies. These involve vibrations of metal-metal bonds and metal-ligand bonds. Metal-metal bond vibrations typically lie below 400 cm^{-1}.

2.1.4 Action spectroscopy

Typically, the IR absorption spectrum of a dense sample is obtained by illuminating the sample and measuring the variation in the intensity of the light passing through it. In conventional IR spectroscopy, the Beer-Lambert law explains the relationship between light absorption and sample properties. When electromagnetic radiation passes through a sample of length *l* and density *n* with a wavelength-dependent molecular absorption cross section $\sigma(\lambda)$, the transmitted $I(\lambda)$ and incident light I_o are related by:

$$I(\lambda) = I_0 e^{-\sigma(\lambda) n l}.$$

However, in the spectroscopy of molecular beams as used in this work, the number density (*n*) is typically too low (< 10^8 cm^{-3}) to produce a detectable absorption signal above the noise level. Therefore, action spectroscopy serves as an alternative method, where a physical or chemical change of the sample when it absorbs light is detected. In infrared action spectroscopy, when a molecule resonantly absorbs IR photons, the absorbed energy is converted into vibrational motion, thus heating the molecule. If enough energy is accumulated—often from multiple photons—the total internal energy can exceed the bond dissociation energy, causing the molecule to fragment, which can be detected by a mass spectrometer. The molecule can also relax by emitting photons or electrons; however, the fragmentation tends to be the most favourable pathway because dissociation energies are typically lower than ionization energies. In some cases, photon emission can compete with fragmentation and prevent the observation of fragments, but typically the fragmentation rate is higher if sufficient internal energy is reached. The action spectrum is obtained by plotting the fragmentation or depletion yield against the wavelength of the laser, refer to section 2.2.6.

2.1.5 Infrared multiple photon dissociation and messenger tagging spectroscopy

For strongly bound systems, such as metal clusters, reaching the dissociation threshold is not easy due to the high binding energy of such systems. The mid- and far-infrared region discussed in this thesis spans from 100 to 2200 cm^{-1} (4.5–100 µm), corresponding to photon energies between 0.0124 and 0.276 eV (with 1 eV equivalent to 96.485 kJ/mol or 8065 cm^{-1}). The binding energy between two cobalt atoms is calculated as 2.86 eV.[111] The typical vibrational frequency of the cobalt

dimer is calculated close to 300 cm^{-1}. Approximately 75 photons are needed to be absorbed to overcome the binding energy of the cobalt dimer and thus observe dissociation. These values represent the minimum estimates, as dissociation is a statistical process. Having just enough energy does not guarantee dissociation within a finite timescale, except possibly for very small clusters. In the case of metal-ligand complexes, such as iron cluster monocarbonyls, Fe_n^+-CO, the binding energy is reported to be between 1.2 and 2.8 eV, depending on the size of the cluster.[112] The typical stretching frequency of carbonyl is around 2000 cm^{-1}, so only 5 to 11 photons are needed to eliminate CO, thus much lower compared to bare metal clusters. In such cases, infrared multiple photon dissociation (IRMPD) spectroscopy[113-115] can be utilised to dissociate the clusters and cluster-molecule complexes, and use this as a tool to obtain the IR spectrum.

For bare metal clusters, the messenger tagging technique[116] can be used to facilitate IRMPD spectroscopy because of the large number of photons that would be required to reach the dissociation threshold of the bare species. Here, the cluster is complexed with an atom of inert gas, such as argon, forming a weak Van der Waals bond. A messenger complex can dissociate after absorbing just one or a few photons; thus, it significantly enhances the sensitivity to weak absorption bands or bands at low IR frequencies. For example, the typical Ar binding energies to small cobalt cluster cations (Co_n^+) range from approximately 0.1-0.3 eV for $n \geq 6$ to 0.3-0.5 eV for smaller sizes,[117] which is much lower compared to the binding energies between cobalt atoms. Compared to direct fragmentation, the messenger technique offers the ability to avoid band broadening caused by saturation effects at high IR laser fluences and to reduce anharmonic band shifts, resulting in spectra obtained using a messenger tag being much better resolved than those measured by IRMPD.[118] Nevertheless, the binding of any messenger species may influence the structure, vibrational spectrum, and even bias to specific isomers, meaning that the isomer distribution in the tagged clusters does not necessarily reflect the distribution in the non-tagged clusters.[119]

Sequential absorption of multiple IR photons by a single complex can be achieved using the high photon fluences produced by Free Electron Lasers (FELs).[120] However, as discussed earlier in section 2.1.2, the vibrational potential is anharmonic for real molecules, so the energy spacing between vibrational states in a potential well is not constant. This effect prevents the cluster-molecule or cluster-rare gas complex from absorbing multiple photons in a ladder-climbing manner. Therefore, if the laser is tuned to a frequency resonant with a specific vibrational mode, it causes the

absorption of a single photon, which excites that mode from the vibrational ground state (v=0) to the first excited state (v=1). Due to anharmonic coupling between the initially excited vibrational mode and all other vibrational modes of the cluster-molecule complex, it rapidly undergoes internal vibrational redistribution (IVR).[121, 122] Energy is dissipated into the bath of other vibrational states on the nanosecond to picosecond timescale, effectively thermalising the vibrational energy across the complex. Once IVR occurs, the originally excited mode returns to v = 0 and becomes ready to absorb the next photon of the same frequency. This cycle of photon absorption, IVR, and re-excitation repeats, allowing multiple photons to be absorbed and increasing the internal energy. This multiple photon absorption process is facilitated by the FEL's time structure, which comprises a train of micro pulses, as will be discussed in section 2.2.3. Eventually, the total internal energy exceeds the dissociation threshold, resulting in bond breaking and the fragmentation of the cluster-molecule complex.

2.2. Experimental approach

The experiments detailed in this thesis were conducted using the Free Electron Laser for Intracavity Experiments (FELICE) molecular beam setup[123, 124] at HFML-FELIX, shown in **Figure 2.3**. The experimental setup consists mainly of four parts: a cluster source, a flow-tube reaction channel, an interaction region and a time-of-flight (TOF) mass spectrometer.

The bimetallic clusters are produced by laser ablation of two separate metal targets, and the metal vapours formed are collisionally cooled down by helium in the cluster source to promote cluster formation. The clusters are then entrained into a reaction channel, where they are tagged with reactants. Afterwards, the mixture of clusters, cluster-molecule complexes and helium is expanded supersonically into vacuum to form a molecular beam. The molecular beam is then collimated by a 2 mm diameter skimmer as it enters a differentially pumped vacuum chamber (pumped by a 500 l/s turbomolecular pump) and is further shaped by a rectangular slit aperture (2 x 8 mm) to ensure good overlap with the FELICE laser at the interaction chamber. Both shaping elements are electrically grounded. The molecular beam interacts with the infrared laser beam, thereby resonantly exciting the cluster-molecule complexes, leading to their fragmentation. After this process, the distribution of clusters and cluster-molecule complexes is extracted into a TOF mass spectrometer by applying high voltages to the extraction and repulsion plates, and is then detected using a micro-channel plate-based detector. IR spectra of cluster-molecule complexes

obtained through a laser on-off experiment, in which two mass spectra with and without IR irradiation are recorded at each laser frequency, and their logarithmic ratio provides the IR spectra. A detailed description of the components used for the experiment is provided below.

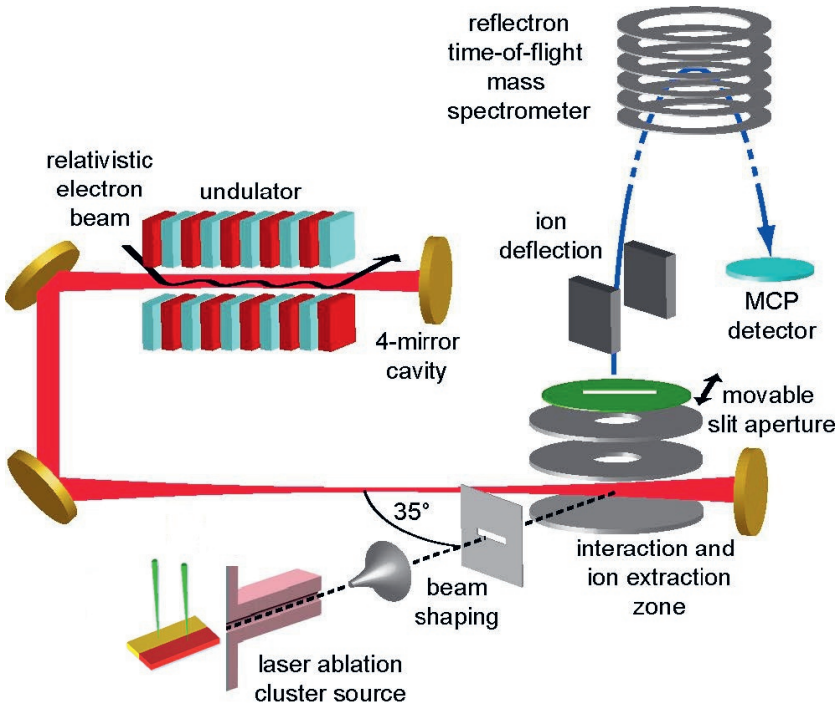

***Figure 2.3**: Schematic depiction of the FELICE molecular beam experiment setup located at the FELICE beamline of the HFML-FELIX laboratory. Reproduced from Ref.[124] with permission from the American Chemical Society.*

2.2.1 Cluster source

Single-element clusters are usually generated using a Smalley-type laser ablation source.[60, 125] However, here, the gas-phase bimetallic clusters are generated using a dual-target dual-laser ablation source[87, 88] based on an existing design from the KU Leuven Solid State Physics group. The cluster source is placed in a source chamber pumped by a 1200 l/s turbomolecular pump, which is backed up by a fore pump, resulting in a pressure of 10^{-7} mbar.

The schematic overview of the bimetallic cluster source with the additional reaction channel is illustrated in **Figure 2.4a**. The metal clusters are produced by laser ablation

of metal targets. The cluster source consists of a target holder in which two rectangular targets, each measuring 24 x 7 x 1 mm³ (*length × width x thickness*), are mounted, and a motion system moves the holder perpendicular to the gas flow (transverse (X)) and parallel to the gas flow direction (longitudinal (Y)). The motion system includes two stepper motors that move sequentially, such that the target holder moves in a snake-like trajectory. The stepper motors are controlled by LabVIEW software, which allows modification of the speed (typically 0.1 mm/s) and range of motion of the targets. The target holder is mounted above the transverse moving platform and is supported by four spring-loaded poles that press it against the source block. Within the source block, a small cylindrical volume (17 mm long and 3 mm in diameter) is used for cluster formation. This volume is directly connected to a channel through which the carrier gas is introduced, along with two small channels for ablation lasers and a channel for clusters to exit and react with other gas molecules (flow-tube reaction channel). The carrier gas (typically He) is introduced into the formation chamber via a pulsed supersonic valve (Jordan TOF Products, Inc.), producing gas pulses with a duration of approximately 60 µs at a repetition rate of 10 Hz. The helium pressure in the clustering channel cannot be determined in the current configuration; however, the pressure in the source chamber rises from 10^{-7} to 10^{-5} mbar.

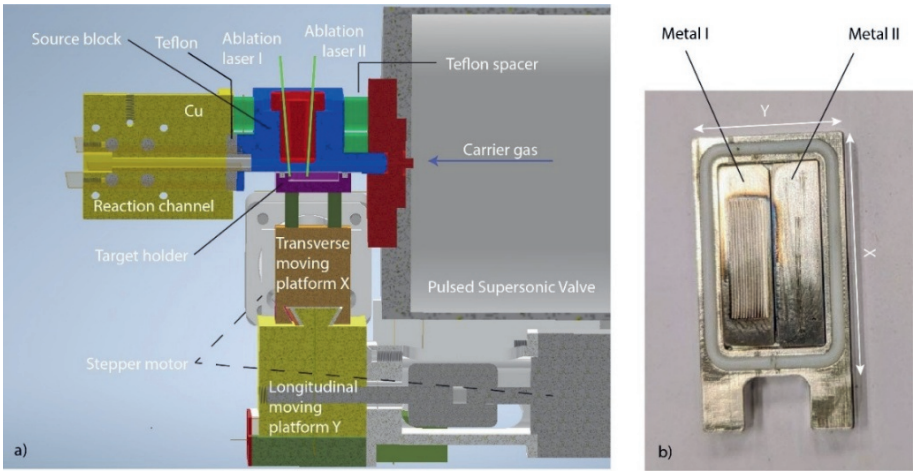

***Figure 2.4**: (a) Half-section view of the dual-target dual-laser ablation source designed in Autodesk Inventor software, and (b) arrangement of metal targets in a target holder (laser-ablated portion is visible in one of the targets).*

For ablation, two independent frequency-doubled Nd:YAG lasers (532 nm, 10 Hz, ~5 ns pulse duration) are focused on the targets. The spot size of the ablation lasers is

controlled by two focal lenses, each with a 400 mm focal length, mounted on a breadboard that contains all the optics for the lasers, positioned above the source chamber. The two lasers are focused on the targets through a laser insert with two small tapered apertures (2 mm in diameter at the top and 1.2 mm at the end), which reduces the amount of carrier gas escaping the formation chamber. Additionally, a fused-silica glass window with a diameter of 10 mm and a thickness of 2 mm is placed above the laser insert to improve sealing. The laser energy density, or laser fluence, on the target is a crucial parameter for cluster production and varies across different elements. This depends on the laser's spot size on the target, which can be adjusted by moving the focal lenses closer to or further away from the target.

The source and clustering channel are extended by a copper body, in which reactants can be injected through a second pulse valve (Parker General Valve series 9). A ceramic spacer is placed between the second valve and the copper body to provide thermal isolation. This flow-tube reaction channel has a total length of 42 mm. It is made of copper to ensure a uniform temperature distribution along the channel because of its high thermal conductivity. The channel has a cylindrical shape, beginning with a 3 mm diameter for a length of 32 mm, then expanding to a 6 mm diameter over the remaining 8 mm. The reaction channel is separated from the clustering channel by a 3-mm-thick Teflon spacer for thermal isolation. The entire source block and copper channel are mounted on the face of the pulsed supersonic valve body using threaded rods. On the copper component, a cooling system is attached, through which a continuous flow of liquid nitrogen can be circulated. A cartridge heater is inserted into the cooling block, and the temperature of the reaction channel is monitored with a K-type thermocouple gauge. To stabilise the source temperature, a PID controller (West 6100+) reads the thermocouple and controls a DC power supply connected to the cartridge heater within an integrated feedback loop.

2.2.2 FELICE beam characteristics

The infrared light for our experiments must be very intense because the cluster-ligand complexes are strongly bound and require many photons to be absorbed before dissociation. That is why we use a Free-Electron Laser (FEL) for all our experiments. Specifically, FELICE is used, which provides much higher pulse energies than traditional FELs. This is due to the unique configuration of the FELICE setup, where the beam of gaseous molecules interacts directly with the laser within the laser cavity, rather than extracting a portion of the light and guiding it to the external

experimental stations. This results in up to 50 times more IR photons reaching the molecules compared to extra-cavity FEL experiments.[123] The only limitation is that samples under investigation should not interfere with the functioning of the laser by causing losses, and can therefore only absorb a very small fraction of the IR light in the cavity. The gas-phase studies on metal clusters involve very dilute samples, which fulfil the vital requirement.

Conventional lasers use atoms or molecules as their active medium to generate coherent light. An infrared free-electron laser differs from traditional lasers in that it utilises a bunch of high-energy free electrons to produce intense, coherent, and tunable infrared radiation, as shown in **Figure 2.5**. Using a linear accelerator (linac), electrons are accelerated to relativistic energies, typically to 10-50 MeV. Electrons are then injected into an undulator, a device composed of a series of magnets carefully spaced with alternating north and south poles. As the electrons travel through these alternating magnetic fields, they are forced into a sinusoidal path by the Lorentz force. These transverse oscillations cause them to emit synchrotron radiation. By adjusting the energy of the electrons and the period of the undulator's magnetic field, the FEL can be tuned to emit a specific infrared wavelength. The resonant wavelength is given by:

$$\lambda_r = \frac{\lambda_u}{2\gamma^2}(1 + \kappa^2),$$

where λ_u is the period of the undulator, γ is the electron's relativistic Lorentz factor, and κ is the undulator parameter that depends on the on-axis magnetic field strength.

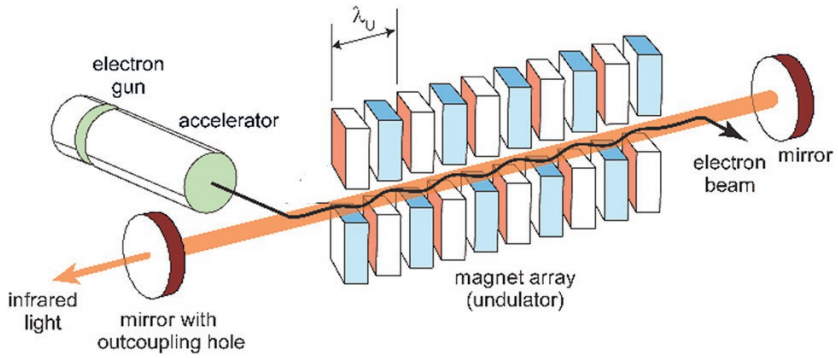

***Figure 2.5**: Scheme of an infrared free-electron laser, which includes an electron gun, a linear accelerator, and an undulator. FELICE features a four-mirror cavity to accommodate the FELICE molecular beam instrument. Reproduced from Ref.[66] with permission from the Royal Society of Chemistry.*

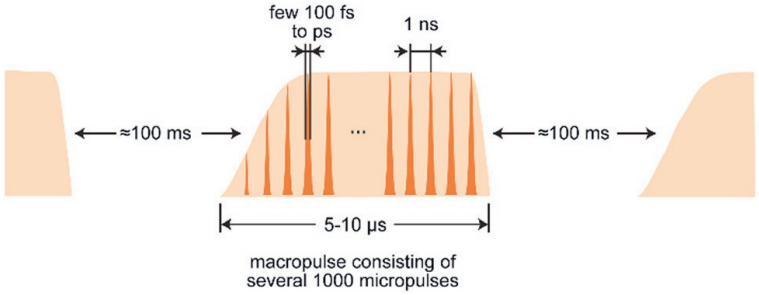

***Figure 2.6**: Typical pulse structure of the infrared light emitted by the free electron laser at a repetition rate of 1 GHz for micro-pulses and 10 Hz for macro-pulses. Reproduced from Ref.[66] with permission from the Royal Society of Chemistry.*

FELICE can be tuned across the 4.5-100 µm (100-2200 cm^{-1}) spectral range. It has a distinct pulse structure, comprising a macro-pulse composed of a series of micro-pulses (see **Figure 2.6**). Each micro-pulse has a pulse length ranging from a few 100 fs to ps and a repetition rate of 1 GHz. One macro-pulse usually lasts between 5 and 10 µs and has a repetition rate of 5 or 10 Hz. This pulse structure concentrates a large amount of energy into a very short time window, which is required for sequential photon absorption in IRMPD spectroscopic experiments. It has high pulse energies, typically ranging from 0.9 to 1.3 J, based on the different frequencies and typical spectral bandwidths between 0.5 and 3% full width at half maximum (FWHM) of the central frequency. The bandwidth of the radiation is determined by the Fourier transform of the micro-pulse duration, which can be adjusted by changing the cavity length. Pulse energies and spectral properties are measured outside the FELICE cavity by outcoupling a small fraction of the laser beam.

2.2.3 Interaction region

Past the skimmer and slit aperture is the region where the molecular beam interacts with the FELICE laser. FELICE is constructed with a four-mirror cavity, with the molecular beam setup located in the 2-metre section between the last two mirrors. The FELICE molecular beam instrument has two source chambers with central axes oriented at angles of 35° and 55° relative to the laser beam.[123] The cluster source is situated in the 35-degree source chamber, so the molecular beam interacts with the laser beam at this angle, as shown in **Figure 2.7**. The source chamber can be isolated from the interaction region using a gate valve, so that venting of the source chamber does not affect the vacuum pressure in the interaction region or cavity. To ensure spatial overlap between the laser and molecular beams, as well as to control the laser fluence in the interaction region, the entire molecular beam instrument can be

moved horizontally and vertically relative to the fixed focus of the IR beam. Horizontal movement along the laser beam reduces fluence, whereas vertical movement overlaps the molecular beam with the laser beam. To achieve this, the entire molecular beam setup is mounted on a movable platform connected to two stepper motors, each with a precision of 0.1 mm.

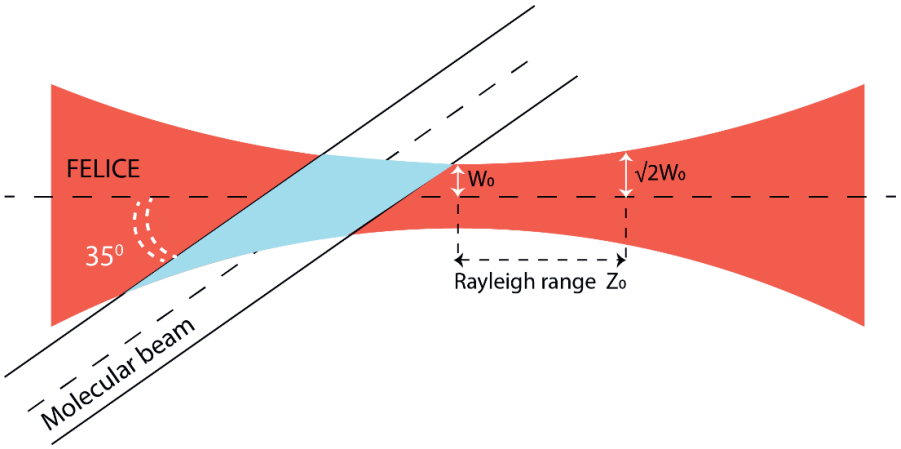

***Figure 2.7**: Schematic of the spatial overlap between the FELICE laser beam and the molecular beam. The laser waist at the focus (w_0) depends on the wavelength of the laser.*

The optical beam of the FELICE laser is assumed Gaussian, characterised by a Rayleigh range Z_0 of 55 mm and a focal point located roughly at the centre between the two cavity mirrors. The laser waist at focus (w_0) is wavelength-dependent, ranging from 0.2 to 1 mm at various wavelengths. The radius of the laser beam increases from the focus towards the edge, resulting in a decrease in laser fluence. It is possible to increase the interaction volume by moving the molecular beam further away from focus (up to about 300 mm); however, this will reduce the laser fluence by a factor of 30. The maximum diameter (height) of the molecular beam can be estimated by dividing the distance from the source exit to the laser by the distance from the source exit to the slit, and then multiplying this value by the height of the slit. For loosely bound species like metal-Ar complexes, even at the maximum out-of-focus position, the infrared spectrum can become saturated due to the high laser fluence. With traditional lasers, you can use attenuators between the laser and the experiment to achieve this. However, in an intracavity setup, inserting an attenuator isn't feasible because it would disrupt FELICE's lasing. Instead, the experimental setup is moved vertically to decrease the fluence, which is possible due to the Gaussian nature of the laser beam; the fluence reduces exponentially towards

the edges. To obtain a good IR spectrum with enhanced spectral sensitivity and decreased band saturation, it is essential to determine the optimal spatial (and temporal) overlap. Additionally, the visibility ratio of spectral bands is increased by preventing complexes in the molecular beam that did not interact with the IR light from entering the mass spectrometer by a slit aperture positioned above the extraction plates inside the flight tube of the TOF mass spectrometer.

2.2.4 Mass detection

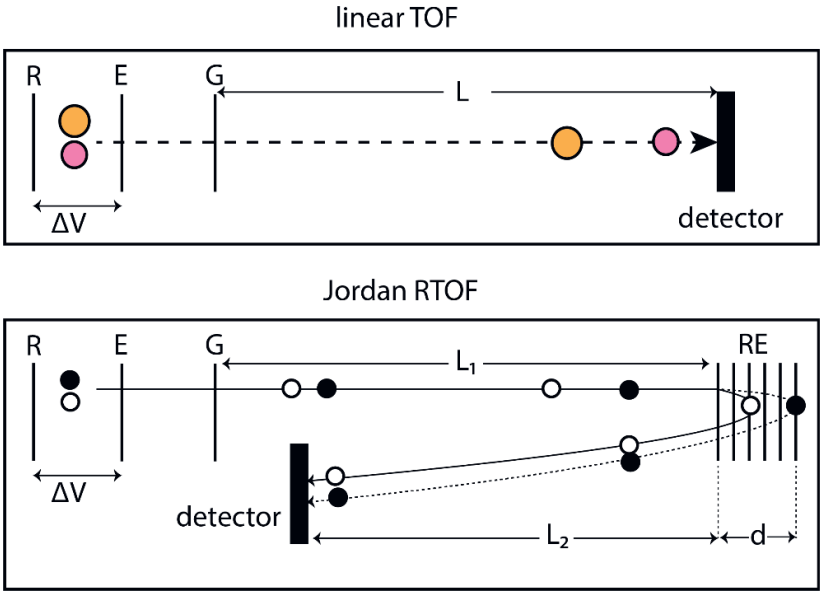

***Figure 2.8**: **Upper panel**: schematic of a linear Wiley and McLaren time-of-flight mass spectrometer. The orange and magenta circles represent ions with different masses. **Bottom panel**: Jordan reflectron time-of-flight mass spectrometer. The illustrated ions have the same mass but different initial kinetic energies (the white circle has lower kinetic energy than the black one). The slower ion trajectory is depicted with a black line, while the faster ion trajectory is shown with a dotted line.*

After the molecular beam is irradiated with FELICE, the ions are extracted into a reflectron time-of-flight mass spectrometer (Jordan TOF Products Inc.) and detected by a micro-channel plate (MCP)-based detector. The flight tube of the TOF-MS is perpendicular to the molecular and laser beam axes, with a source region featuring three high-voltage electrodes: a repeller plate (R), an extractor plate (E), and a ground plate (G). The extractor and repeller plates are pulsed with high voltages using fast switches (Behlke HTS 51, rise time ~40 ns). These voltages are applied to accelerate the ions between the repeller and extractor plates in the interaction chamber, directing them into the TOF-MS. The voltage on the extractor is lower than

on the repeller (e.g. V_E = +3392 V, V_R = +5046 V). The trigger pulse timing on these plates is synchronised with cluster formation (discussed in Section 2.2.5), ensuring that the molecular beam encounters these high voltages only after entering the region between the plates.

Ions with different masses will experience different accelerations due to the potential difference between the extractor and repeller plates. This process occurs in the areas R-E and E-G within the acceleration region, as illustrated in **Figure 2.8**. When the ions leave the acceleration region, they enter a field-free region where they are separated according to their velocities. Lighter ions (top panel, magenta circle) are accelerated to higher velocities than heavier ones (orange) and reach the detector earlier. Mass-to-charge ratios (*m/z*) are determined by measuring the time that ions take to move through a field-free region between the source region and the detector.

Consider an ion with mass *m* and charge *q = ze* that is accelerated by a potential difference *ΔV* at the source region. Its potential energy (E_p) is converted into kinetic energy:

$$E_p = q\Delta V = ze\Delta V = \frac{mv^2}{2},$$

So that the velocity of the ion leaving the acceleration region is given by:

$$v = \left(\frac{2ze\Delta V}{m}\right)^{\frac{1}{2}} \text{ or } \sqrt{\frac{2ze\Delta V}{m}}.$$

If the ion then travels a field-free distance *L* to the detector in a linear TOF mass spectrometer[126] (**Figure 2.8**, top panel), the flight time t_{tof} is calculated as:

$$t_{tof}^2 = \left(\frac{L}{v}\right)^2 = \frac{m}{z}\left(\frac{L^2}{2e\Delta V}\right),$$

the equation shows that the mass-to-charge ratio of the ions can be calculated from the flight time of the ions using a relation, $m/z = \alpha t_{tof}^2$, where α is a constant.

However, the resolution of the linear TOF is limited by the kinetic energy spread of the ions. This issue can be addressed by using a reflectron time-of-flight (RTOF) mass spectrometer[127] (**Figure 2.8**, bottom panel), where an ion mirror (reflector RE) compensates for the energy spread, thereby enhancing mass resolution. Faster ions (black circle) penetrate deeper, spend more time in the reflectron, and reach the detector simultaneously with slower ions (white) with the same *m/z*. In this case,

the total flight length of the ion consists of the distances before and after the reflectron (L_1 and L_2), as well as the distance travelled inside the reflectron. A quantitative approach to this process is detailed elsewhere.[128]

When these time-separated ions hit the plates of the MCP detector, each ion enters a microscopic pore, strikes the wall, and triggers a cascade of electrons that generates a measurable current pulse. The resulting current is amplified and recorded using a transient digitiser (Acquiris DP310), and the data are analysed using custom-built LabVIEW software.

2.2.5 Signal optimization

This section covers the parameters that affect cluster formation in the dual-target dual-laser ablation source. Laser energy, the timing between the gas pulse and the laser, the timing between the two lasers, and carrier gas pressure are crucial factors influencing bimetallic cluster production, as explained in detail below. Furthermore, maintaining the stability of the cluster signal throughout the entire FELICE beam period is vital for obtaining high-quality IR spectra. Therefore, this section discusses the components of the cluster source essential to ensuring a stable signal.

Parameters affecting cluster production

Laser energy

Duncan has provided a detailed description of the physical aspects of cluster production using a Smalley-type laser ablation source.[129] It was found that vaporisation depends on the laser pulse energy, the reflectivity of the metal surface at the employed wavelength, the laser pulse duration, the thermal conductivity of the material, and the composition of the plasma produced above the material.[130] For nanosecond lasers like the Nd:YAG laser, vaporisation happens within the first few picoseconds of the laser pulse, followed by plasma formation. The rest of the laser pulse heats the plasma that has already been created. Therefore, there is a minimum threshold for the laser pulse energy at which vaporisation begins, an optimal range that operates effectively, and a maximum threshold beyond which excessive heating of the plasma occurs. Above the threshold, carrier gas atoms are unable to effectively cool the metal atoms, resulting in fewer cluster formations. Determining the optimal laser pulse energy is crucial for cluster production, which relies on the reflectivity, thermal conductivity, and plasma dynamics of various materials. In the case of bimetallic cluster production, the metal composition within the clusters can

be adjusted by controlling the laser pulse energies (as well as laser timings, discussed below) on both the dopant and the main cluster. The laser power is controlled by adjusting the Q-switch timing relative to the lamp firing of the Nd:YAG laser. In addition, selecting the laser wavelength (532 or 355 nm) for ablation is important for specific systems. For instance, producing copper clusters is easier with the frequency-tripled (355 nm) wavelength than with the frequency-doubled (532 nm) wavelength of the Nd:YAG laser.

Carrier gas stagnation pressure

Carrier gas is vital for cooling the plasma produced by laser ablation and aiding cluster formation. The small clustering channel enables the carrier gas to accumulate pressure, supporting the condensation process and dissipating the heat generated during cluster formation. Helium is primarily used as a carrier gas. A mixture of helium and argon is used for metal vapours that cannot be cooled effectively by helium gas. The optimum backing pressure of the carrier gas is crucial for cluster formation. Typically, at low stagnation pressures (below 5 bar), clusters are not formed. Pressures between 5 and 10 bar are primarily used for cluster formation. For the experiments in this thesis, a stagnation pressure of 8 bar helium is used.

Synchronisation

The cluster source consists of three pulsed elements that must be synchronised to produce a good signal: the carrier gas valve, ablation laser I, and ablation laser II. The most critical parameters are the time between the carrier gas pulse and the ablation laser ($\Delta\tau_1$) and the timing between the two ablation lasers ($\Delta\tau_2$), shown in **Figure 2.9**. The pulsed elements are externally triggered by a pulse generator (Quantum Composer 9520 series), which provides an initial delay (T_0) to start the experiment and enables the adjustment of the time delay between components. For the production of vanadium-doped cobalt clusters in Chapter 3, the pulsed supersonic valve opens approximately 400 µs before the ablation lasers to ensure an optimal pressure at the ablation region. To control the vanadium doping in cobalt clusters, the laser on the vanadium target is fired either earlier or later than the laser on the cobalt target with a time delay ($\Delta\tau_2$). Additionally, to extract all the formed clusters into the TOF-MS and detect them with the MCP detector, the time delay between the ablation laser pulse and the extraction pulse ($\Delta\tau_3$) on the plates must be optimised. This is around 350-400 µs in our experiments. The timing between

different events can significantly affect the distribution of cluster sizes that are formed and/or detected.

For the experiments involving the reactivity of bimetallic clusters towards specific reactants (e.g CO_2), the reactant is injected into the reaction channel via a separate pulsed valve. The opening time of this valve also needs to be optimised and synchronised with the cluster formation to prevent the reactants from arriving too early or too late to the reaction channel. If the reactant is introduced too early, there is a risk of back-streaming of the reactants into the clustering channel, which can disrupt the clustering process. If the reaction valve opens too late, the clusters will have already left the reaction channel, and no complexes will be formed. Therefore, in our experiments, to account for the internal delay in opening the valve for CO_2 injection, it is triggered approximately 900 µs before extraction to ensure that the clusters are exposed to CO_2. The delay time between the reactant valve and the extraction is $\Delta\tau_4$.

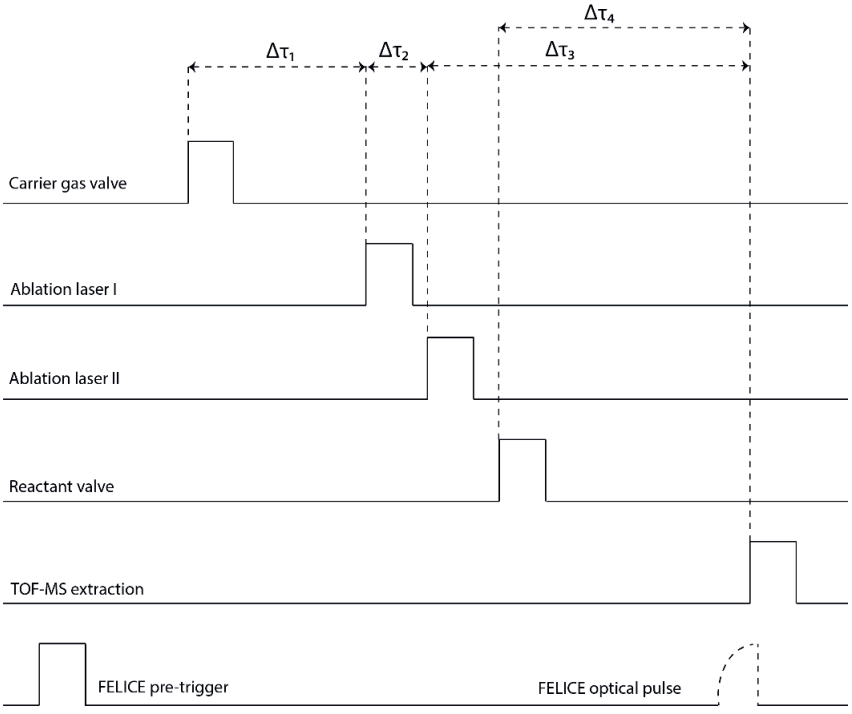

***Figure 2.9**: Schematic diagram of the synchronisation of various triggers with the pulsed elements in the experiment.*

For the experiments involving the FELICE laser, the entire molecular beam setup is synchronised to a pre-trigger from FELICE, typically 3 ms before the optical pulse. As discussed in Section 2.2.2, the overlap in time between the molecular beam and laser beam is crucial for obtaining a good IR spectrum. This is achieved by optimising the delay of the pulsed components relative to the FELICE pre-trigger, ensuring the cluster distribution arrives at the interaction region simultaneously with the optical pulse.

Signal stability

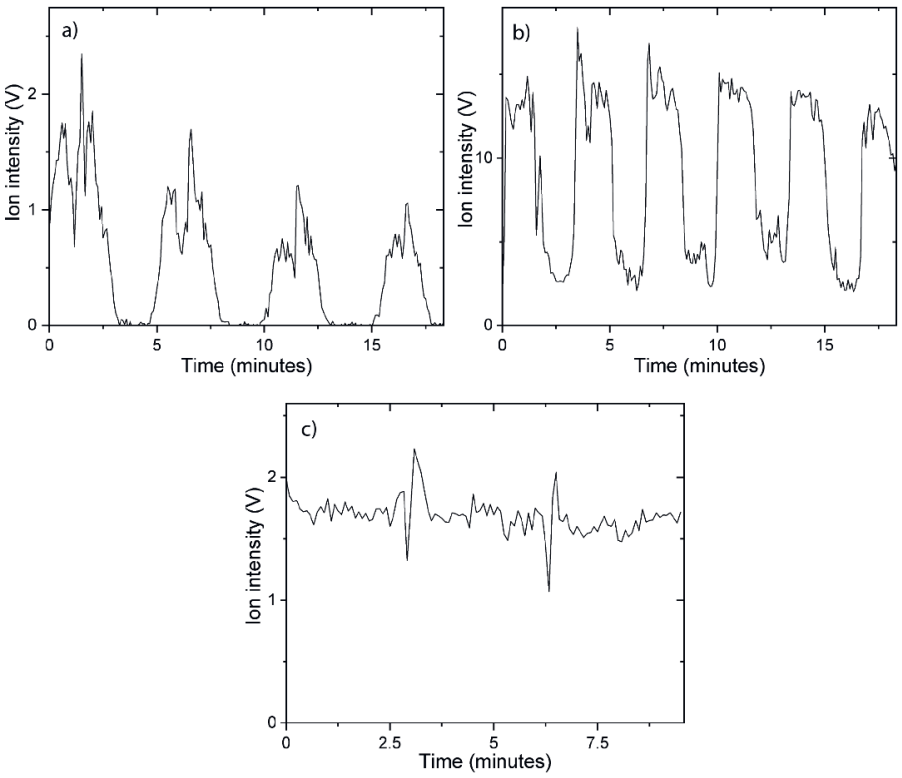

***Figure 2.10**: The production stability of the Co_3^+ cluster before and after modifications to the source: a) signal intensity measured when the bimetallic cluster source was first commissioned, b) the periodic drops in signal intensity correspond to the periodic motion of the target as the stepper motor approaches the target edge, c) improved signal after changing the seal and springs.*

A stable signal from the cluster source is necessary throughout a FELICE scan to obtain a good IR spectrum. A consistent drop in signal or the absence of signal after a period of ablation cannot be used to measure IR spectra. When the bimetallic cluster source was first commissioned, the signal intensity from the source

intermittently disappeared, and the overall signal decreased, as shown in **Figure 2.10a**. For an 8-hour-long beam shift, this is insufficient to obtain IR spectra. Subsequently, it was discovered that this drop in intensity results from carrier gas escaping from the clustering channel, leading to non-uniform cooling of the metal vapours after ablation. Helium can escape primarily through the small holes in the laser insert or through the seal between the source block and the target holder. In the initial design of the cluster source, a Teflon seal is used between the target holder and the source block, enabling smooth sliding. Additionally, four spring-loaded poles are used to push the target holder toward the source block, ensuring contact. The cluster source had a damaged seal and loose springs upon initial commissioning. When these parts are replaced with a polished Teflon seal and stiff springs, the overall signal intensity from the cluster source improves, as shown in **Figure 2.10b**, although periodic fluctuations persist. This periodic drop is directly linked to the sliding position of the target holder on the surface of the source block. The signal drops when the target holder reaches the edge of the source block and improves when it returns from the edges. Therefore, a Viton O-ring is used instead of Teflon, and the signal from the source becomes much more stable, as shown in **Figure 2.10C**. The O-ring is more flexible than Teflon and adapts to the target holder's motion. Additionally, a glass window is inserted above the laser holes to prevent carrier gas from leaking through the laser insert. The transverse moving platform (X) was not sliding smoothly over the longitudinal moving platform (Y), resulting in uneven motion in the X-direction. A customised translation system replaces the old moving system. All these changes helped the cluster source achieve a highly stable signal.

2.2.6 Signal interpretation and analysis

Suppose the cluster and cluster-complexes signal is stable and optimised, and an optimal overlap between the molecular beam and FELICE is achieved. In that case, the infrared spectra can be measured by scanning FELICE over a frequency range. The molecular beam experiment operates at twice the repetition rate of the infrared laser, enabling alternate on/off measurements of the mass spectrometric intensities as a function of IR frequency. At each IR laser frequency, two mass spectra were recorded: a reference spectrum without IR irradiation and a spectrum with IR irradiation (**Figure 2.11a**). For the experiments discussed in this thesis, FELICE operates at 5 Hz, and the experiment runs at 10 Hz. Also, the laser was tuned from one frequency to another with steps of 5 or 10 cm^{-1}. The mass spectra obtained during the FELICE scan are averaged (typically over 50 runs) and recorded by the

LabVIEW programme. Consider $Co_n^+ \cdot CO_2$ complexes as an example, with *n* representing the cluster size. When the IR light is in resonance with the vibrational mode of the $Co_n^+ \cdot CO_2$ complexes, the complexes dissociate upon absorbing several photons, leading to a reduction in their intensity (**Figure 2.11b**). This depletion is quantified by dividing the intensity of the $Co_n^+ \cdot CO_2$ complexes peak under IR irradiation (red) by that without IR irradiation (black) as a function of wavelength. The IRMPD spectrum of $Co_n^+ \cdot CO_2$ complexes is obtained by taking the negative logarithm of this depletion.

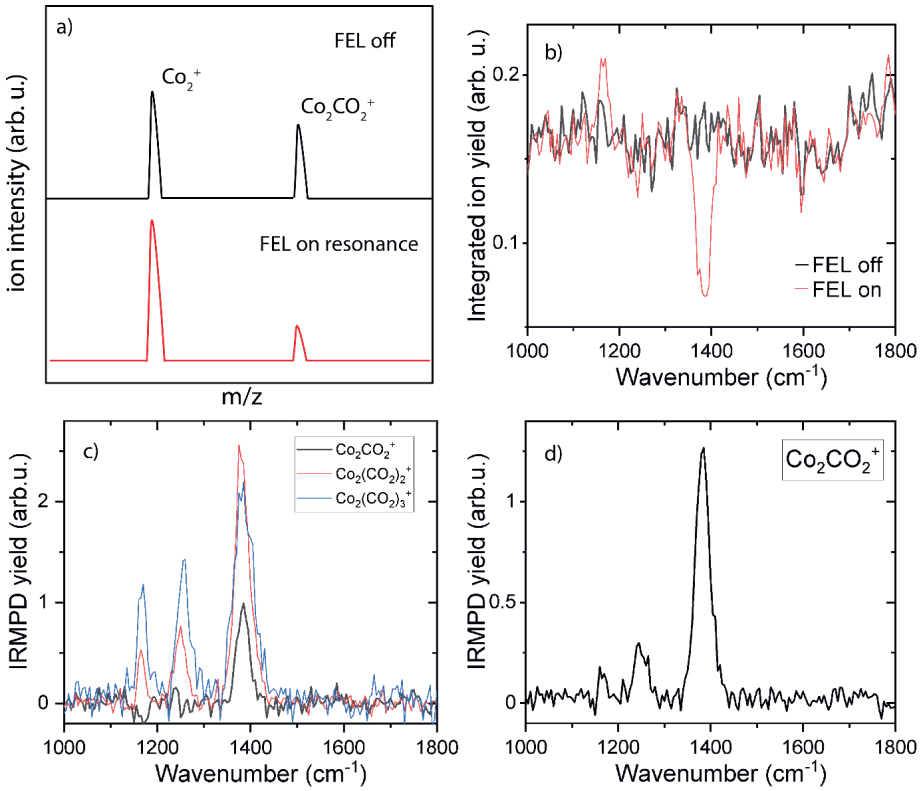

***Figure 2.11**: Panel A shows a schematic of the mass spectrum in the region of Co_2^+ and $Co_2^+ \cdot CO_2$ with the laser off (black) and on resonance (red) with a vibrational mode. Panel B displays the $Co_2^+ \cdot CO_2$ intensity as a function of wavenumber with IR irradiation (red) and without IR irradiation (black). The dip in the signal results from a vibration near 1400 cm^{-1}. In Panel C, the IR spectra of $Co_2^+ \cdot (CO_2)_m$ (m=1,2,3) are shown. The peaks near 1150 and 1250 cm^{-1} for $Co_2^+ \cdot CO_2$ are screened due to the fragmentation of higher-order complexes. Panel D shows the IR spectrum of $Co_2^+ \cdot CO_2$ obtained using the branching ratio approach.*

Assuming *I(ν)* is the signal intensity of the complexes in the mass spectrum with IR radiation, and $I_0(\nu)$ is the signal intensity without IR radiation, *D(ν)* is the depletion, and the depletion yield is calculated as:

$$Y_D(\nu) = -\frac{1}{P(\nu)}\ln\left(\frac{I(\nu)}{I_0(\nu)}\right) = -\frac{1}{P(\nu)}\ln\big(D(\nu)\big),$$

where P(*ν*) is the intracavity laser pulse energy.

In the mass spectrum (in chapter 3), it can be observed that clusters not only bind one CO_2, but also multiple CO_2 molecules to form $Co_n^+\cdot(CO_2)_m$ complexes, with *m* varying with *n*. Complexes with more than one CO_2 can fragment at the same resonant frequency as those with only a single CO_2. Their dissociation into the $Co_n^+\cdot CO_2$ channel can partially or completely screen absorptions in the $Co_n^+\cdot CO_2$ spectrum (**Figure 2.11c**). This can be expressed as $Co_n^+\cdot(CO_2)_m \rightarrow Co_n^+\cdot(CO_2)_{m-1} + CO_2$, where the $Co_n^+\cdot(CO_2)_{m-1}$ also dissociates into $Co_n^+\cdot(CO_2)_{m-2}$ and so on, and finally ends up in $Co_n^+\cdot(CO_2)$. To eliminate these contributions, the branching ratio B_n of CO_2 adducted clusters is calculated as the ratio of the mass spectrometric intensities of all cluster-$(CO_2)_m$ complexes to the sum of the intensities of all clusters and all cluster-$(CO_2)_m$ complexes:

$$\mathrm{B_n} = \frac{\sum_{m=1} I_{n,m}}{\sum_{m=0} I_{n,m}},$$

and then the IRMPD yield *Y(ν)* is presented by taking the logarithmic ratio of the branching ratio *B(ν)* and B_0, with IR and without IR irradiation (**Figure 2.11d**):

$$Y_B(\nu) = -\frac{1}{\mathrm{P}(\nu)}\ln\left(\frac{\mathrm{B}(\nu)}{\mathrm{B_0}(\nu)}\right).$$

When cluster-molecule complexes absorb IR radiation, the population of remaining parent ions decreases exponentially. Taking the logarithm transforms this exponential decay into a linear relationship, proportional to the IR absorption strength.

2.3. Density Functional Theory

Density Functional Theory (DFT) is a quantum mechanical approach used to describe the electronic structure and geometry of atoms and molecules. To be precise, DFT is a formalism that describes the many-electron wavefunction of an atom or molecule, which can be used to calculate geometries and therefore vibrational frequencies,

similarly as other common methods, such as MP2 or coupled-cluster. Basically, the total electronic energy is calculated and minimised as a function of geometry and spin multiplicity. To understand the experimental IR spectra presented in this thesis, computational IR spectra are obtained through DFT calculations. This aids in predicting the geometrical structure of the clusters and their complexes formed during the experiment. To perform DFT calculations, the most plausible trial structures of the clusters can be identified in the literature or through structural searches. If the ground state spin multiplicity of the cluster is unknown, the trial structures are optimised by DFT for a range of spin multiplicities,[131] which allows a determination of the preferred spin configurations for the clusters, as a function of geometry. Finally, energies and vibrational spectra can be computed.

A brief overview of the underlying principles of DFT will be provided here. The Hamiltonian describes the total energy of a molecular system as $H = T + V + U$, where T represents the kinetic energy of the system, V is the potential energy of the electrons in the electric field originating from the nuclei, and U is the potential energy of electron-electron repulsion. In quantum mechanics, the behaviour of a system of particles is described by the Schrödinger equation, $H\Psi = E\Psi$, where Ψ is the wavefunction that describes the system. However, the wavefunction is very complex as it depends on all electronic and all nuclear coordinates. To simplify this, the Born-Oppenheimer approximation is introduced. In this approximation, the total wavefunction can be separated into a product of an electronic and a nuclear wavefunction. It recognises that the nuclei are much heavier and move more slowly than electrons; therefore, a good approximation can be achieved only by solving the electronic Schrödinger equation assuming that the nuclei are fixed in space. Still, the wavefunction Ψ for a system composed of many interacting electrons is highly complex because it depends on the coordinates of all electrons simultaneously, in addition to the presence of the U term due to electron-electron interactions, which makes it, in principle, impossible to find an analytical solution to the electronic Schrödinger equation.

In the DFT approach, the system is described by its electron density $\rho(r)$, rather than its wavefunction. Here, the electron density relies solely on three spatial variables, regardless of the number of electrons. According to the Hohenberg-Kohn theorem,[132] the energy functional can be expressed as a functional of the electron density $\rho(r)$ and the external potential $V(r)$, in which all the electrons experience the same external potential:

$$E[\rho(r)] = \int V(r)\rho(r)dr + F[\rho(r)],$$

and where

$$F[\rho(r)] = T[\rho(r)] + V_{ee}[\rho(r)],$$

is known as the Hohenberg-Kohn functional, which does not depend on the external potential and is therefore intrinsic to the system of electrons. *F[ρ(r)]* is the sum of two terms – the kinetic energy functional and the electron repulsion functional. This latter, in turn, is the sum of a classical electron repulsion and a nonclassical exchange functional.

The practical use of DFT became feasible through the Kohn-Sham method.[133] They proposed replacing the real, interacting system of electrons with a reference system of non-interacting electrons that guarantees the same electron density, which obeys the so-called Kohn-Sham equation. In this equation, the reference system can easily be separated into one-electron equations, and its wavefunction can be described as a linear combination of eigenstates. The one-electron equations can be applied to express the electron density:

$$\rho(r) = \sum_{i=1}^{n} |\varphi_i(r)|^2,$$

and the functional *F[ρ(r)]* can be calculated as:

$$F[\rho(r)] = T_s[\rho(r)] + J[\rho(r)] + E_{xc}[\rho(r)],$$

where $T_s[\rho(r)]$ is the kinetic energy of the non-interacting system, which can be calculated, *J[ρ(r)]* is the classical Coulomb term, which is known from classical electrodynamics, and $E_{xc}[\rho(r)]$ is the exchange correlation functional, which remains unknown. Many exchange correlation functionals have been developed so far, and are chosen based on their ability to explain the obtained experimental data. The DFT calculations discussed in this thesis primarily employ the TPSSh functional.[134]

The process of solving the Kohn-Sham equations is iterative, involving a self-consistent field cycle. An initial guess for the electron density *ρ(r)* is made, the effective potential is calculated, and the Kohn-Sham equations are solved to obtain new orbitals. From these orbitals, a new density is constructed, and the cycle is repeated until the total energy converges to a determined threshold. This provides the ground-state energy for the given arrangement of nuclei. In each cycle, not only are the orbitals and energy calculated, but also the forces are determined as the energy gradient with respect to nuclear positions. The atoms are then moved in the direction of these forces to minimise the energy, and the Kohn-Sham equations are

solved for the updated geometry. This process is called geometry optimisation and is repeated until a minimum energy configuration (forces on all atoms become negligible) is reached. Additionally, the spin can be varied, in which case the previous cycles are repeated for each various spin multiplicities. When the minimum energy structure is found, the vibrational frequencies can be calculated from the second derivative of the potential energy surface, and intensities can be determined by the change in dipole moment along each vibrational mode. A detailed account of DFT applications is provided elsewhere.[135]

3 Size-selective CO_2 activation by vanadium-doped cobalt clusters

Abstract

CO_2 activation is the primary step for CO_2 reduction to C2 products. To understand the activity of bimetallic catalysts towards CO_2, and in particular the role of dopant elements, we experimentally studied CO_2 adsorption on pure and vanadium-doped cationic cobalt clusters. Doped and pristine clusters are reacted with CO_2 in a flow tube-like reaction channel, and resulting cluster-CO_2 products are characterized by free-electron laser-based IR spectroscopy. The spectra for CO_2 adsorbed on pure Co_n^+ clusters are highly similar for each cluster size studied, and indicate that CO_2 is mostly physisorbed on the cluster. However, substituting a Co atom with a single V atom results in strongly varying IR spectra for $VCo_{n-1}^+ \cdot CO_2$ adducts, indicative for size-selective activation, dissociation and even cluster oxidation. The size selectivity demonstrates how a fine interplay between dopant element and cluster size could be made instrumental in tuning the activity of catalyst materials.

This chapter is adapted from:
D. Pradeep, B. Zamora Yusti, R.T. Zijlstra, M. Szalay, T. Höltzl, L. Nyulászi, J. M. Bakker, J. Phys. Chem. Lett. 2026, 17 (31), 9008-9015.

DP and RTZ carried out the experimental work; BZY, LN, and TH performed DFT calculations.

3.1. Introduction

Gas phase clusters are excellent model systems for investigating the interaction between metals and molecules, and in particular as model systems for the active sites of more complex catalysts.[57, 58, 66, 136] Complete control over the charge, size, and composition of clusters in the gas phase helps in understanding the interaction at the molecular level, and such knowledge is important for the rational design of future catalyst materials. Given that CO_2 neutrality may be achieved via the capture of CO_2 and its conversion into value-added chemicals like methanol, ethanol and other C2 products,[137] understanding the binding nature of CO_2 on different metal clusters or ions has attracted broad research interest. Spectroscopic studies show that CO_2 exhibits little to no activation when adsorbed on positively charged metal ions, e.g refs [72, 81] In contrast, when adsorbed on anionic metal ions the CO_2 molecule is activated.[73] This difference is attributed to the ability of the anion to donate electron density into the π^* anti-bonding orbital of CO_2, leading to a characteristic bent, carbonate-like structure. This picture is the same when evaluating polyatomic metal cluster ions: CO_2 adsorption on cationic copper clusters adsorb weakly via physisorption,[74] whereas CO_2 activation and dissociation were observed on specific sizes of anionic Pt_n^- and Co_n^- clusters.[75, 76]

Catalyst materials, however, tend not to have formal charges of +1 or -1, but one that is dependent on the charge donation capabilities of the support. Moreover, catalyst materials are usually much more complex than the single-element picture of clusters, as evidenced by the bimetallic nature of the industrial $Cu/ZnO/Al_2O_3$ catalyst.[13, 83] It is therefore of interest to investigate how the elemental composition of a cluster affects its activity towards CO_2. However, experimental studies of CO_2 involving multiple metal elements are, to the best of our knowledge, not extant. In this work, we experimentally and computationally investigate the dopant effect on the adsorption of CO_2 on cationic Co_n^+ and VCo_{n-1}^+ clusters. We experimentally characterize the adsorption product using mass spectrometry and infrared spectroscopy. We chose cobalt clusters because CO_2 activation or dissociation has been reported for their anions,[76] as well as for ease of mass spectrometric detection (cobalt has no isotopes). As a dopant, we chose vanadium, an oxophylic element with a V^+—O bond energy of 6 eV.[108] Additionally, vanadium-doped cobalt clusters were shown to have an increased reaction rate for H_2 adsorption.[86] Furthermore, we perform DFT calculations to benchmark the experimental IR spectra and potential energy surfaces to understand the wildly varying outcomes for CO_2 on cobalt and doped-cobalt clusters.

3.2. Experimental and computational methods

Experiments were carried out in the molecular beam instrument installed within the cavity of the free-electron laser FELICE, discussed in detail in Chapter 2 and elsewhere.[123, 124] In short, cationic V-doped Co clusters were produced in a dual-target dual-laser ablation source,[87] operated at room temperature. Separate vanadium and cobalt were ablated by two loosely focused, frequency-doubled, pulsed Nd: YAG lasers (532 nm, pulse energies 7–8 mJ). Right before ablation, helium (stagnation pressure of 8 bar) was injected into the formation chamber of the source using a pulsed valve (Jordan TOF Products, Inc.). The helium collisionally cooled the metal vapours from both targets and promoted (bimetallic) cluster formation, while simultaneously entraining the formed clusters towards a reaction channel. Here, the clusters were reacted with CO_2, injected via a second pulsed valve (Parker General Valve) at a stagnation pressure of 1 bar, resulting in the formation of cluster-CO_2 complexes.

The mixture of helium, clusters and cluster-CO_2 complexes was then supersonically expanded into a vacuum to form a molecular beam. The beam was collimated by a 2-mm diameter skimmer and further shaped by a 2-mm high slit aperture to match the beam size to the IR light beam, which it crossed at a 35-degree angle. To ensure spatial overlap between the laser and molecular beams, as well as to control the laser fluence in the interaction region, the whole molecular beam instrument can be moved horizontally and vertically with respect to the fixed focus of the IR beam. After interaction with the IR laser, all ions were extracted into a reflectron time-of-flight mass spectrometer (Jordan TOF Products, Inc.) and detected using a microchannel plate-based detector. To prevent complexes that did not interact with the IR laser to reach the detector, a slit aperture is positioned in the flight path directly above the extraction plates.[124]

FELICE produces IR light in the 4.5–100 µm (100–2200 cm^{-1}) spectral range, although in the current work only the 600–2200 cm^{-1} range was used. It has a distinct temporal pulse structure, with a macro pulse (10 µs, 5 Hz repetition rate) consisting of a train of micro pulses (0.2-10 ps pulse width, 1 GHz repetition rate). It has high pulse energies typically between 0.9 and 1.3 J, and a spectral bandwidth between 0.5 and 3 % full width at half maximum (FWHM) of the central frequency. Pulse energies and spectral properties were monitored by outcoupling a small fraction of the laser beam.

When the IR laser is in resonance with a vibrational mode of the cluster-molecule complexes, the complexes can dissociate after absorption of multiple photons, leading to a reduction in their detected ion intensity. To detect this depletion, the experiment ran at a 10 Hz repetition rate, with FELICE operating at 5 Hz and reference mass spectra were recorded when FELICE was off. Complexes of clusters with two or three CO_2 molecules adsorbed can also be formed, and these may fragment at the same resonant frequency as that of the clusters with a single CO_2 molecule adsorbed. This can result in the partial screening or even complete elimination of the absorption band for the cluster with a single CO_2 molecule by the ingrowth from fragments of the larger complexes. To eliminate this contribution to the spectrum of the cluster with a single CO_2 adsorbed, the branching ratio *B* of the summed mass-spectrometric intensities I_m of all cluster·$(CO_2)_m$ (m=1–4) complexes formed to the sum including all clusters and cluster complexes (m=0–4) is used (see details in Chapter 2).

The adsorption concentration dependence experiment is conducted by adjusting the voltage amplitude driving the second pulsed valve. The partial pressure of CO_2 is established by measuring the source chamber pressure (so not in the flow tube itself) as a function of voltage amplitude in the absence of helium injected in the ablation source. The CO_2 dosage is controlled by increasing the amplitude of the control pulse that opens the General Valve, while keeping the pulse length constant. The partial pressures are measured with a cold-cathode gauge in the absence of helium. Cluster and adsorption product mass intensities were normalised by taking the branching ratio of the mass-spectrometric intensities of clusters, cluster oxides, or cluster-CO_2 complexes to the total sum of all clusters and cluster complexes.

To computationally investigate the effect of doping, DFT calculations were performed on four cationic clusters: Co_4^+, Co_5^+, VCo_3^+, and VCo_4^+, using the Gaussian 16 package.[138] All initial geometry optimisations and frequency calculations were carried out using the BP86[139] functional with the lanl2dz[140]/auto basis set. Since the ground-state spin multiplicities of the V-doped clusters were unknown, a range of spin states was explored: from 1 to 21 for VCo_4^+, based on the high-spin character of the isoelectronic Fe_5 cluster (spin multiplicity of 19),[141] and from 2 to 12 for VCo_3^+. For Co_4^+ and Co_5^+, the spin multiplicities were taken from the literature[142]. Once the lowest-energy spin multiplicity was identified for each cluster, the CALYPSO structure prediction method was used,[143] which is based on a particle swarm optimization (PSO) algorithm.[144] The resulting low-energy structures were then reoptimized at the TPSSh/def2-TZVP[134, 145] level, yielding the lowest energy structure for the bare

clusters. Subsequently, to generate input structures for geometry optimisation of cluster-CO_2 complexes, we used an in-house code[103] to systematically investigate carbon dioxide adsorption product structures in different binding motifs to low-energy bare metal clusters. Details of the different bare clusters and CO_2 binding modes are shown in Table S1 of the Appendix. To explore the full reaction pathways for the CO_2 activation and dissociation reactions, intermediates and products were located for the cationic clusters. The Freezing String Method (FSM)[146] was used to locate good guesses of the transition structure geometries and the minimum energy pathways connecting the reactant and product structures. This initial guess geometry of the transition structure was further refined using the STQN method, as implemented in the Gaussian software and requested through the QST3 option.[138] The first-order nature of the located saddle point was further verified by ensuring that the imaginary frequency corresponded to the vibrational normal mode of the atoms involved in bond formation or breaking. Once the transition state geometry was located, Intrinsic Reaction Coordinate (IRC) computations were performed to explore the reaction pathway in the vicinity of the transition state and to verify the proposed energy pathway. Harmonic vibrational frequencies for the product structures were calculated to ensure a true minimum was achieved, as well as to compare with the experimental IR spectrum. The calculated harmonic vibrational stick spectra were, without frequency scaling, convoluted with a 15 cm^{-1} full-width at half-maximum Gaussian line shape function.

3.3. Results and discussions

3.3.1 Mass spectrometry: CO_2 adsorption on pure Co_n^+ and VCo_{n-1}^+ clusters

Figure 3.1 shows the typical mass distribution of cationic cobalt and vanadium-doped cobalt clusters interacting with CO_2. The mass spectrum is presented on a horizontal scale relative to the masses of pure cobalt clusters to enable comparison for the various cluster sizes. Mass peaks for cationic pure cobalt clusters (at 0) and single vanadium atom-doped cobalt clusters (at –8) are depicted by orange and magenta bars, respectively. Mass peaks at +45 and +37 correspond to the adduct of these clusters with one $^{13}CO_2$ molecule, and are indicated by bars adopting the same color convention as for the bare clusters. A more detailed assignment of all mass peaks is shown in **Figures 3.2** and **3.3**. From the congestion in the upper panels it is clear that the smaller clusters are more prone to form adducts with CO_2, illustrated by the observation of $V^+(CO_2)_m$ and $Co^+(CO_2)_m$ (both m=1-6), $VCo^+(CO_2)_m$ (m=1-3). Carbon-13 isotopically labelled CO_2 was employed to prevent the mass overlap

between these smaller clusters with numerous CO_2 molecules adsorbed and larger clusters with one CO_2 molecule. For example, the mass of $VCo^+(^{12}CO_2)_5$ (m/z=330) is close to that of $VCo_4^+(^{12}CO_2)$ (m/z=331). Along the orange bar (+45), indicative for the mass of $Co_n^+CO_2$, we observe for all *n* a mass peak suggesting the complexation of all sizes with at least a single CO_2 molecule. Along the magenta bar (+37, $VCo_{n-1}^+CO_2$), four out of the six cluster sizes displayed show a mass peak (VCo^+, VCo_2^+, VCo_5^+, and VCo_6^+), whereas no such peak is observed for VCo_3^+ and VCo_4^+. The mass spectrum without CO_2 (see **Figure 3.2**) shows slight contamination from oxides. This could be due to residual oxygen or water in the gas lines, or due to an oxide layer on the metal targets. However, upon reaction with CO_2, the mass peaks for VCo_3O^+ and VCo_4O^+ (at +8) as well as for $VCo_3O_2^+$ and $VCo_4O_2^+$ (at +24) show a marked increase with CO_2 injection. The absence of $VCo_3^+{\cdot}CO_2$ and $VCo_4^+{\cdot}CO_2$ mass peaks may suggest that CO_2 dissociates upon adsorption and that the carbonyl formed is eliminated from the cluster. An observed appearance of oxides on VCo_{n-1}^+ may reflect this.

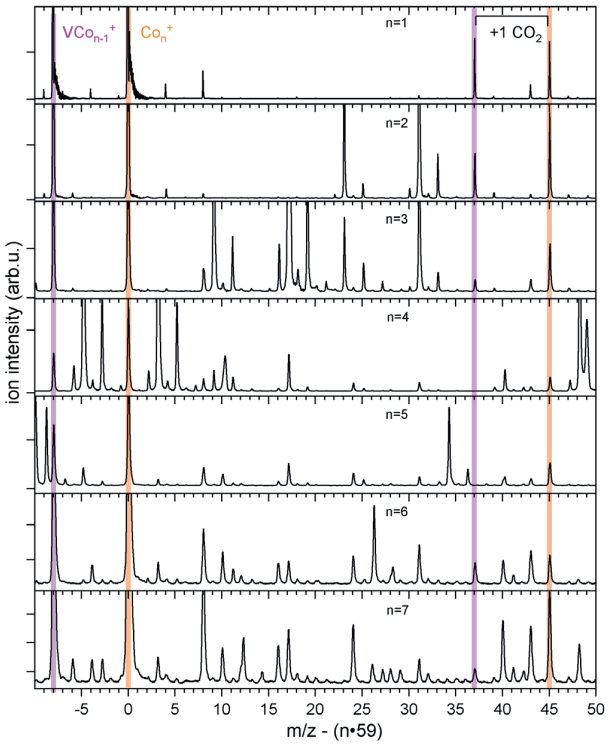

***Figure 3.1**: Mass distribution of cationic Co and V-doped Co clusters (orange and magenta bars) reacted with $^{13}CO_2$ (same colour coding). Mass peaks corresponding to $VCo_3CO_2^+$ (n=4) and $VCo_4CO_2^+$ (n=5) are absent in the mass spectrum.*

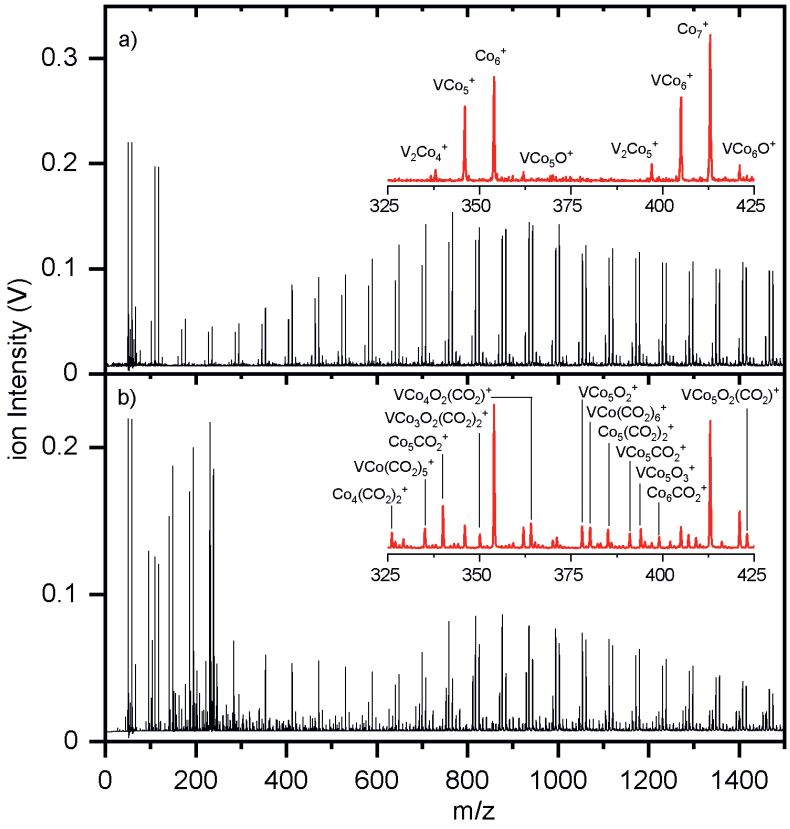

***Figure 3.2**: (a)Mass spectrum of a distribution of cationic pure and vanadium-doped cobalt clusters. The zoom-in panel highlight the distribution close to the Co_n^+ (n=6 and 7) mass peaks. A single oxide on VCo_5^+ and VCo_6^+ clusters is observable. (b) Mass spectrum of a distribution of cationic pure and vanadium-doped cobalt clusters reacted with $^{13}CO_2$. The zoom-in panel highlights all the cluster-CO_2 and cluster-oxide complexes formed.*

To analyse the formation of oxides on clusters during CO_2 reactions, we analyse the concentration dependence of their formation. **Figure 3.4** shows the mass peak intensities of various reaction products as a function of CO_2 partial pressures. The vertical axis represents the branching ratio, indicating the proportion of cluster or reaction product relative to the sum of all. Panels *a* and *b* show the product concentration dependences of VCo_3^+ and VCo_5^+ reacted with $^{13}CO_2$. As the CO_2 concentration increases, the bare $VCo_{3,5}^+$ clusters (black squares) are consumed, while $VCo_{3,5}O^+$ (red circles) and $VCo_{3,5}O_2^+$ (green triangles) increase. Notably, no formation of $VCo_3^+{\cdot}CO_2$ (blue squares) is detected, supporting the hypothesis of CO_2 dissociation followed by CO desorption from the cluster. In the reaction with VCo_5^+ (panel *b*), a clear correlation between formed $VCo_5^+{\cdot}CO_2$ is observed, although there

is a simultaneous increase in the formation of VCo_5O^+ and $VCo_5O_2^+$. This could indicate that some CO elimination still occurs over VCo_5^+, but not to the extent of VCo_3^+. To rule out atmospheric oxide contamination, the experiment is repeated using $C^{18}O_2$ (panels *c* and *d*). Consistent with the observations for $^{13}CO_2$, with increasing $C^{18}O_2$ concentration, the $VCo_{3,5}{}^{18}O^+$ (cyan hexagons) and $VCo_{3,5}{}^{18}O_2{}^+$ (purple stars) product formation rises, while $VCo_{3,5}{}^{16}O^+$ (red circles) is decreasing, suggesting it is consumed to form $VCo_{3,5}{}^{16}O^{18}O^+$ (not shown here because of a mass overlap). Meanwhile, no formation of $VCo_3{}^+{\cdot}C^{18}O_2$ (blue diamonds) and $VCo_{3,5}{}^{16}O_2{}^+$ (green triangle) is detected, confirming that the oxides arise from carbon dioxide and not from external contamination.

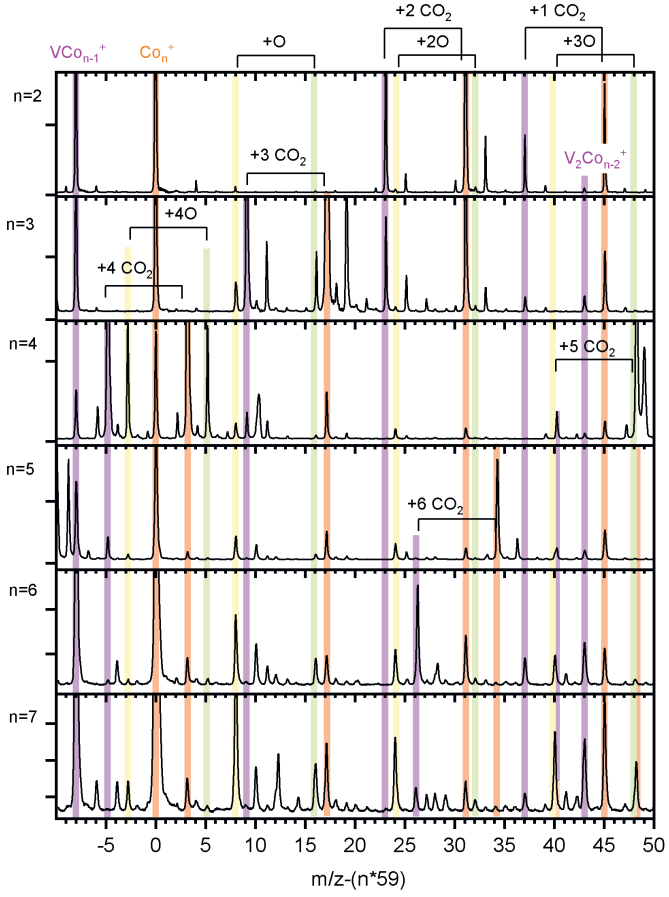

***Figure 3.3**: Mass distribution of Co and V-doped Co clusters (orange and magenta bars) reacted with $^{13}CO_2$. Adducts with one (at +45 and +37) or multiple CO_2 molecules are indicated using the same colour coding as the bare clusters. Oxidized Co and V-doped Co clusters, such as Co_nO^+ (+16) and VCo_nO^+ (+8), are indicated by green and yellow bars.*

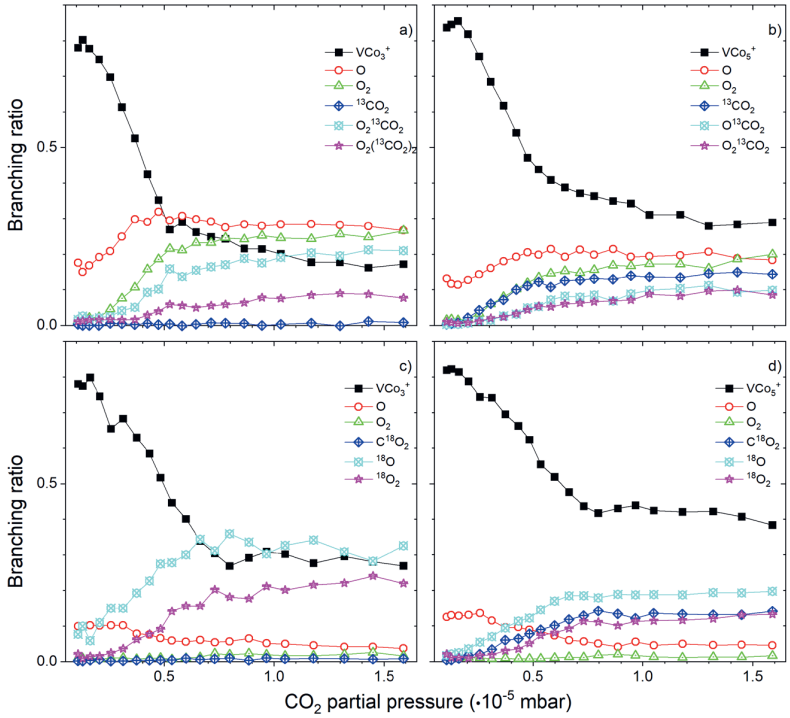

***Figure 3.4**: Product distribution dependence of $VCo_n^+ + CO_2$ on CO_2 partial pressure for n=3 (panels a and c) and n=5 (panels b and d). To rule out oxide product formation due to air contamination, the experiments are carried out using $^{13}CO_2$ (panels a and b) and $C^{18}O_2$ (panels c and d)*

3.3.2 Spectroscopy of $Co_n^+ \cdot CO_2$ and $VCo_{n-1}^+ \cdot CO_2$ products

Figure 3.5 displays the IR spectra for $Co_n^+ \cdot {}^{13}CO_2$ (black traces) and $VCo_{n-1}^+ \cdot {}^{13}CO_2$ (red traces) for *n*=2-7 in the 600–2200 cm^{-1} spectral range. IR spectra of $Co_n^+ \cdot {}^{12}CO_2$ and $VCo_{n-1}^+ \cdot {}^{12}CO_2$ for cluster sizes where mass overlap did not prevent their recording are included in **Figure 3.6** . The spectra for pure cobalt clusters are all very similar, with four bands around 625 cm^{-1}, 1150 cm^{-1}, 1250 cm^{-1}, and 1350 cm^{-1}, respectively. The exception is formed by the spectrum for $Co_4^+ \cdot CO_2$ which shows in addition to the bands mentioned two extra bands at 689 and 1792 cm^{-1}.

The experimental spectrum of $Co_5^+ \cdot CO_2$ is representative for other cluster sizes excepting Co_4^+. It has bands at 629, 1141, 1217 and 1349 cm^{-1}. Three of these frequencies match well with bands observed for the free CO_2 molecule:[147] the bending vibration (ν_2) at 667 cm^{-1}, and the two components of the Fermi resonance between symmetric stretch (ν_1) and ν_2 overtone at 1388 cm^{-1} and 1285 cm^{-1}, respectively and the asymmetric stretch vibration (ν_3). The band detected at 1141

cm^{-1} is close to half the frequency of the asymmetric stretch (ν_3) of CO_2 (2349 cm^{-1}), likely made visible by a small fraction of second harmonic light present in the FEL cavity. The same four bands, including the overtone were also observed in our previous work on CO_2 adsorption onto cationic copper clusters,[74] suggesting the inactivity of cationic clusters of all late 3d transition metal elements. Finally, we note that the spectrum of $Co_5^+ \cdot CO_2$ shows a shallow plateau in the 1000–2000 cm^{-1} spectral window. We do not have a good explanation for this slope, although we note that such non-resonant signals have been seen for other species, and speculated to be due to low-lying electronic states.[148] Recently, such absorptions were also reported for $Co_n^+ \cdot Kr$ (n=4-15).[149]

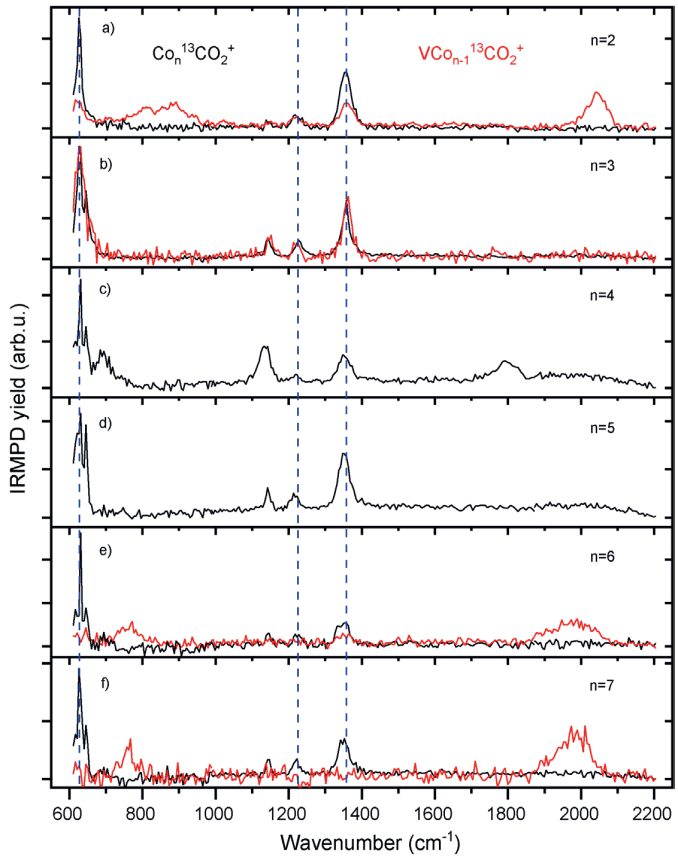

***Figure 3.5**: IR spectrum for $^{13}CO_2$ adsorbed on pure (black) and V-doped (red) cationic Co clusters for sizes n= 2-7. The vertical dashed lines indicate the vibrational frequencies of the free CO_2 molecule. Panels c) and d) only display a spectrum for $Co_nCO_2^+$ because $VCo_3CO_2^+$ and $VCo_4CO_2^+$ were not formed.*

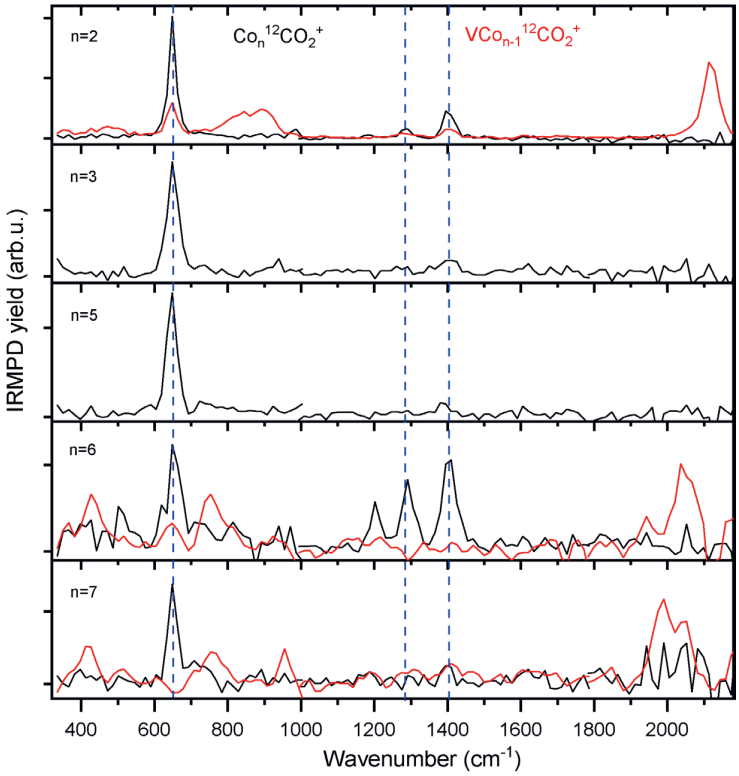

***Figure 3.6**: IRMPD spectrum for $^{12}CO_2$ adsorbed on cationic Co (black line) and V-doped Co (red line) clusters for cluster sizes, n = 2-7. The vertical dashed lines indicate the vibrational frequencies of the free CO_2 molecule. These spectra show bands slightly blue-shifted from those detected for $^{13}CO_2$, consistent with their lower effective mass. Due to the mass overlap of $VCo_2{}^+{\cdot}CO_2$ (n = 3), $Co_4{}^+{\cdot}CO_2$, and $VCo_3{}^+{\cdot}CO_2$ (both n = 4), and $VCo_4{}^+{\cdot}CO_2$ (n = 5) with other masses, the IR spectra are not reliable.*

While the inactivity of $Co_5{}^+$ is representative for all pure cobalt clusters, it is not for $Co_4{}^+$. Its spectrum (**Figure 3.5c**) exhibits a similar set of bands with maxima at 624 cm^{-1}, 1135 cm^{-1}, 1219 cm^{-1}, 1348 cm^{-1} but has two extra bands with maxima at 689 cm^{-1} and 1792 cm^{-1}, respectively. These peak positions are not dissimilar from bands reported for CO_2 adsorption on the anionic Pt and Cu_xO_y clusters, around 800, 1100 and 1600 cm^{-1}, attributed to activated CO_2. [75, 77] For $Co_4{}^+$, the three bands at 689 cm^{-1}, 1135 cm^{-1} (most likely the mix of two bands) and 1792 cm^{-1} therefore suggest the presence of a mixture of physisorbed and activated CO_2 on the $Co_4{}^+$ cluster. This is further substantiated by a comparison of the experimental IR spectrum of $Co_4{}^+{\cdot}CO_2$ with the calculated spectra in **Figure 3.7**.

For the doped clusters, the spectral fingerprints change significantly. Only the spectrum for $VCo_2{}^+{\cdot}CO_2$ (**Figure 3.5b**, red trace) shows the same bands indicative for

physisorbed CO_2. However, this is contrasted by the spectra for $VCo^+ \cdot CO_2$, $VCo_5^+ \cdot CO_2$ and $VCo_6^+ \cdot CO_2$, where, along with the bands diagnostic for physisorbed CO_2, an intense extra band around 2000 cm^{-1} appears and a broader band around 800 $cm^{-1}$is visible. The former band is diagnostic for the stretch vibration of the CO dissociation product (2143 cm^{-1} in free CO)[150, 151], whereas the latter may be a CoO or VO stretch mode. A similar band was also observed in our previous work on CO_2 adsorption on anionic C-doped Cu clusters,[79] leading to conclude on dissociative adsorption of CO_2. The bands diagnostic for physisorption suggest part of the product population is collisionally cooled by the helium carrier gas and trapped before the dissociation barrier. For larger sizes (n>6) the spectra no longer show these physisorption bands.

Figure 3.7 shows a comparison between the experimental spectrum of $Co_4^+ \cdot CO_2$ (3.7A) to calculated spectra (3.7BC). As basis, we used the tetrahedral Co_4^+ cluster with octet multiplicity, which has the lowest energy calculated, consistent with previous experiments.[117] Computed spectra are shown for two possible binding geometries. One has linear CO_2 (panel B) physisorbed with an oxygen atom η1-bound to the cobalt atom. A second (panel C) has an activated CO_2 moiety, i.e., CO_2 forms a bent structure and binds with one oxygen in η1 configuration and with the carbon bound in bridge configuration to two Co atoms. The binding energy (BE) of the CO_2 adduct is calculated as the energy difference between the Co_4^+-CO_2 product and that of the separate reactants ($E(Co_4^+)$ + $E(CO_2)$). The lowest energy of these structures is for activated CO_2 at –89 kJ/mol, by a margin of 41 kJ/mol with respect to the physisorbed adduct at –48 kJ/mol. When comparing the experimental spectrum with panel B, it can be seen that the experimental band I at 624 cm^{-1} is in good agreement with the calculated band at 668 cm^{-1}, the CO_2 bending vibration. Bands IV and V at 1219 cm^{-1} and 1348 cm^{-1} are reproduced by the single band at 1237 cm^{-1}: the Fermi resonance, an anharmonic coupling effect, is not replicated by the harmonic calculations, only the symmetry-broken ν_1 stretch vibration. When comparing with panel C, the experimental bands II, III and VI at 689, 1135, and 1792 cm^{-1} are in fair agreement with the theoretically predicted peaks at 695, 1170, and 1796 cm^{-1} for bend, symmetric stretch and antisymmetric stretch vibrations of activated CO_2. The populations are estimated from the depletion spectra for the $Co_4^+ \cdot CO_2$, showing a 60% depletion for physisorbed bands compared to a 40% for activated CO_2 bands.

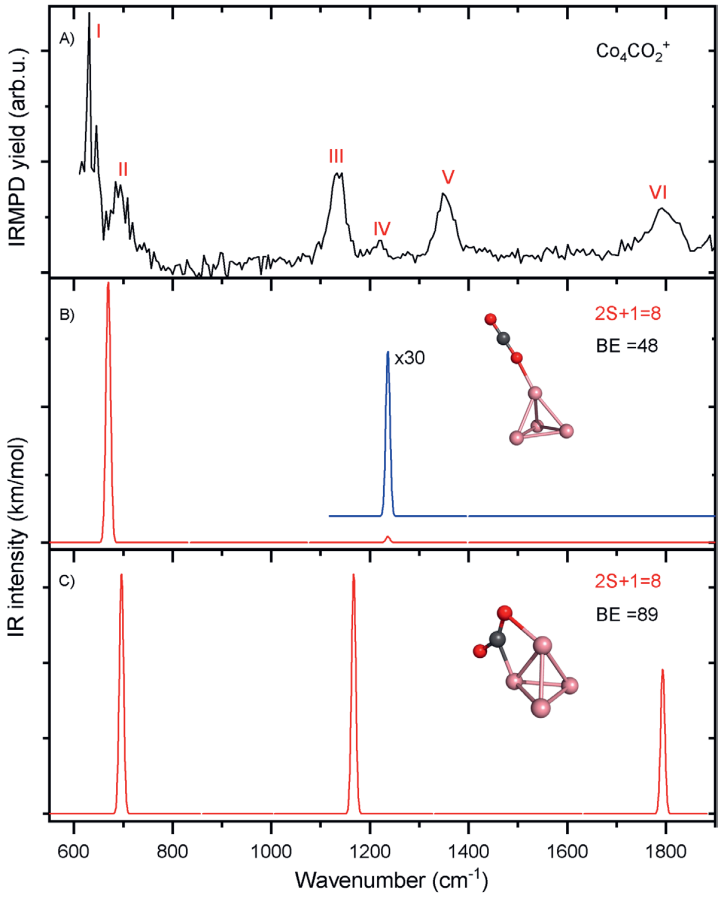

***Figure 3.7**: Experimental IR spectrum of $Co_4^+ \cdot CO_2$ (panel A) compared to the calculated vibrational spectra of two low-energy structures of physisorbed (panel B) and activated CO_2 (panel C) adsorption products, both with spin multiplicity 2S+1=8. Binding energies (BE) are shown in kJ/mol.*

3.3.3 Reaction paths for the adsorption and activation of CO_2 on Co_n^+ and VCo_{n-1}^+ clusters

To understand the absence of CO_2 adsorption products for VCo_3^+ and VCo_4^+ and the apparent oxidation of these clusters, we turn to theoretical computations of the adsorption reaction on VCo_3^+. To be able to compare the doped cluster with the pure cobalt cluster, we compare these results with the same reaction over Co_4^+. For both reactions, the reaction pathways are evaluated and shown in **Figure 3.8** . For Co_4^+, the octet surface is evaluated, and for VCo_3^+, the reaction path on the quartet surface is shown.

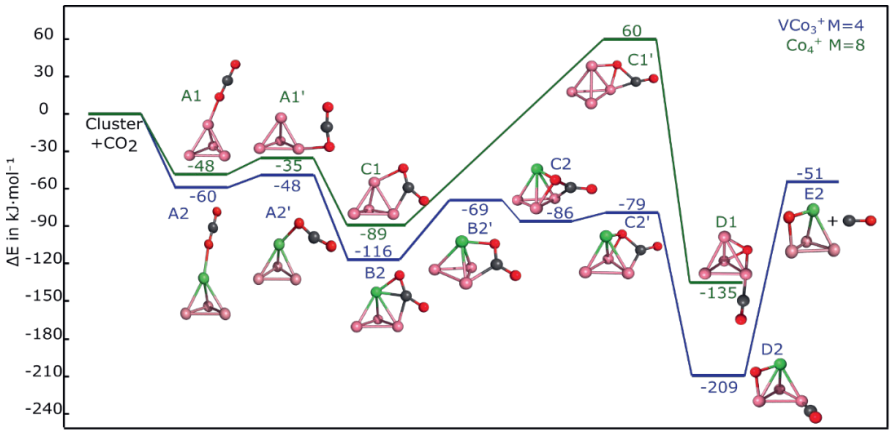

***Figure 3.8**: Reaction paths for the adsorption, activation, and dissociation of CO_2 on Co_4^+ and VCo_3^+ clusters. Relative energies are given with respect to the most stable cluster (our global minimum for the respective size) + free CO_2 molecule. The various spin surfaces are color-coded, minima are labelled by capitals and transition states by primed capitals. V, Co, C, and O atoms are depicted by green, pink, black, and red spheres, respectively. Calculations were done using the TPSSh/def2-TZVP combination.*

For $Co_4^+ \cdot CO_2$ (the green line in **Figure 3.8**), the entrance complex is formed by the linear CO_2 adsorbed onto the apex of the tetrahedral Co_4^+ cluster, with a CO_2 BE of 48 kJ/mol (structure A1). To form a partially bent CO_2 structure on the cluster (C1), the linear CO_2 rotates towards the cluster over transition state A1' at –35 kJ/mol keeping one oxygen atom bound to one cobalt atom and with the carbon atom bound to a bridge site of Co_4^+ at an energy of -89 kJ/mol (structure C1). For dissociation, the bent CO_2 rearranges on the cluster so that the bound oxygen atom moves to the bridge site and the carbon to an atop site (transition state C1'). When the C=O bond is ruptured the atop bound O atom migrates to a hollow site, and the C=O to an on-top Co site (D1). The final product is exothermic at –135 kJ/mol, but the barrier for CO_2 dissociation (C1') is endothermic at +60 kJ/mol, barring the reaction from proceeding.

The reaction over VCo_3^+ is depicted by the blue line in **Figure 3.8** . Like for Co_4^+, the entrance complex is formed by linear CO_2 adsorbed on an atop position on a vanadium atom of the tetrahedral VCo_3^+ cluster, with a CO_2 binding energy of 60 kJ/mol (structure A2). Adsorption on the cobalt atoms is less favourable with a BE of 51 kJ/mol. Fully analogous to Co_4^+, the CO_2 molecule rotates towards the cluster over TS A2' (-32 kJ/mol) to form a bent CO_2 moiety (B2), but now significantly more strongly bound at –116 kJ/mol (compared to –89 kJ/mol). To dissociate CO_2 on the cluster, the carbon atom shifts toward a Co-Co bridge site (B2' and C2) and upon rupturing the OC–O bond, CO binds to one of the cobalt atoms in on-top

configuration (D1). The oxygen atom on the vanadium center migrates to a V–Co bridge site. The dissociated O–VCo_3^+–CO structure is much more stable than the equivalent product for Co_4^+, with a rate-limiting barrier of 47 kJ/mol between B2 and B2' that is surpassable using the reactants' energy. The reaction pathway calculations further examined the likelihood of carbonyl elimination following CO_2 dissociation on the VCo_3^+ cluster (**Figure 3.8** , transition from D2 to E2). Although the barrier for elimination is rather high at 158 kJ/mol, the energy of the elimination product O–VCo_3^+ + CO lies at –51 kJ/mol well below that of the reactants, consistent with the observed mass-spectrometric and spectroscopic signatures.

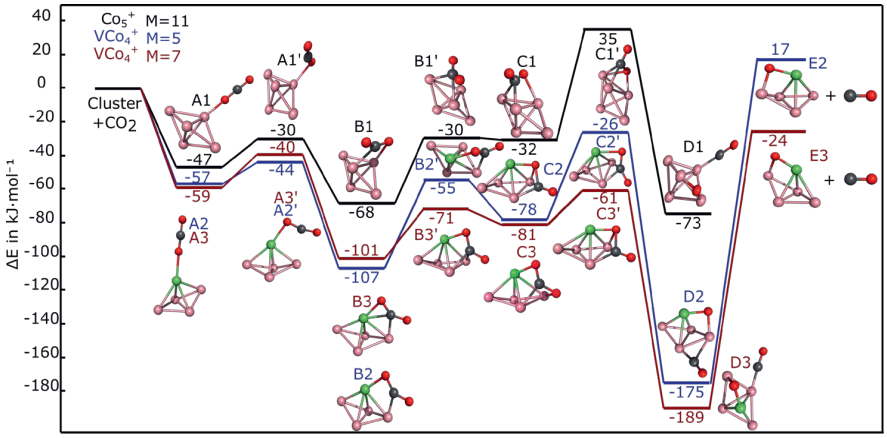

***Figure 3.9**: Reaction pathways for the adsorption, activation, and dissociation of CO_2 on Co_5^+ and VCo_4^+ clusters. Relative energies are given with respect to the most stable cluster (our global minimum for the respective size) + free CO_2 molecule. The letters label minima, the numbers (1-3) label $VCo_4(CO_2)^+$ with spin multiplicities 5 (blue) and 7 (red), and Co_5^+ (black)with spin multiplicity 11, respectively. Letters with numbers and primes label transition states. V, Co, C, and O are depicted by green, pink, black, and red spheres, respectively. DFT-calculated at the def2-TZVP/TPSSh level.*

Following the cases of $VCo_3^+ \cdot CO_2$ and $Co_4^+ \cdot CO_2$, we also examined the reaction pathways for CO_2 dissociation on trigonal bipyramidal clusters of VCo_4^+ (M=5 and 7) and Co_5^+ (M=11). As illustrated in **Figure 3.9**, the $VCo_4^+ \cdot CO_2$ reaction pathways, represented by blue (M=5) and red lines (M=7), reveal closely related energetics and geometries. Similar to $VCo_3^+ \cdot CO_2$, the lowest energy entrance complex (A2/A3) shows linear CO_2 bound to the vanadium atom, with binding energies of 57 and 59 kJ/mol for M=5 and 7, respectively. To partially bend CO_2 on the cluster (B2/B3), the carbon atom moves toward the cobalt atom at the acute apex, with transition state energies of –44 kJ/mol (A2', M=5) and –40 kJ/mol (A3', M=7). The energy for activated (bent) CO_2 on VCo_4^+ is marginally higher than that on VCo_3^+, by 9 kJ/mol. Similar to $VCo_3^+ \cdot CO_2$, three structures are involved in the full activation and

dissociation of CO_2 on VCo_4^+. Two predicted reaction pathways for CO_2 dissociation on VCo_4^+ exist, with the lowest energy path corresponding to septet multiplicity (red line). To dissociate CO_2 (C3'), the barrier between B3 and B3' must first be surpassed, analogous to the $VCo_3^+ \cdot CO_2$ reaction pathway; however, the potential barrier in this instance is only 30 kJ/mol (47 kJ/mol for VCO_3^+). The reaction can readily surpass this barrier to reach C3' and dissociate. The rupture of the C=O bond occurs when the η1-bound oxygen atom forms an η^2 bond with a V-Co bridge site, allowing the C=O to migrate to a cobalt site (D3). The final products are exothermic by 189 kJ/mol (D3), with a CO_2 dissociation barrier (C3') at –61 kJ/mol.

Because we did not observe $VCo_4^+ \cdot CO_2$ in the mass spectrum, the reaction pathway was expanded to explore CO desorption. CO desorbs at an overall energy of 24 kJ/mol below that of the reactants (E3). For $Co_5^+ \cdot CO_2$, the lowest energy structure predicted is the partially activated B1 (–68 kJ/mol), which has not been observed experimentally. This may be due to CO_2 already getting trapped in the potential well of structure A1.

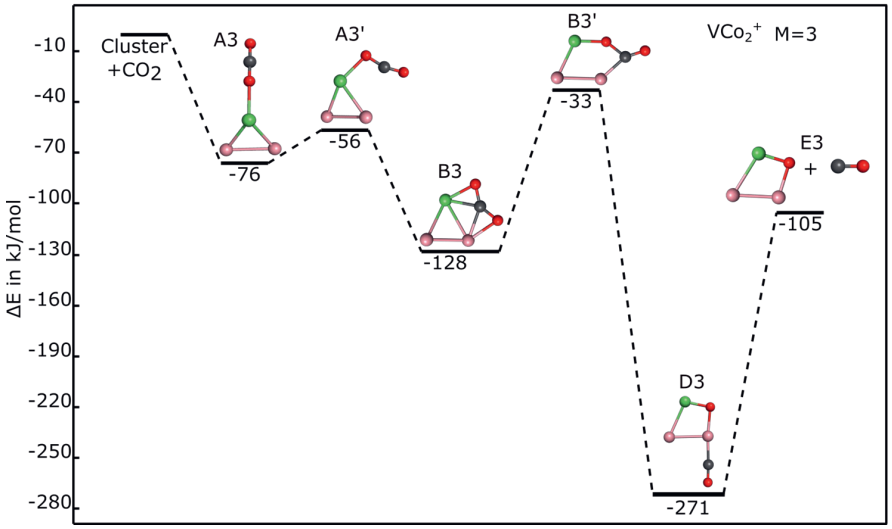

***Figure 3.10**: Reaction pathways for the adsorption, activation, and dissociation of CO_2 on the VCo_2^+ cluster on the triplet spin surface calculated at the def2-TZVP/TPSSh level. Minimum structures are labelled with capitals, transition state structures with primed capitals.*

To know why the $VCo_2^+ \cdot CO_2$ spectrum does not show any traces of CO_2 dissociation, we examined the reaction pathway for CO_2 dissociation on a triangular VCo_2^+ cluster with M=3 in **Figure 3.10**. Similar to VCo_4^+, the lowest energy entrance complex (A3) shows linear CO_2 bound to the vanadium atom, with a binding energy of 76 kJ/mol.

To partially bend CO_2 on the cluster (B3), the carbon atom moves towards the cobalt atom at the acute apex, with a transition energy of -56 kJ/mol (A3'). The carbon atom is bound to vanadium and the cobalt atom, whereas the free oxygen is bound to the cobalt atom in B3. The energy for activated (bent) CO_2 (20 kJ/mol) on VCo_2^+ is similar to VCo_3^+ (12 kJ/mol) and VCo_4^+ (19 kJ/mol). To dissociate CO_2 from the cluster, a rupture of the C=O bond occurs when the η1-bound oxygen atom forms an η^2 bond with a V-Co bridge site, allowing the C=O to migrate to a cobalt site (D3). The final product is exothermic by 271 kJ/mol (D3), with a CO_2 dissociation barrier (B3') at –33 kJ/mol. The reaction pathway was further expanded to explore CO desorption, with a structure (E3) at -105 kJ/mol.

A marked difference for VCo_2^+ is that the rate limiting barrier towards dissociation (from bent/activated CO_2) is much larger for VCo_2^+ (95 kJ/mol, linking well B3 and transition state B3') than for VCo_3^+ (47 kJ/mol, B2→B2') and VCo_4^+ (30 kJ/mol, B3→B3'), which suggests that it is likely that collisions with helium in flow-tube stabilize the adsorption product, preventing dissociation. This barrier height is consistently low for VCo_3^+ and VCo_4^+ when using other computational methods (Figure S2 of the Appendix). We further calculated the binding energies for physisorbed, chemisorbed and dissociated CO_2 on a number of VCo_n^+ clusters as well as on the V^+ ion. We always find the dissociated product lowest in energy, but never more than for the V^+ ion (see Figure S1 of the Appendix).

3.4. Conclusions

We synthesized cationic cobalt and vanadium-doped cobalt clusters, which were then reacted with various CO_2 isotopologues. Adsorption on pure cobalt clusters leads to intact physisorption, as diagnosed by infrared spectroscopy, with the exception of Co_4^+, which displays a mix of physisorbed and activated CO_2. Mass-spectrometric evaluation of the adsorption reaction demonstrates that CO_2 adsorption is highly size-selective, with evidence for CO_2 dissociation and subsequent CO elimination for VCo_3^+ and VCo_4^+. For the remaining clusters VCo_n^+ (n=1, 2, 5–6) the product mass of $[VCo_n, C, 2O]^+$ is spectroscopically identified as that of $O–VCo_n^+–CO$ through the appearance of the carbonyl CO stretch vibration, except for VCo_2^+, where only physisorption is evidenced. Reaction pathway calculations for the CO_2 adsorption and subsequent dissociation reactions over Co_4^+, VCo_3^+, Co_5^+, VCo_4^+ and VCo_2^+ validate the observed experimental results, demonstrating how the inclusion of V significantly alters the reaction energetics of CO_2 – cluster interactions.

This finding opens an extra route for CO_2 activation studies, where thus far only the scenario of electron donation by anionic clusters has been considered as a viable method. Now, we have shown that mixed-metal clusters, even when positively charged are capable of activating CO_2, as long as oxophilic elements are made part of the cluster.

A.3. Appendix to Chapter 3

A.3.1 Bare clusters

Cluster	the relative energies (kJ/mol) and spin multiplicities (M)		
VCo_3^+	 0 (M=4) 5 (M=2)	 3 (M=4)	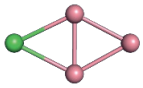 53 (M=4)
Co_4^+	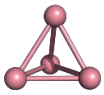 0 (M=8)		
VCo_4^+	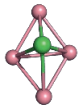 0 (M=7) 6 (M=5)	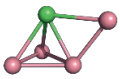 48 (M=5)	
Co_5^+	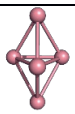 0 (M=11)	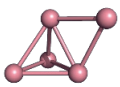 34 (M=11)	

***Table S1**: Gas-phase bare clusters: relative energies and spin multiplicities for all isomers with relative energies up to 53 kJ/mol above the global minimum for each size.*

A.3.2 Adsorption energies for different CO_2 adducts on Co_n^+ and VCo_{n-1}^+ clusters

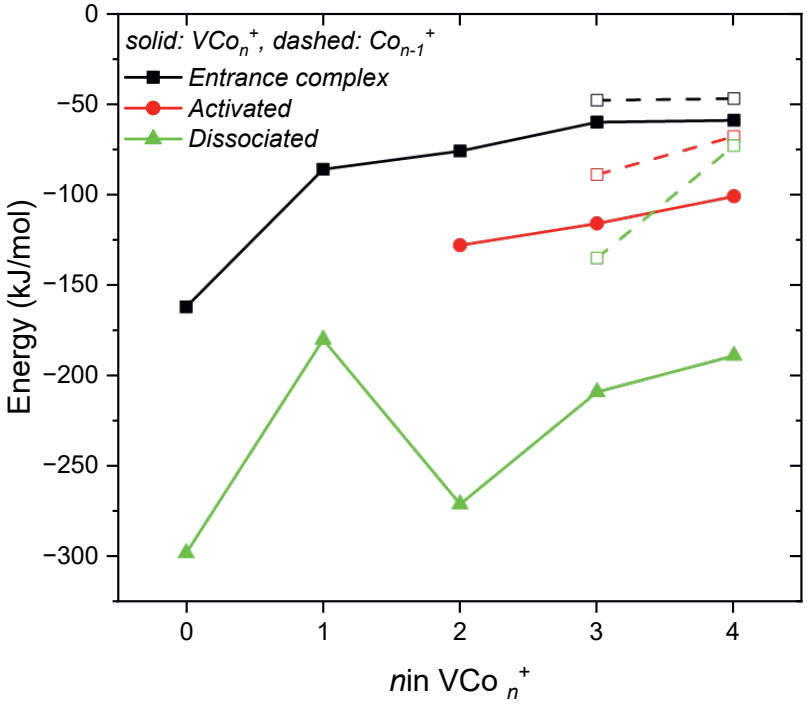

Figure S1: *The adsorption energies (AE) of CO_2 adducts on the VCo_n^+ clusters for n=0-4.*

A.3.3 Method benchmarks

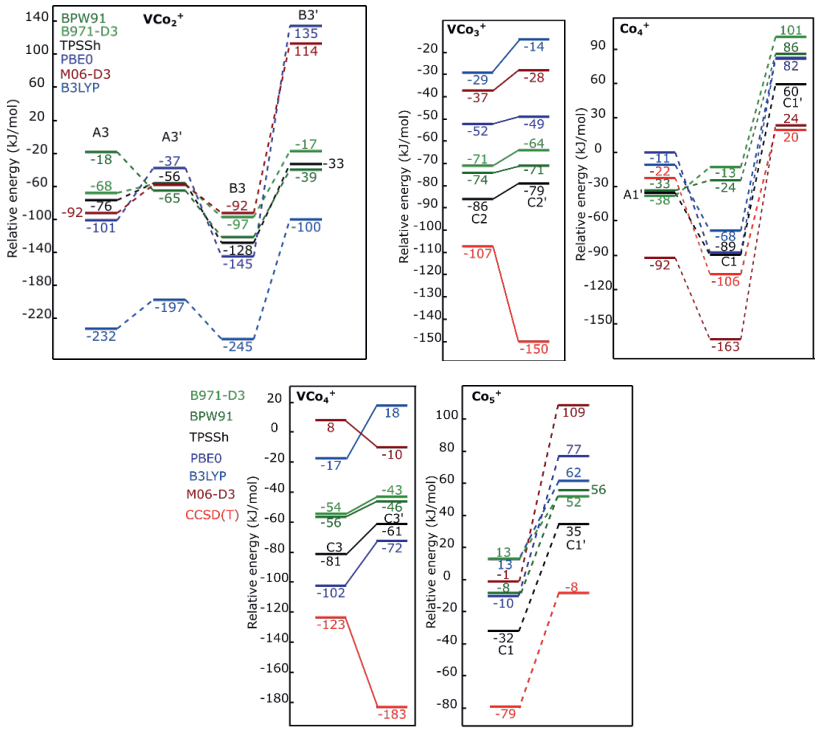

***Figure S2**: TPSSh calculated energies for products of the CO_2 dissociation pathway on VCo_2^+, VCo_3^+, Co_4^+, VCo_4^+ and Co_5^+ clusters. Energies are reported relative to the most stable cluster (our computed global minimum for the respective cluster size) plus a free CO_2 molecule. DFT and CCSD(T) calculations were performed with the def2-TZVP basis set. The various computational methods are color-coded. Stationary points along the reaction paths are labelled with capital letters for minima and primed capitals for transition states, shown on each TPSSh energy profile.*

To assess the reliability of the TPSSh functional for modelling CO_2 dissociation, we benchmarked both the intermediates preceding the dissociation barrier and the main CO_2 dissociation transition state (shown in Figures 3.8, 3.9 and 3.10) against a range of DFT functionals and the CCSD(T) method. As illustrated in Figure S2, this benchmark involved a detailed comparison of key reaction points on the reaction pathways of VCo_2^+, VCo_3^+, Co_4^+, VCo_4^+, and Co_5^+. While a few functionals, and occasionally CCSD(T), displayed outlier behaviour, the majority of tested methods predicted relatively low dissociation barriers for V-doped systems. These results support the use of TPSSh/def2-TZVP as a reliable choice for describing the reaction pathway and suggest that VCo_3^+ and VCo_4^+ clusters provide thermodynamically and kinetically favourable pathways for CO_2 dissociation.

A.3.4 Cartesian coordinates (in Å)

Cartesian coordinates and SCF energies (E_h) of cationic bare clusters from Table S1.

VCo_3^+	Isomers	
V 8.12673 7.43199 8.32549 Co 7.68768 9.79146 8.54791 Co 9.74940 8.68592 9.71039 Co 9.72029 9.11543 7.51671 Eh= -5092.149532 (M=4) Eh= -5092.147614 (M=2)	V 7.14372 10.30248 9.95931 Co 8.23429 10.77821 7.77817 Co 9.38964 9.48102 9.39471 Co 7.87324 7.97319 10.42332 Eh= -5092.148352 (M=4)	V 7.47461 7.63753 6.94395 Co 7.90466 9.05850 9.04413 Co 10.02913 9.78844 9.91332 Co 9.75050 8.43453 7.89980 Eh= -5092.129212 (M=4)
Co_4^+		
Co 0.85943 -1.12200 0.05678 Co -0.86627 -0.06173 -1.11631 Co -0.85155 0.06158 1.12596 Co 0.85839 1.12216 -0.06643 Eh= -5530.954951 (M=8)		
VCo_4^+		
V 9.01802 9.19272 9.32190 Co 9.81691 10.84975 7.58391 Co 7.74410 9.66239 7.26981 Co 8.09450 7.41242 7.77841 Co 10.13536 8.56602 7.22107 Eh= -6474.9936 (M=7) Eh= -6474.9913 (M=5)	V 7.82482 8.66136 9.20975 Co 10.13514 8.35070 9.41504 Co 8.81270 7.03262 10.86271 Co 9.35095 8.56870 7.19215 Co 8.91458 9.29462 11.37045 Eh= -6474.97548148 (M=5)	
Co_5^+		
Co 0.00088 -0.71887 -1.14499 Co -0.00118 -0.72098 1.14460 Co -2.00220 0.06938 -0.00218 Co 1.97180 0.04842 0.00134 Co 0.03069 1.32204 0.00123 Eh= -6913.79722938 (M=11)	Co 0.31322 0.91317 0.68978 Co 0.31362 -0.91157 -0.69002 Co 2.39292 -0.00030 -0.00025 Co -1.51084 0.71847 -0.87506 Co -1.50892 -0.71977 0.87555 Eh= -6913.784231 (M=11)	

Cartesian coordinates and SCF energies of adducts along the reaction paths shown in Figures 3.8 and 3.9.

VCo_3^+ (M=4)	CO_2 adducts	
V 0.7147750 -0.4065560 -0.1412330 Co -1.3396770 -0.4890690 1.2443070 Co -0.9435420 1.4226240 -0.0365670 Co -1.6133940 -0.5624650 -1.0723690 O 2.8865100 -0.2188920 -0.0913100 C 4.0449890 -0.0273700 -0.0172120 O 5.1758390 0.1558390 0.0533870 Eh= -5280.840456	V 0.4789950 -1.0734780 0.0000040 Co -1.5434180 -0.0989090 -1.1064880 Co -1.5434140 -0.0988940 1.1064880 Co 0.2010630 1.2568840 -0.0000040 O 2.5606460 -1.2509090 0.0000140 C 2.9365470 -0.1061380 -0.0000010 O 3.5993040 0.8423640 -0.0000140 Eh= -5280.835947	Co -0.451743 -1.160130 -0.394431 O -2.519964 -1.003497 -0.502487 C -2.054402 0.066386 -0.076915 O -2.473052 1.191051 0.319325 Co 1.325155 0.398570 -0.996554 Co 1.222222 -0.535735 1.132851 V -0.479231 1.229758 0.404864 Eh= -5280.862047
V -0.191464 1.346757 -0.686996 Co 0.185432 -0.049281 1.404501 Co -0.211980 -1.112675 -0.707061 Co 1.877533 -0.106600 -0.229397 O -2.830877 -0.682685 0.121867 C -1.755027 -0.152147 0.109338 O -1.411497 1.015353 0.799104 Eh= -5280.844060	V 0.022928 -1.209400 0.965877 Co -0.036490 -0.205749 -1.369616 Co -0.218604 1.204507 0.560661 Co 1.862362 0.261631 -0.061307 O -2.879826 0.462765 0.247183 C -1.769695 0.013064 0.180294 O -1.424889 -1.238129 -0.341710 Eh= -5280.850563	V -0.424978 -1.563047 -0.671655 Co -0.331526 0.939979 -0.997841 Co 0.248772 0.130392 1.119488 Co 1.695526 -0.352158 -0.758631 O -2.618829 0.505026 1.303615 C -1.640654 0.230200 0.702547 O -1.809311 -0.328062 -0.768944 Eh= -5280.847862

V 0.265352 -1.374883 0.929857 Co -0.056597 -0.462925 -1.385739 Co -0.389010 1.030211 0.483639 Co 1.818455 0.336444 0.029998 O -3.321947 0.961385 0.275641 C -2.188485 1.049503 0.370588 O -0.406983 -2.041048 -0.462603 Eh= -5280.897426		V 0.245373 -1.376566 0.908059 Co -0.096130 -0.438255 -1.311886 Co -0.365289 1.094946 0.454164 Co 1.803838 0.314510 0.035263 O -0.356576 -2.106835 -0.490449 Eh= -5167.480592

Co_4^+ (M=8)

Co -0.603392 0.390219 -0.155370 Co 1.104620 -0.615161 -1.248495 Co 1.616805 1.086814 0.261495 Co 0.935839 -0.908753 1.040441 O -2.652586 0.251104 0.055142 C -3.810469 0.054422 0.041611 O -4.944739 -0.132959 0.031005 Eh= -5719.640978	Co -0.856095 0.515752 0.750835 Co -0.266043 -0.779410 -1.013540 Co 1.183905 0.940491 -0.339665 Co 1.021956 -0.886231 0.947124 O -2.877101 0.757761 0.840065 C -3.060303 0.089685 -0.131595 O -3.445043 -0.517304 -1.041942 Eh= -5719.635886	Co -0.499804 -1.080086 0.111078 Co -0.314078 1.255118 -0.159731 Co 1.281092 0.147160 1.141578 Co 1.250110 -0.293107 -1.175641 O -2.512183 -1.116514 0.234506 C -2.061626 0.010583 0.054540 O -2.325967 1.201169 -0.110557 Eh= -5719.656604
Co -0.214345 -1.553791 -0.478334 Co -0.493015 0.720230 -0.346080 Co 1.096260 -0.234227 1.143660 Co 1.718684 -0.233644 -1.118254 O -3.106573 0.732372 1.029113 C -2.123151 0.655485 0.440102 O -1.758861 -0.524096 -0.741629 Eh= -5719.599967		Co 0.958233 -0.778692 -0.289309 Co 0.272973 1.314047 0.446975 Co -1.139567 0.289084 -1.108021 Co -1.119897 -0.594348 1.165893 C 2.605132 -0.123783 -0.152923 O 3.653206 0.320059 -0.058844 O -0.749545 -1.397372 -0.455530 Eh= -5719.674175

VCo_4^+ (M=7)

V 0.731919 -0.543543 0.007098 Co -1.502713 -1.709426 -0.002974 Co -1.273434 0.348830 1.195921 Co 0.125111 1.851502 -0.029149 Co -1.246662 0.318638 -1.247070 O 2.903713 -0.546046 0.030997 C 4.079097 -0.488494 0.043224 O 5.225228 -0.437270 0.055207 Eh= -6663.684388	V -1.225538 -1.312012 0.016293 Co 0.481101 -0.007114 1.282812 Co 0.575183 -0.048917 -1.159044 Co -1.162878 1.152684 -0.023495 Co 1.205886 -1.967633 0.121177 O -4.006766 0.948193 -0.129820 C -3.532612 -0.112484 -0.093346 O -3.345246 -1.296586 -0.065818 Eh= -6663.677146	V 0.188860 1.167579 0.039355 Co 1.480685 -0.992798 -0.041916 Co -0.747020 -0.789082 1.199252 Co -2.260127 0.747068 -0.103991 Co -0.655310 -0.843834 -1.091475 O 3.240923 0.194096 -0.017396 C 2.224281 0.891833 -0.009223 O 1.911379 2.120674 0.039858 Eh= -6663.700319
V 0.109549 1.345707 0.712981 Co 1.395826 -0.994613 0.928117 Co -0.961264 -0.911467 1.091648 Co -1.940064 0.671260 -0.510229 Co 0.189948 -0.401072 -0.961624 O 2.830239 0.074079 -0.820846 C 1.875221 0.738190 -0.422757 O 1.809515 1.946651 0.055921 Eh= -6663.688740	V -0.124105 -0.928716 -1.099508 Co 1.490976 1.222330 -0.226376 Co -0.967798 1.374957 -0.354443 Co -2.118707 -0.685214 0.314444 Co 0.071493 -0.115658 1.156164 O 2.612805 -0.313887 0.600211 C 1.638413 -0.924674 0.069272 O 1.627112 -1.791923 -0.877389 Eh= -6663.692551	Co 0.042679 -0.071413 -0.073845 C 0.056266 0.168189 1.894974 O 0.891911 0.039246 2.705501 O -1.465126 0.609334 2.437419 V -1.723250 1.278634 0.775685 Co -1.846158 -1.044279 1.314903 Co -0.786607 1.615425 -1.607719 Co -2.180166 -0.360683 -1.014303 Eh= -6663.685072
Co -0.043915 -0.885923 -0.692622 C -1.738149 -1.481109 -0.967534 O -2.770098 -1.941054 -1.156351 O -1.495519 0.438237 1.926460 V 0.120185 0.139524 1.626716 Co -1.594917 0.759561 0.024633 Co 2.237351 -0.709903 0.168710 Co 0.885725 1.286587 -0.426492 Eh= -6663.734000		Co 0.005935 -0.844107 -0.711964 O -1.473451 0.345683 1.912785 V 0.178683 0.178916 1.609630 Co -1.581416 0.819898 0.060105 Co 2.154164 -0.736754 0.268836 Co 0.824996 1.264447 -0.511987 Eh= -6550.314298

Co_5^+ (M=11)

Co -0.690294 -0.086982 -0.387786 Co 1.562271 0.190458 -1.004481 Co 0.815803 -1.925775 0.073537 Co 0.317389 2.066623 0.062408 Co 0.945492 0.119951 1.274707 O -2.740693 -0.348076 -0.437318 C -3.841123 -0.333003 -0.024945 O -4.921997 -0.322245 0.365014	Co -0.011097 0.008556 -0.001910 O 0.002158 -0.000536 2.028188 C 1.199287 -0.004285 1.965993 O 2.339945 -0.011643 2.192469 Co 2.138804 -0.103261 -0.898393 Co 0.341280 -0.138355 -2.353663 Co 0.878564 1.917544 -1.107621	Co 0.184387 -0.173791 -1.229735 Co 0.279417 -0.417065 1.096550 Co -1.895821 -0.694777 0.099909 Co 1.549944 1.369906 -0.016358 Co -0.866492 1.464735 0.171343 O 1.080806 -2.017859 -1.258188 C 1.021610 -1.785529 -0.053672

Eh= -7102.483188	Co 0.815799 -2.090687 -0.974666 Eh= -7102.476940	O 1.307136 -2.183262 1.071194 Eh= -7102.491271
Co -0.001278 -0.001734 0.001256 C 0.001412 0.001604 1.979402 O 1.191141 -0.000116 1.652067 O -0.756514 -0.330934 2.921579 Co -1.652359 1.089522 1.624700 Co -1.843809 -1.204161 0.842548 Co -2.214083 0.549974 -0.641304 Co -1.183052 -1.547437 -1.397134 Eh= -7102.476879	Co -0.030248 1.198099 0.470567 Co -1.024166 -0.913458 0.780800 Co 1.380304 -0.708926 1.099321 Co -1.866535 0.537606 -0.948291 Co 0.239230 -0.504186 -1.170734 O 2.129282 1.238257 0.328261 C 1.863882 0.349540 -0.543941 O 2.175538 0.034290 -1.694985 Eh= -7102.477510	Co -0.002440 0.000232 0.004486 C 0.014733 0.000331 1.936859 O 0.715238 0.013978 2.868568 O -1.561862 -0.647853 2.215390 Co -1.840736 -1.580183 0.638433 Co -1.885122 0.875502 1.137501 Co -2.078341 -0.134699 -1.202239 Co -0.561287 -1.991073 -1.343387 Eh= -7102.451942
Co 0.360853 -0.641642 -0.894675 C 1.863720 -1.673251 -0.880784 O 2.794146 -2.322692 -0.790046 O 1.287876 0.855419 1.842259 Co -0.222559 0.059963 1.321527 Co 1.497794 1.300578 0.170015 Co -1.167521 1.190645 -0.519551 Co -1.929948 -1.020191 0.002112 Eh= -7102.493094		

4 IR spectroscopy of cationic MCo_n^+–CO_2 (M=Fe, Mn, Cr; *n*= 2-7) cluster complexes

Abstract

We investigated the CO_2 adsorption reaction on pure cationic cobalt clusters and cobalt clusters doped with iron, manganese, or chromium atoms using a combination of experimental infrared (IR) spectroscopy and density functional theory (DFT) calculations. MCo_n^+ (M=Fe, Mn, Cr) clusters were produced by laser ablation and subsequently reacted with CO_2 to form $MCo_n^+ \cdot CO_2$ adducts. These were then characterised by IR multiple photon dissociation spectroscopy in the 300 – 2200 cm^{-1} spectral range utilising the IR free-electron laser, FELICE. The experimental IR spectra were compared with DFT-calculated spectra to identify geometrical structures. The spectra for CO_2 adsorbed on pure cobalt clusters are highly similar for all cluster sizes (except for Co_4^+) and indicative of CO_2 physisorption rather than activation. The spectrum for $Co_4^+ \cdot CO_2$ shows the presence of both physisorbed and activated CO_2. Substituting one Co atom by a Fe atom in the clusters does not affect their activity toward CO_2. In contrast, substitution by a Mn atom results in CO_2 activation in two cluster sizes ($MnCo_2^+$ and $MnCo_3^+$), whereas substitution by a Cr atom leads to a mixture of physisorbed and dissociated CO_2 on $CrCo_2^+$ and $CrCo_4^+$.

This chapter is adapted from:
D. Pradeep, M. Szalay, T. Höltzl, J. M. Bakker, *in preparation*.

Experimental work was carried out by DP; DFT calculations were conducted by MS and TH.

4.1. Introduction

The continuous emission of CO_2 into the atmosphere through the combustion of fossil fuels has contributed to global warming and ocean acidification. Restraining the atmospheric concentration of CO_2 is therefore an important societal challenge. Using CO_2 as a feedstock for renewable fuels or other more valuable chemicals is a potential route to reduce CO_2 emissions. Instead of emitting CO_2 into the atmosphere, it can be captured and repurposed by reacting with renewable H_2 to produce various hydrocarbons, thereby creating a "circular carbon economy".[152]

Due to the very stable molecular structure of CO_2 with its high bond dissociation energy (approximately 750 kJ/mol),[7] it is difficult to break the C=O double bond under standard temperature and pressure conditions, requiring the need for a catalyst. In industry, methanol is produced from synthesis gas (syngas), a mixture of CO, CO_2, and H_2 over a $Cu/ZnO/Al_2O_3$ catalyst at temperatures of 200-300 °C and pressures of 50-100 bar.[13, 137] The reaction is highly energy-intensive, with a conversion efficiency of 35-45% per pass.[153] The reaction also competes with the reverse water-gas shift reaction, producing unwanted byproducts. For direct conversion, a catalyst is required that can activate or dissociate CO_2 at lower temperatures. The reaction mechanism and active sites of catalysts should be well understood to design more efficient and selective catalysts.

Gas-phase metal clusters form a good model system for investigating the reaction mechanism and active sites of more complex real-world catalysts.[57-59, 66, 136] Controlled studies of reactions under isolated conditions will help to understand the roles of the electronic and geometric structures of the catalyst materials, as well as the role of the elemental composition of the catalyst. Such studies will provide a mechanistic understanding of activation and guide the design of future catalyst materials. They will further produce stringent benchmarks for theoretical methods used for modelling catalytic reactions under more realistic, and therefore more complex conditions.

The existing catalysts are often more reactive at defects or low-coordinated atoms, where charge distribution is also inhomogeneous. Therefore, a significant number of studies have been devoted to exploring the size and charge dependence of metal clusters and ions towards CO_2 activation. IR spectroscopic studies of various cationic $M^+(CO_2)_n$ complexes (M= Co, Rh, Ir, Fe, Ni, V, Ti, Mg, Al, Si) show little to no activation of CO_2.[81, 154-160] In contrast, CO_2 activation is observed on anionic metal centres, such

as Au, Cu, Ni, Co and Fe.[161-166] This difference arises from the ability of a metal anion to donate electron density to the anti-bonding orbital of CO_2, thereby forming a bent structure.[73, 167] Similar observations for clusters of late transition metal elements. Our prior work on CO_2 adsorption on cationic copper clusters shows no activation due to a large energy barrier between physisorbed (linear) and activated (bent) CO_2 structures.[74] In contrast, CO_2 activation has been observed by Co_n^- and Pt_n^- clusters.[75, 76] Recent work on CO_2 adsorption in cationic and anionic copper oxide clusters has demonstrated similar activation in anionic clusters and physisorption in cationic clusters,[77] whereas adsorption on MgO clusters led to the formation of carbonate-like structures (CO_3).[168]

Catalyst materials are typically more complex than simple clusters of a single element. This is exemplified by the industrial $Cu/ZnO/Al_2O_3$ catalyst, where Cu-Zn or Cu-ZnO sites can play a significant role in enhancing the efficiency of CO_2 hydrogenation.[13, 83, 169-172] However, to our knowledge, there are no existing experimental studies exploring how doping metal clusters influences their activity with CO_2. Anionic carbon-doped copper clusters and copper oxide clusters induce activation and/or dissociation of the adsorbed CO_2 molecules, but the explicit dopant effect via a comparison with pure copper anions could not be made. [77, 79]

Introducing a foreign element to single-element metal clusters could significantly alter their activity towards CO_2. Including an oxophilic dopant atom can enhance CO_2 activation by attracting the oxygen atom(s), thereby destabilizing carbon dioxide. This effect was predicted in a theoretical study on the effects of doping by 3d metal elements on the activation of CO_2 by neutral copper clusters.[103] Notably, the early transition metals, such as scandium, titanium, and vanadium, exhibit a significant reduction in the barrier for CO_2 dissociation, which correlates with their higher M-O binding energies compared to those of the late transition metals.[108] In our recent experimental study of CO_2 activation on cationic vanadium-doped cobalt clusters, we observed size-selective dissociation of CO_2, which in some cases led to the elimination of CO and cluster oxidation.[173]

In this work, we extend our investigation of CO_2 adsorption onto doped cobalt clusters by addressing other first-row transition elements (Fe, Mn, and Cr) using infrared multiple-photon dissociation (IRMPD) spectroscopy. We selected cobalt clusters as the primary focus of the study due to their importance as a catalyst, for example in the formation of hydrocarbons from CO and H_2 in the Fischer-Tropsch reaction[107] or in the selective hydrogenation of CO_2 with cobalt-based catalysts ($CoAlO_x$).[174] Additionally, we compute theoretical IR spectra for selected products to

benchmark the experimental IR spectrum and the potential energy surface to rationalize the pathways of formation of the observed product structures.

4.2. Methods

4.2.1 Experimental

Experiments were carried out in the molecular beam instrument within the cavity of the free-electron laser FELICE[123, 124] housed at HFML-FELIX. Iron, manganese, and chromium-doped cobalt clusters are formed using a home-built dual-target dual-laser ablation source based on an existing design.[87, 88] As discussed in Chapter 2, the source consists of a rectangular target holder where two metal targets (in this case, dopant and cobalt) of dimensions 24 x 7 mm each are placed and ablated by two loosely focused Nd: YAG lasers operating at the second harmonic (532 nm, pulse energy 7-8 mJ). The doping of cobalt clusters with foreign element is precisely controlled by adjusting the intensities and relative timing of the two lasers. The target holder is mounted on a two-dimensional translation stage, which continuously moves the target in a snake-like pattern at a speed of 0.1 mm/s. The metal vapours produced during ablation are collisionally cooled down by helium carrier gas injected into the ablation region using a pulsed supersonic valve (Jordan TOF Products, Inc.) with a stagnation pressure of 8 bar. The helium pulse entrains the metal clusters formed into a reaction channel, where CO_2 is injected by a second pulsed valve (General Valve, Series 9) with a backing pressure of 1 bar. The clusters react with CO_2 to form cluster-CO_2 complexes, and the gas mixture then supersonically expands into the vacuum to form a molecular beam. The formed beam is then collimated by a 2 mm diameter skimmer and further shaped by passing through a 2 mm horizontal slit aperture to ensure a good overlap with the FELICE laser. Both shaping elements are electrically grounded. The beam then proceeds to the interaction region, where it is illuminated by the IR light from FELICE at a 35-degree angle.[123] Since the cavity is fixed, the entire molecular beam instrument can move horizontally and vertically to ensure a good spatial overlap between the molecular and laser beams, as well as to position the cluster complexes away from or towards the fixed focus of the laser beam, thereby controlling the laser fluence experienced by the cluster complexes. The IRMPD spectra shown here were measured with the molecular beam approximately 250 mm from the laser focus in the horizontal direction. This reduces the laser fluence by a factor of 9 from the focus but increases overlap with the molecular beam. After illumination, the complexes are extracted into a time-of-flight mass spectrometer (Jordan TOF Products, Inc.) by

pulsing high voltages to the extraction plates and detected by a micro-channel plate-based detector. The complexes that did not interact with the IR light are prevented to enter the mass spectrometer by a slit aperture positioned right above the extraction plates.

FELICE is tunable in the 4.5-100 μm (100–2200 cm^{-1}) spectral range, but only the 300-2200 cm^{-1} region is used in this work, as CO_2 vibrations lie in this range. It has a distinct pulse structure, with a macro pulse (10 μs pulse width, 5 Hz repetition rate) containing a train of micro pulses (0.2-10 ps pulse width, 1 GHz repetition rate). It has high pulse energies, typically between 0.9 and 1.3 J, based on the different frequencies and spectral bandwidths between 0.5 and 3% full width at half maximum (FWHM) of the central frequency. Pulse energies and spectral properties are measured outside the FELICE cavity by outcoupling a small fraction of the laser beam.

When the IR light is in resonance with the vibrational mode of the cluster-molecule complexes, the complexes dissociate after absorbing multiple photons into their vibrational states, resulting in a decrease in their intensity. This depletion is detected by running the experiment at 10 Hz and the FELICE laser at a 5 Hz repetition rate. Consequently, we registered two mass spectra at each laser frequency: one with and one without FELICE.

In the mass spectrum, clusters are observed not only with one, but also with multiple CO_2 molecules to form $MCo_n^+ \cdot (CO_2)_m$ complexes, with *m* varying with cluster size *n*. Complexes with more than one CO_2 can fragment at the same resonant frequency as those with only a single CO_2. Their dissociation into the $MCo_n^+ \cdot CO_2$ channel can partially or fully screen the absorption spectrum of $MCo_n^+ \cdot CO_2$. This is clearly indicated elsewhere.[175] To eliminate these contributions, the branching ratio B_n (see details in Chapter 2) of CO_2 adducted clusters is calculated as the ratio of the mass-spectrometric intensities of all cluster-$(CO_2)_m$ complexes to those of all clusters plus cluster$(CO_2)_m$ complexes.

4.2.2 Computational

Density functional theory calculations were performed for the $CrCo_2^+/Co_3^+ + CO_2$ system, using the Q-Chem 6.1 software package.[176] All geometry optimisations and frequency calculations were performed using the TPSSh/def2-TZVP[134, 145] + D3[177] level of theory. The lowest-energy bare cluster structures were determined by testing various initial geometries with different spin multiplicities: even multiplicities

(2 – 14) for $CrCo_2^+$, and odd multiplicities for Co_3^+. In all cases, triangular geometries were identified as the most stable structures. For Co_3^+, both the lowest-energy spin multiplicity and geometry agree with previous computational studies.[178] For the cluster–substrate intermediates, initial geometries corresponding to the quasi-degenerate spin multiplicities (within ~10 kJ/mol of each other; Co_3^+: 7 and 3; $CrCo_2^+$: 2, 6, and 10, listed in order of increasing energy) were generated using the Budapest in-house structure-construction code, which systematically enumerates all plausible bonding motifs. This procedure has been successfully applied in several combined experimental and theoretical studies of metal-cluster activation processes.[103, 179-182] Subsequent optimisations revealed a pronounced multireference character for the $CrCo_2^+ + CO_2$ system, arising from strong state-coupling effects. Consequently, the reaction energetics exhibited a high sensitivity to structural variations, with even minor distortions shifting relative energies by as much as 80 kJ/mol. This sensitivity was markedly reduced for the dectet spin multiplicity (M=10), which produced the lowest-energy $CrCo_2^+ \cdot CO_2$ adduct and thus the largest thermodynamic driving force among the three multiplicities examined. Accordingly, M = 10 for $CrCo_2^+$ and M = 7 for Co_3^+ were selected for detailed mechanistic analysis, including transition-state characterization. Harmonic vibrational analyses were performed for all product structures to confirm their nature as minima or transition states and to enable comparison with the experimental IR spectra. The unscaled harmonic stick spectra were convoluted using a Gaussian line-shape function with a full width at half maximum of 10 cm^{-1}. Self-consistent field (SCF) stability was verified in all cases. Intrinsic reaction coordinate calculations were carried out from each transition structure. Binding energies (BE) of the CO_2 adduct are calculated as the energy difference between the cluster─CO_2 product and the summed energies of the individual reactants, BE = E(cluster─CO_2) - E(cluster) - E(CO_2).

4.3. Results and discussion

4.3.1 $FeCo_n^+$

Figure 4.1 shows typical mass spectra of cationic iron-doped cobalt clusters (panel a) and the same distribution reacted with CO_2 (panel b). An enlarged view of each mass spectrum in the m/z=290-420 range is displayed in the insets. Without CO_2 (**Figure 4.1a**), the most prominent peaks are those corresponding to pure cobalt clusters, while the less intense peaks 3 and 6 mass units lower correspond to cobalt clusters doped with one or two Fe-56 atoms, respectively. Apart from Fe-56, one can discern smaller peaks corresponding to minor isotopes Fe-54 and Fe-57 in the mass

spectrum. In the inset in **Figure 4.1b**, the key masses for which IR spectra will be presented—$FeCo_4^+ \cdot CO_2$, $Co_5^+ \cdot CO_2$, $FeCo_5^+ \cdot CO_2$, $Co_6^+ \cdot CO_2$—are highlighted in bold. The mass spectrum is somewhat complex, with many CO_2 molecules adsorbed to the Co^+ ion and the $FeCo^+$ cluster. Furthermore, Co_n^+ clusters ranging in size n=2–5 can bind up to three CO_2 molecules. The contamination from oxides is minimal and primarily leads to the formation of $FeCoO^+$, again with numerous CO_2 molecules bound to this oxide. This contamination is attributed to oxides present in the gas line or on one or both of the target surfaces.

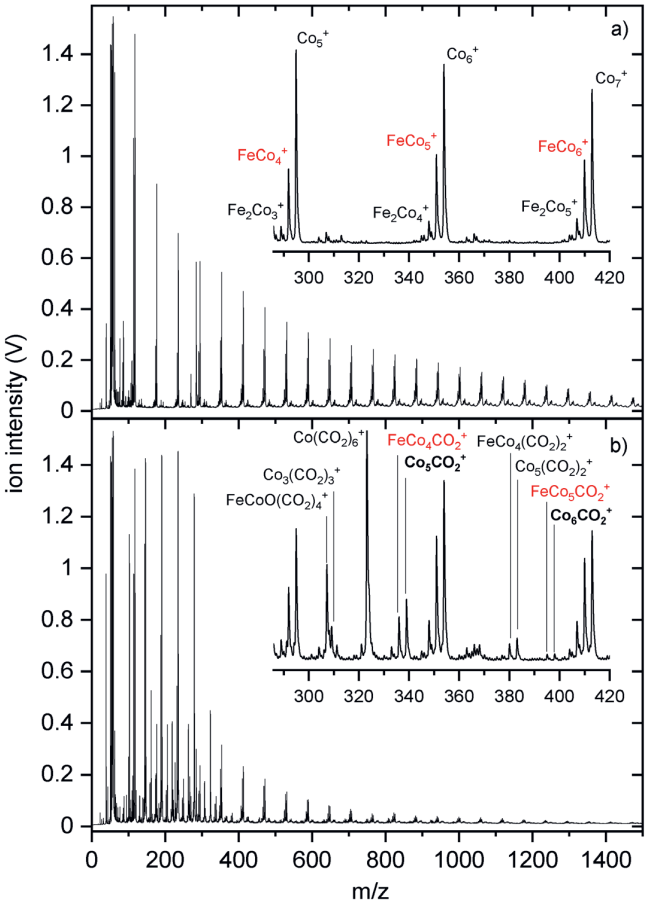

***Figure 4.1**: Mass spectra of the distribution of cationic iron-doped cobalt clusters without (panel a) and with (panel b) CO_2 injected. The insets show enlargements of the mass spectra near the Co_5^+, Co_6^+, and Co_7^+ clusters.*

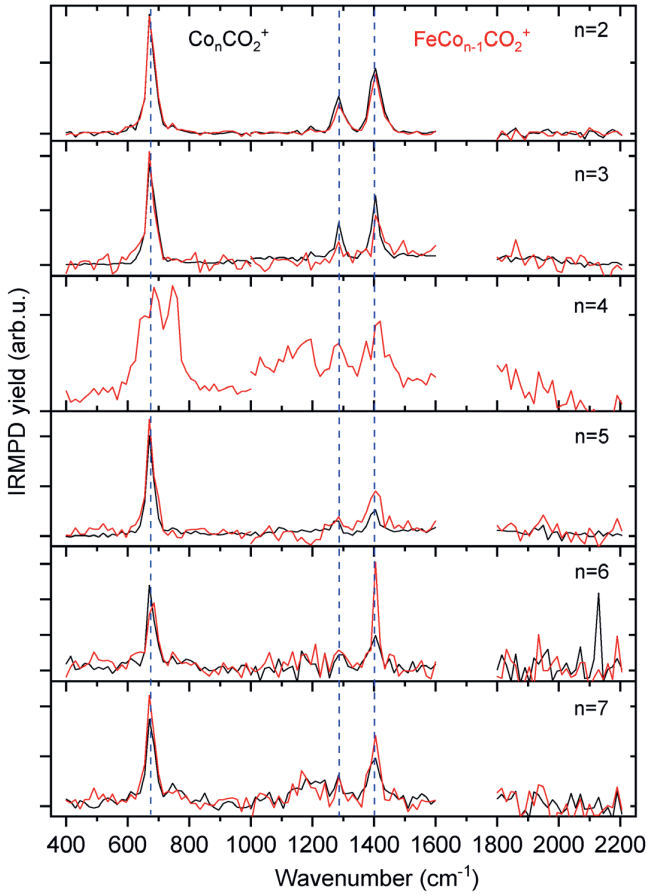

***Figure 4.2**: IRMPD spectra of $Co_n^+ \cdot CO_2$ (black line) and $FeCo_{n-1}^+ \cdot CO_2$ (red line) for n=2–7. Blue dashed lines indicate the line positions of free CO_2 vibrational modes.*

Figure 4.2 illustrates the experimental IR spectra of $Co_n^+ \cdot CO_2$ (black traces) and $FeCo_{n-1}^+ \cdot CO_2$ (red traces) for n = 2–7. The spectrum is recorded in the 400–2200 cm^{-1} range with an omission between 1600 and 1800 cm^{-1}. As reported in our previous work,[173] the spectra for $Co_n^+ \cdot CO_2$ are similar for all n, with four bands around 650, 1200, 1300, and 1400 cm^{-1}, respectively. The spectrum for $Co_4^+ \cdot CO_2$ (m/z=280) is not shown here because its mass peak is contaminated by the strong, nearby peak of $Co^+ \cdot (CO_2)_5$ at m/z=279 (such overlaps do not play a role for M=Mn, Cr, *vide infra*).

Free CO_2 has three fundamental vibrational modes: the symmetric stretch (ν_1), the bend (ν_2), and the anti-symmetric stretch (ν_3). ν_2 and ν_3 are IR-active and have been experimentally observed at 667 cm^{-1} and 2349 cm^{-1}.[147] The symmetric stretch vibration is symmetry-forbidden in free CO_2, but it is Raman active and has been

observed as part of the Fermi resonance with the overtone of the bending vibration at 1285 and 1388 cm^{-1}. The bands in the experimental spectra for Co_n^+ clusters, located around 650, 1300, and 1400 cm^{-1}, are thus close to the frequencies observed for free CO_2, with the Fermi dyad having gained IR intensity by symmetry-breaking due to the presence of the cluster. Finally, the band detected around 1200 cm^{-1} is nearly half the frequency of the asymmetric stretch vibration (v_3). It is likely caused by the small fraction (<1%) of second harmonic light present in the FEL cavity. As we concluded in our previous work,[173] these bands indicate that CO_2 is physisorbed to cobalt clusters.

The IR spectra for CO_2 adsorbed on iron-doped cobalt clusters (**Fig. 4.2**, red trace) closely resemble those of pure cobalt clusters, except for $FeCo_3^+ \cdot CO_2$ (n = 4), which exhibits an additional band at 745 cm^{-1} and a strong peak at 1195 cm^{-1}, along with physisorbed CO_2 bands at 684, 1285 and 1420 cm^{-1}. The bands at 745 and 1195 cm^{-1} are relatively close to those observed for activated CO_2 on Pt and Cu_xO_y anionic clusters,[75, 77] around 800, 1100, and 1600 cm^{-1}. The spectra between 1600 and 1800 cm^{-1} are not measured, so the band corresponding to 1600 cm^{-1} for activated CO_2 cannot be confirmed. These bands were observed in our previous work, where the spectrum of $Co_4^+ \cdot CO_2$ exhibits three similar bands; because these were recorded using isotopically labelled $^{13}CO_2$, the wavenumbers differ slightly from those observed here. The presence of five bands in the $FeCo_3^+ \cdot CO_2$ spectrum, like for $Co_4^+ \cdot {}^{13}CO_2$ suggest a mixture of physisorbed and activated CO_2.

4.3.2 $MnCo_n^+$

The typical mass distribution for cationic manganese-doped clusters, as well as the distribution when reacted with CO_2, is shown in **Figure 4.3**. Similar to the iron-doped cobalt clusters, the Co^+ and $MnCo^+$ ions bind a large number of CO_2 molecules, and Co_n^+ (n=2-5) clusters bind up to three CO_2 molecules. However, the contamination from oxides is very minimal in the mass spectrum of manganese-doped cobalt clusters.

The doped and bare clusters are measured simultaneously, so for each new dopant, the IR spectra for $Co_n^+ \cdot CO_2$ are again recorded alongside $MCo_{n-1}^+ \cdot CO_2$. The IR spectra for $Co_n^+ \cdot CO_2$ (black trace) and $MnCo_{n-1}^+ \cdot CO_2$ (red trace) are shown in **Figure 4.4** for n = 2–7 in the 300–2200 cm^{-1} range. The signal-to-noise ratio of the spectra for $MnCo_{n-1}^+ \cdot CO_2$ is lower than for the bare cobalt clusters due to the low production efficiency for $MnCo_{n-1}^+$. The IR spectra in **Figure 4.4** for $Co_n^+ \cdot CO_2$ are consistent with those shown in **Figure 4.2**. Furthermore, the mass peak for $Co_4^+ \cdot CO_2$ is clearly

distinguished from the $Co^{+}\cdot(CO_2)_5$ peak, so the spectrum for $Co_4^{+}\cdot CO_2$ (n=4) is included. It shows a mixture of physisorbed and activated CO_2, similar to $FeCo_3^{+}\cdot CO_2$ as discussed earlier.

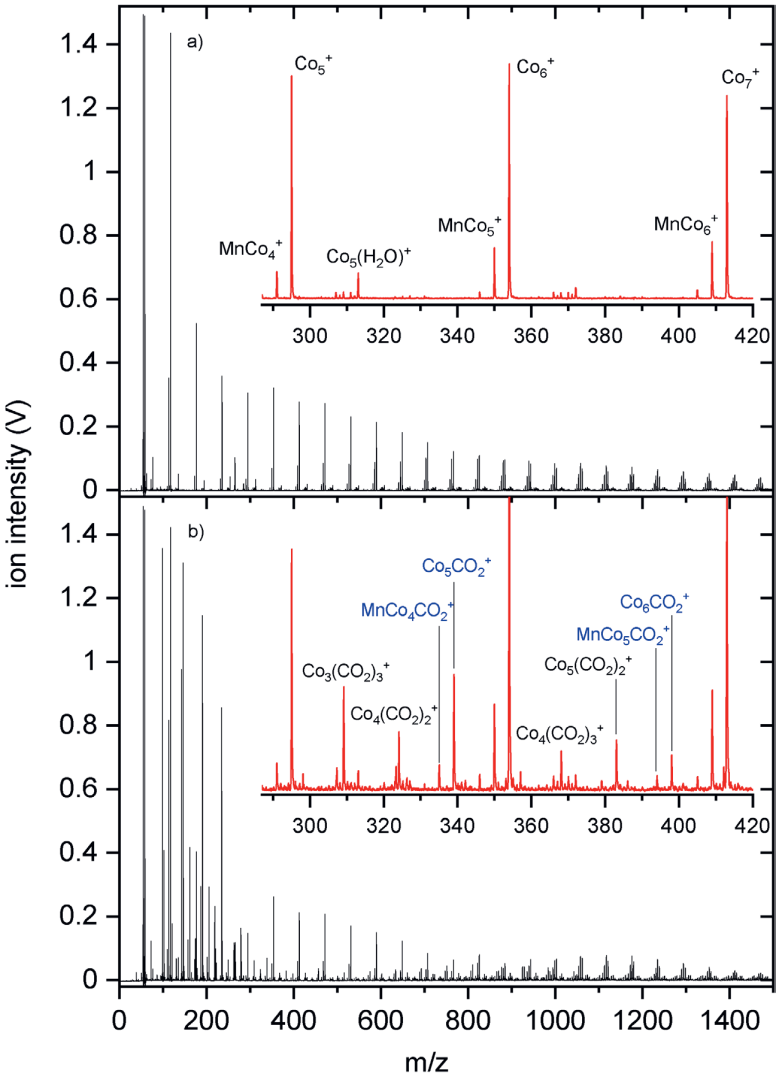

***Figure 4.3**: Mass spectra show a distribution of cationic manganese-doped cobalt clusters (panel a) and CO_2 attached to this mass distribution (panel b). The insets show enlargements of the mass spectra near the Co_5^{+}, Co_6^{+}, and Co_7^{+} clusters.*

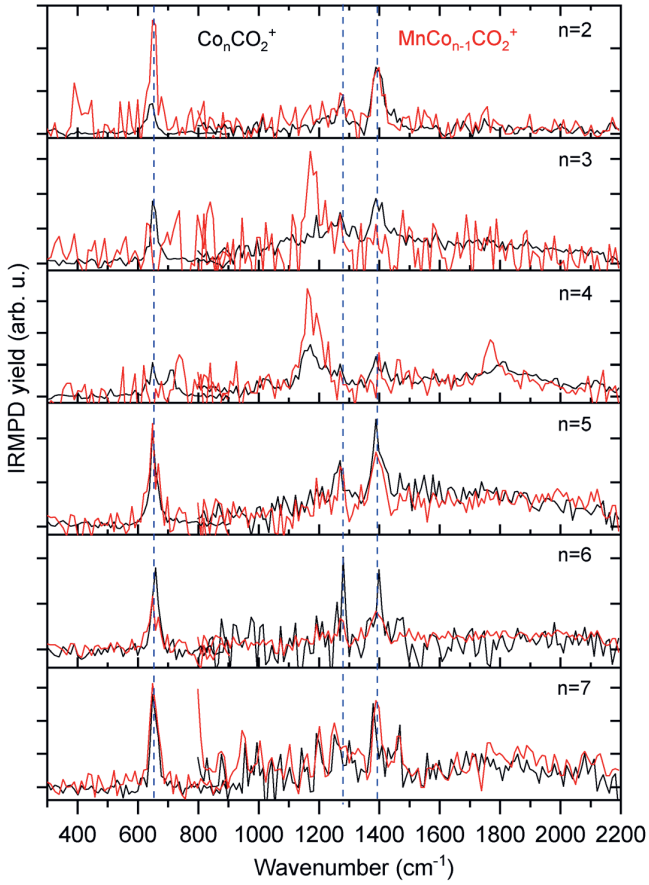

***Figure 4.4**: IRMPD spectra of $Co_n^+ \cdot CO_2$ (black line) and $MnCo_{n-1}^+ \cdot CO_2$ (red line) for n=2–7. Blue dashed lines indicate the line positions of free CO_2 vibrational modes.*

The bands observed around 650, 1300, and 1400 cm^{-1} for $MnCo_{n-1}^+ \cdot CO_2$ (**Fig. 4.4**, red trace) closely resemble those for $Co_n^+ \cdot CO_2$, which are characteristics of physisorbed CO_2. However, the spectra for $MnCo_n^+ \cdot CO_2$ (n =3,4) differ from those for the other cluster sizes. The spectrum for $MnCo_3^+ \cdot CO_2$ displays bands at 737, 1161, and 1768 cm^{-1}, which correspond to the bands observed for activated CO_2, similar to those in the spectrum of $Co_4^+ \cdot CO_2$. For $MnCo_2^+ \cdot CO_2$, the spectrum is very noisy, and the only band clearly discernible is just below 1200 cm^{-1}, which may correspond to an activated CO_2 complex despite the absence of the other two bands.

4.3.3 $CrCo_n^+$

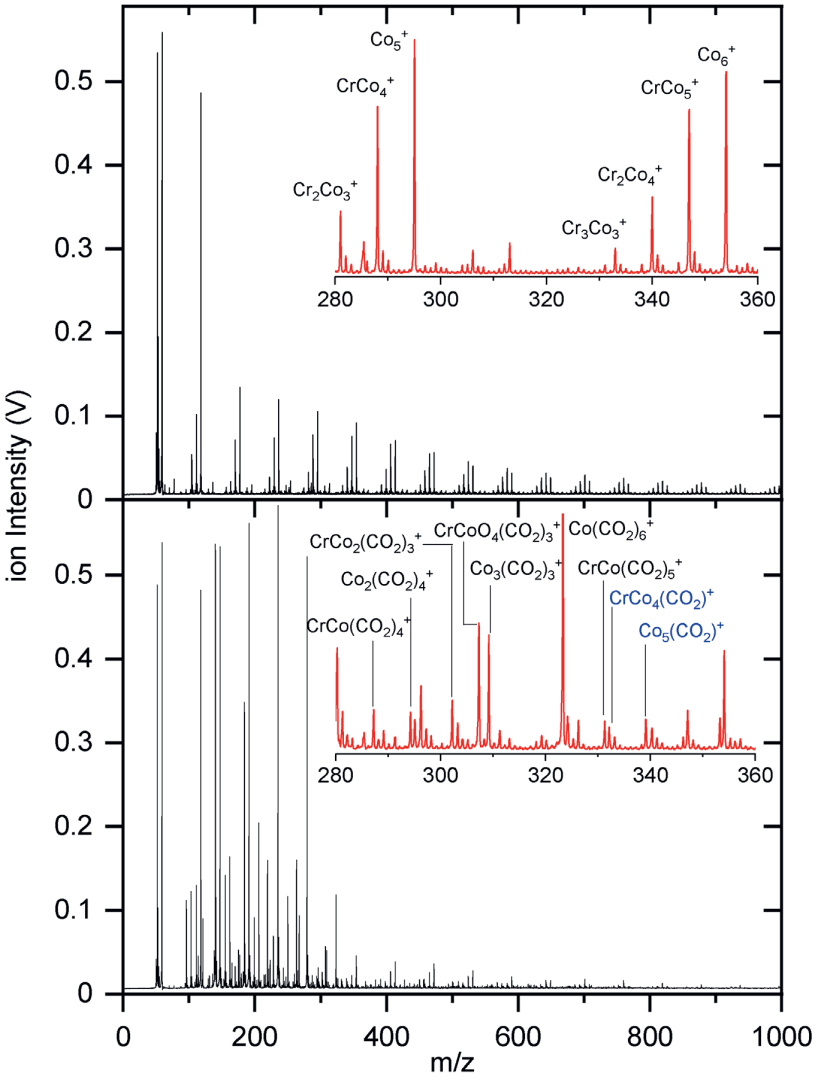

***Figure 4.5**: Mass spectra show a distribution of cationic chromium-doped cobalt clusters (panel a) and CO_2 attached to this mass distribution (panel b). The insets show enlargements of the mass spectra near the Co_5^+ and Co_6^+ clusters.*

Like for the Mn-doped cobalt clusters, typical mass distributions for the Cr-doped Co clusters without and with CO_2 are shown in **Figure 4.5**. The mass spectrum shows both pure cobalt and cobalt clusters doped with one to three chromium atoms. Although chromium has multiple isotopes, it is dominated by Cr-52, and the minor isotopes Cr-50, Cr-53 and Cr-54 only show minor peaks in the mass spectrum. As we have seen before, Co^+ and $CrCo^+$ easily bind many CO_2 molecules, while Co_n^+ (*n*=2-

5) bind up to three CO_2 molecules. Unlike iron or manganese-doped cobalt clusters, we observe two to three CO_2 molecules adsorbed to $CrCo_{n-1}^+$ (n = 3, 5-7). However, no CO_2 adsorption peak is observed in the mass spectrum for $CrCo_3^+$. When reacting with CO_2, there is a notable rise in the mass peaks of $CrCo_3O^+$ and $CrCo_3O_2^+$. The missing $CrCo_3^+{\cdot}CO_2$ peak suggests that CO_2 dissociates during adsorption, and the resulting carbonyl is removed from the cluster. A simultaneous increase in oxides on $CrCo_3^+$ supports this interpretation. A similar situation was observed in our work on vanadium-doped cobalt clusters.[173] The mass spectrum is slightly contaminated with oxides, and these cluster-oxide complexes are also observed to bind CO_2. The mass resolution is sufficient to prevent mass overlap; for example, the peak for $CrCo_4(CO_2)^+$ (m/z=332) is clearly separated from that for $CrCo(CO_2)_5^+$ (m/z=331), which is also visible in the comparison of their IR spectra.

Figure 4.6 shows the experimental IR spectra of $Co_n^+{\cdot}CO_2$ (black trace) and $CrCo_{n-1}^+{\cdot}CO_2$ (red trace) for n = 2–7 in the 450–2200 cm^{-1} range. As before, all $Co_n^+{\cdot}CO_2$ spectra are consistent with those shown in **Figures 4.2** and **4.4**. The spectra for $Co_4^+{\cdot}CO_2$ show a shallow plateau in the 1000 – 2200 cm^{-1} spectral range. This was observed for $Co_4^+{\cdot}{}^{13}CO_2$ in our previous work[173] and was attributed to the presence of low-lying electronic states.[148, 149]

In the spectra of $CrCo_{n-1}^+{\cdot}CO_2$ (**Fig 4.6**, red traces), the bands characteristic of physisorbed CO_2 are present for $CrCo^+$, $CrCo_5^+$ and $CrCo_6^+$, indicating that the dopant atom does not affect activity. The spectra for $CrCo_2^+{\cdot}CO_2$ (n =3) and $CrCo_4^+{\cdot}CO_2$ (n =5) show more bands. For $CrCo_2^+{\cdot}CO_2$, in addition to the bands diagnostic for physisorbed CO_2 at 647, 1268, and 1388 cm^{-1}, a band at 721 cm^{-1} and a broader band at 2096 cm^{-1} are detected. The latter is diagnostic for the carbonyl CO stretch vibration, found at 2143 cm^{-1} for free CO,[150, 151] while the former may be a CoO or CrO stretch. So, the spectrum for $CrCo_2^+{\cdot}CO_2$ could be a mixture of both physisorbed and dissociated CO_2. For $CrCo_4^+{\cdot}CO_2$, hardly any sign of physisorbed CO_2 is observed in the spectrum. Mainly two bands at 1176 and 2013 cm^{-1} are observed, plus two weak features centred at 656 and 724 cm^{-1}. The band at 656 cm^{-1} may be the remaining indication of a marginal population of physisorbed CO_2. The bands at 724 and 2013 cm^{-1}, on the other hand, point to dissociated CO_2. The band at 1176 cm^{-1} appears very similar to a band observed for $Co_4^+{\cdot}CO_2$, which we assigned in our previous work to a symmetric stretch vibration of activated CO_2. The $CrCo_4^+{\cdot}CO_2$ spectrum is thus complex, containing minor traces of physisorbed and activated CO_2, but some prominent features of dissociated CO_2.

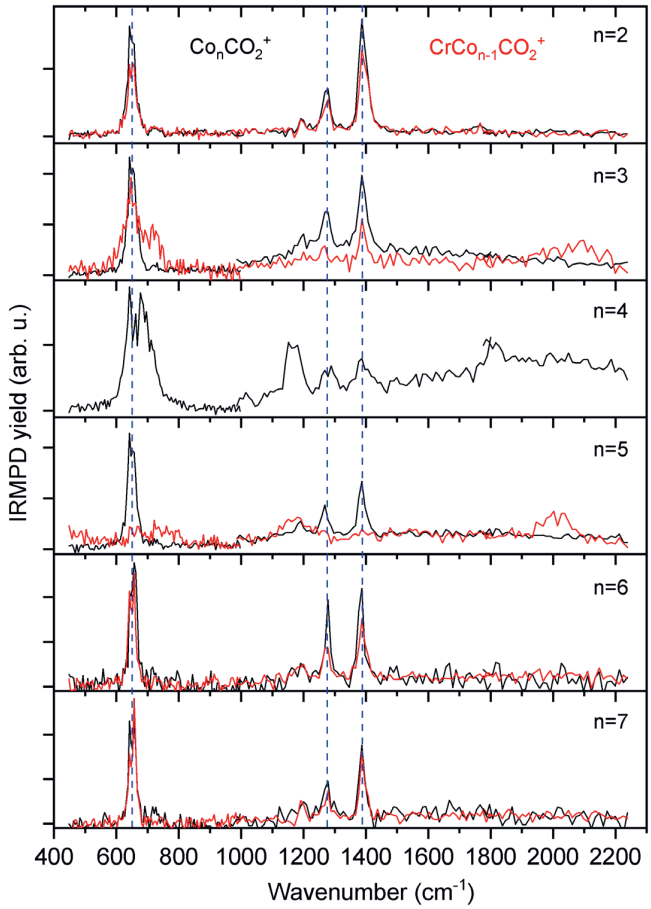

***Figure 4.6**: IRMPD spectra of $Co_n^+ \cdot CO_2$ (black line) and $CrCo_{n-1}^+ \cdot CO_2$ (red line) for n=2–7. Blue dashed lines indicate the line positions of free CO_2 vibrational modes.*

The spectra for CO_2 adsorbed on pristine and Cr-doped cobalt clusters differ at *n* =3 and 5, showing additional bands for doped cobalt clusters in **Figure 4.6**. To confirm the nature of CO_2 binding as discussed earlier and to determine the difference in molecular structure between CO_2 adsorbed on pristine and doped clusters, we performed DFT calculations for *n* =3, specifically for $Co_3^+ \cdot CO_2$ and $CrCo_2^+ \cdot CO_2$, and obtained the corresponding spectra. We chose *n* =3 because it is the smallest cluster size at which a spectral difference between doped and pristine clusters is observed.

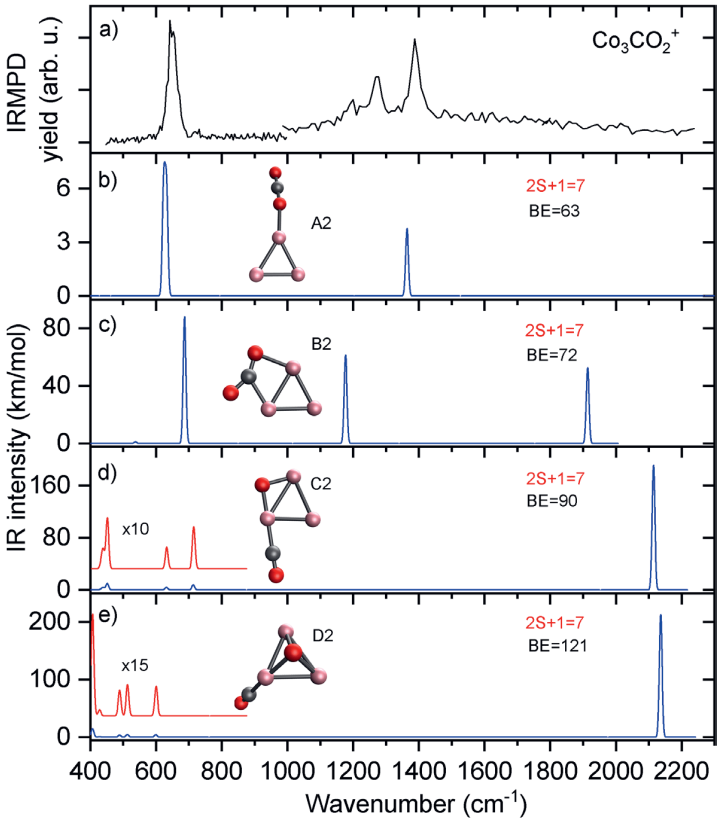

Figure 4.7: Experimental IRMPD spectrum of $Co_3^+ \cdot CO_2$ (panel a) and calculated IR spectra of low-energy structures of physisorbed (panel b), activated (panel c), and dissociated (panels d and e) CO_2 adsorption adducts, each with spin multiplicity 2S+1=7. Binding energies (BE) are shown in kJ/mol.

Figure 4.7 displays a comparison between the experimental spectrum of $Co_3^+ \cdot CO_2$ (panel a) and the calculated spectra for several isomers (panels b-e). As a basis, we used the lowest energy isomer of the bare cluster, triangular Co_3^+ with septet multiplicity. Computed spectra are shown for four possible binding geometries. The first one has a linear CO_2 physisorbed with an oxygen atom η^1-bound to the cobalt atom (structure A2). The second features an activated CO_2 moiety, where CO_2 forms a bent structure and one oxygen binds to the cluster in an η^1 configuration and the carbon in a bridging configuration to two cobalt atoms (B2). The third and fourth are structures with dissociated CO_2. Structure C2 has a separate oxygen atom on the bridge site connecting two cobalt atoms, and the carbonyl (C=O) bound via the carbon atom to a cobalt atom. Structure D2 has a separate oxygen bound to all cobalt atoms in a hollow configuration and the carbonyl bound to a single cobalt atom, similar to C2. The binding energy (BE) of the CO_2 adduct is calculated as the energy

difference between the $Co_3^+ \cdot CO_2$ product and that of the separate reactants [$E(Co_3^+)$ + $E(CO_2)$]. The lowest energy of these structures is for structure D2 at –121 kJ/mol, or 31 kJ/mol lower than the second dissociation product (C2). The product with bent CO_2 (–72 kJ/mol) and with linear CO_2 (–63 kJ/mol) both lie significantly higher in energy.

When comparing the experimental spectrum with the calculated spectrum of physisorbed CO_2 (**Fig. 4.7b**), it is evident that the experimental band at 647 cm^{-1} aligns well with the calculated band at 627 cm^{-1} for the CO_2 bending vibration. The single calculated band at 1363 cm^{-1} is responsible for the experimental peaks at 1273 and 1387 cm^{-1}, because harmonic calculations cannot predict a Fermi resonance, an anharmonic coupling effect, but only the symmetric stretch fundamental vibration. We see no evidence for an experimental band matching the spectrum for activated CO_2 (panel *c*) consisting of three modes at 685 (bend), 1178 (symmetric stretch), and 1914 cm^{-1} (anti-symmetric stretch), or it has to be the tiny band just above 700 cm^{-1}. Panels d and e primarily display a strong band at 2114 and 2138 cm^{-1}, corresponding to a C=O stretch vibration in the product with dissociated CO_2. The remaining bands in the 400-800 cm^{-1} range are significantly less intense and represent some potential cluster vibrations and cobalt oxide stretch. The bands at 439 and 452 cm^{-1} are both Co-C stretches, while those at 632 and 713 cm^{-1} are Co-O stretches in panel *d*. Similarly, the bands at 428 and 488 cm^{-1} are Co-C stretches, whereas the bands at 407, 513, and 599 cm^{-1} are Co-O stretches in panel *e*. No experimental bands have been observed to match any vibrational bands in panels *d* and *e*. Therefore, we conclude that the IR spectrum for $Co_3^+ \cdot CO_2$ is only due to a structure with physisorbed CO_2.

We repeat this exercise for the experimental spectrum of $CrCo_2^+ \cdot CO_2$. **Figure 4.8** shows the experimental spectrum (panel *a*) compared to calculated spectra for several isomers (panels *b*-*e*). Computed spectra are presented for geometries with four potential binding modes, all on the dectet spin surface of the lowest energy bare cluster, a triangular structure. The first structure shown has linear CO_2 physisorbed with an oxygen atom η^1-bound to the chromium atom (structure A1). The structure with CO_2 bound to the cobalt atom lies 10 kJ/mol higher in energy. The second structure, B1, features an activated CO_2, with one oxygen atom bound in an η^1 configuration to a Co atom, the second oxygen atom to Cr and the carbon atom bridge bound to the Cr–Co bond. Structures C1 and D1 have a dissociated CO_2, with the CO bound to a cobalt atom. In C1, the oxygen atom is bound to the Co-Cr bridge; in D1, it is bound to the Cr and two Co. The lowest energy structure among these is

the structure D1 at -179 kJ/mol, much lower than C1 at -113 kJ/mol, let alone the bent adduct at -83 kJ/mol, or the physisorbed adduct at -66 kJ/mol. Other structures, for instance with CO_2 physisorbed on a Co atom or with CO bound to the Cr are higher in energy than the ones shown here.

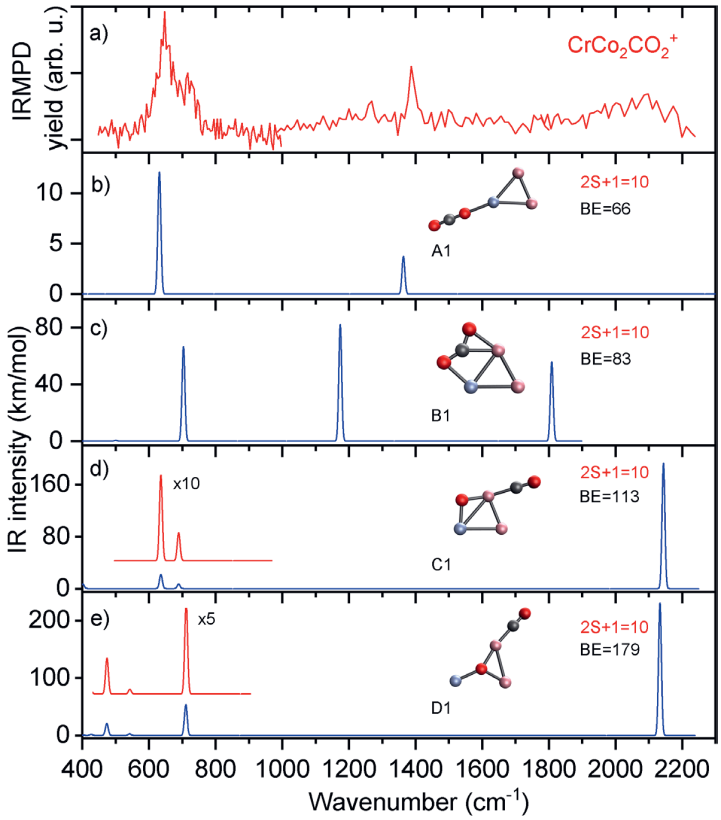

***Figure 4.8**: Experimental IRMPD spectrum of $CrCo_2^+ \cdot CO_2$ (panel a) and calculated IR spectra of low-energy structures of physisorbed (panel b), activated (panel c), and dissociated (panels d and e) CO_2 adsorption adducts, each with spin multiplicity 2S+1=10. Binding energies (BE) are shown in kJ/mol.*

When comparing the experimental spectrum with the spectrum of the cluster with physisorbed CO_2 (panel *b*), the experimental band at 647 cm^{-1} aligns well with the calculated CO_2 bending vibration at 632 cm^{-1}. The Fermi resonance experimental bands at 1268 and 1388 cm^{-1} are reproduced by the single symmetric stretching mode calculated at 1363 cm^{-1}. The experimental spectrum shows no clear match for the bands at 705, 1174, and 1809 cm^{-1} calculated for the bent CO_2 product (panel *c*). In contrast, the spectra calculated for structures with dissociated CO_2 (panels *d* and *e*) both show bands matching the experimental bands at 647, 721, and 2096

cm^{-1}. Clearest match for the 2096 cm^{-1} experimental band is the carbonyl stretch at 2144/2133 cm^{-1} for structure C1/D1, but also the Co–O (689, C1 only) or Cr–O (711, D1 only) stretches show similarity to the 721 cm^{-1} experimental band. Because all other diagnostic bands are much weaker, it is impossible for us to distinguish between structures C1 and D1, but we can conclude that the IR spectrum for $CrCo_2^+ \cdot CO_2$ shows a mixture of clusters with physisorbed and dissociated CO_2.

Potential energy surface for the adsorption and activation of CO_2 on Co_n^+ and $CrCo_{n-1}^+$ clusters

To rationalize the observation of the CO stretch band diagnostic for CO_2 dissociation on $CrCo_2^+$ and its absence for Co_3^+, we evaluated the reaction pathway for adsorption, activation and subsequent dissociation on both $CrCo_2^+$ and Co_3^+ (**Figure 4.9**). The calculations are limited to the spin multiplicity of the lowest energy cluster structure: septet for Co_3^+, and dectet for $CrCo_2^+$. The energy of the reactants, the bare cluster and free CO_2, is chosen as the zero-energy reference point.

For $Co_3^+ \cdot CO_2$ (**Figure 4.9**, black line), the entrance complex is formed by linear CO_2 attached to one of the apices of the triangular Co_3^+ cluster (structure A2), with a binding energy (BE) of 63 kJ/mol. To form a bent CO_2 structure on the cluster (B2, –72 kJ/mol), the linear CO_2 rotates towards the cluster over a submerged transition state (A2', –41 kJ/mol), keeping one oxygen atom O_b on the apex cobalt atom. The carbon atom binds to a second Co atom and the second O_{free} remains unbound. For dissociation, the bound O_b slightly move to form a bridge bond to the two cobalt atoms and the C–O_{free} rotates over the Co–O_b bond after which dissociation ensues and the C=O re-orients into the cluster plane. The cluster with separate CO and O (C2) lies 90 kJ/mol below the reactants, but transition state B2' at +85 kJ/mol, prevents dissociation. In a final rearrangement, the bridge-bound oxygen atom moves over a low transition state (C2') barrier towards a hollow Co–Co–Co site to form a pyramidal structure D2, with CO on a base cobalt atom (–121 kJ/mol). The structure with activated (bent) CO_2, (–72 kJ/mol) lies lower in energy than that with physisorbed CO_2 (–63 kJ/mol), with the latter likely observed in the experiment. This seeming discrepancy may be explained by the possible trapping of CO_2 in the potential well of structure A2, as observed for $Co_5^+ \cdot CO_2$ in our previous work.[173]

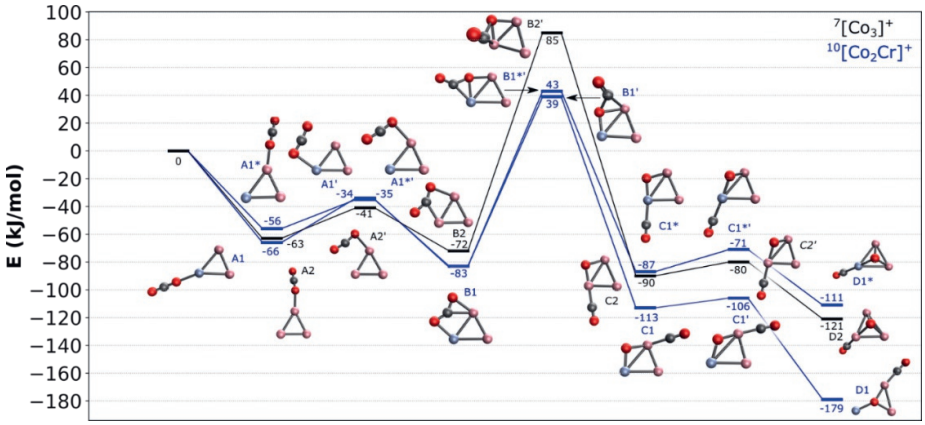

***Figure 4.9**: Potential energy surfaces for the adsorption, activation, and dissociation of CO_2 on Co_3^+ (black, septet spin surface) and $CrCo_2^+$ (blue, dectet) clusters. Relative energies are given with respect to the most stable cluster (our global minimum for the respective size) + free CO_2 molecule. Minima are labelled with capital letters and numbers, with local minima denoted by asterisks; transition states are labelled with a prime. Cr, Co, C, and O atoms are depicted by grey, pink, black, and red spheres, respectively.*

The reaction involving $CrCo_2^+$ is shown by the blue line in **Figure 4.9**. In the entrance complex, linear CO_2 is bound to the chromium atom of the triangular $CrCo_2^+$ (structure A1) with a BE of 66 kJ/mol. Adsorption of linear CO_2 on the cobalt atom (structure A1*) is slightly higher in energy at –56 kJ/mol. To form a bent CO_2 structure (B1, –83 kJ/mol), from both structures A1 and A1*, the linear CO_2 rotates over a transition state (A1' or A1*', -34/35 kJ/mol) directing the second O_{free} atom to a vacant metal atom (Cr or Co) while keeping the originally bound O_b atom fixed to the chromium or cobalt atom. In both cases, it results in a single structure B1, with the carbon atom bridge bound to the Co–Cr bond with oxygen atoms bound to the chromium and cobalt atoms. For CO_2 dissociation, two potential pathways are predicted, either keeping the CO bound to the Co atom (transition state B1' and minimum C1) or to the Cr atom (B1*' and C1*)**.** In both cases C–O bond rupture leads to an O atom bridge bound to Cr–Co bond. Both rate-limiting barriers remain endothermic (43 and 39 kJ/mol for B1*' and B1, respectively), but are roughly half of the barrier calculated for Co_3^+ at 85 kJ/mol. We speculate that the lowering of this barrier will significantly increase the thermal rate for dissociation, and therefore allow dissociation even when the barrier lies above the energy of the reactants.

After bond dissociation a final re-arrangement takes place. The bridge-bound oxygen in structure C1* moves over a small transition state C1*' towards a hollow Cr–Co–Co site to form a pyramidal structure D1* at an energy of –111 kJ/mol. A similar

rearrangement occurs for structure C1, but after. Here, the bridge-bound oxygen inserts itself (over small transition state C1') into the Co–Cr bond to form structure D1, a Co_2O^+ triangular core, with CO bound to a cobalt and the Cr atom bound to the oxygen atom. Structure D1 has the lowest energy in the overall pathway at –179 kJ/mol.

So how can we rationalize the lowering of the rate-limiting barrier for $CrCo_2^+$ with respect to Co_3^+? A first inclination would be to compare the M^+–O bond strengths. The experimental value of bond energy for Cr^+-O is 3.72 eV, which is higher than the Co^+–O bond energy of 3.32 eV. It also exceeds experimental values for Mn^+–O (2.95 eV) and Fe^+-O (3.53 eV), respectively, rationalizing why Cr substitution has the largest impact of the dopants studied here. The Cr^+–O bond strength is larger than the Cr^+–C bond strength (2.87 eV),[183] reflecting the higher energies of structures C1* and D1*.

4.4. Conclusions

We formed cationic cobalt clusters doped with iron, manganese, and chromium atoms, as well as pristine cobalt clusters. These were reacted with CO_2, and the structure of cluster-CO_2 complexes was studied using IRMPD spectroscopy. Adsorption of CO_2 on pure cobalt clusters results in intact physisorption, except for Co_4^+, which shows a mixture of physisorbed and activated CO_2. This aligns well with our previous work on CO_2 adsorption on vanadium-doped cobalt clusters.[173] Doping the cobalt clusters with an Fe atom does not alter their activity towards CO_2, as they exhibit spectra similar to those of $Co_n{\cdot}CO_2^+$ clusters. Doping with a Mn atom alters the activity slightly, with some cluster sizes showing CO_2 activation ($MnCo_2^+$ and $MnCo_3^+$), while CO_2 adsorbs intact on other sizes. The highest activity observed is that for Cr-doped cobalt clusters, with CO_2 dissociation over $CrCo_2^+$ and $CrCo_4^+$ clusters, where other cluster sizes mainly have physisorbed CO_2. DFT-calculated spectra for various isomers of $CrCo_2^+{\cdot}CO_2$ suggest that the experimental spectra represent a mixture of physisorbed and dissociated CO_2. A comparison of the reaction pathway for CO_2 adsorption and subsequent dissociation over Co_3^+ and $CrCo_2^+$ shows that the inclusion of a chromium atom in the cobalt cluster significantly lowers the barrier for CO_2 dissociation, although it is still higher than the energy of the reactants. It is speculated that the thermal energy of the room-temperature experimental reaction is sufficient to overcome this barrier for a fraction of the population, something that would be consistent with the spectral signature of a mixture of physisorbed and dissociated CO_2 on $CrCo_2^+$.

5 Far-infrared spectroscopy of cationic vanadium-doped cobalt clusters

Abstract

Metal clusters can be considered as robust model systems for catalysts, offering the possibility to investigate the effect of doping on the catalytic activity and stability of nanoparticle catalysts. A cluster's chemical activity is often determined by a fine interplay between the strongly intertwined electronic and geometric structures of the cluster. Therefore, to understand the activity of clusters, pristine or doped, in reactions with molecules aimed at designing new catalysts, it is important to know the cluster geometry. Here, we examine the geometry adopted by cationic pure and vanadium-doped cobalt clusters using far-infrared spectroscopy with argon as messenger atom. The experimental spectra of Co_n^+-Ar and VCo_{n-1}^+-Ar (both n= 4-9) are compared, and the spectra of VCo_3^+ and VCo_4^+ are assigned to tetrahedral and trigonal bipyramidal structures by comparing their spectra to density functional theory calculations. It appears that the structures of the doped clusters remain unchanged compared to the pristine form, so the activity of vanadium-doped cobalt clusters is attributed to the oxophilicity of vanadium.

This chapter is adapted from:
D. Pradeep, P. Ferrari, B. Zamora Yusti, T. Höltzl, J. M. Bakker, *in preparation*.

Experimental work was carried out by DP; DFT calculations were conducted by PF, BZY and TH.

5.1. Introduction

Transition metal clusters are of significant interest because they bridge the gap between isolated atoms and bulk materials. Their electronic, magnetic, and chemical properties depend on size, elemental composition and structure,[54, 57, 62, 184] making them essential for both fundamental research and practical uses in catalysis, materials science, and organometallic chemistry. In catalysis, metal clusters can mimic the active sites of nanoparticles; therefore, they are utilised to elucidate catalytic activity in molecular reactions.[47] The aims in studying metal cluster interactions with molecules are to identify the mechanisms, rates, and energetics of adsorption, and to understand how these properties depend on the subtle interplay between the electronic structure and the geometry of the bare clusters. Therefore, understanding the geometry of isolated metal clusters is crucial for comprehending their chemical and physical behaviour.

Gas-phase clusters serve as a suitable model system for real-world catalysts to study the molecular-level interactions.[57, 58, 66, 136] For example, significant research efforts have been dedicated to understand the CO_2 adsorption on metal ions[72, 81] and single metal clusters[74-79] as a first step in the catalytic CO_2 hydrogenation reaction. However, single metal clusters often lack stability and activity, and, furthermore, catalytic materials are usually more complex than simple single-element clusters. This is evident from the complex nature of the conventional $Cu/ZnO/Al_2O_3$ catalyst used for the CO_2 hydrogenation reaction to methanol, where Cu-Zn or Cu-ZnO sites can enhance the catalyst's activity.[13, 83, 169, 171, 172, 185] Therefore, the study of doped metal clusters interacting with molecules (such as CO_2) can be instructive to understand the influence of the dopant on cluster activity.[84]

Doping cobalt clusters with other elements can change their electronic and geometric structures, potentially changing their reactive and magnetic properties. For example, the inclusion of vanadium atoms in cobalt clusters enhances their activity towards H_2.[86, 90] The electronic structure of the cobalt clusters changes significantly upon addition of a benzene molecule, resulting in the quenching of magnetic moments.[186] Similarly, chromium doping of cobalt clusters results in a size-dependent variation in magnetic coupling with respect to cobalt clusters.[187] Additionally, in our previous work on CO_2 activation on first-row transition metal-doped cobalt clusters,[173, 188] doping with vanadium promoted CO_2 dissociation compared to molecular adsorption on pristine cobalt clusters. This is due to the stronger V-O bond energy compared to that of late transition metals,[108] which

enables vanadium to attract the oxygen atom(s) in the CO_2, thereby destabilising the molecule. Because the difference in activity could also arise from the distinct electronic and geometric structures of the pure and doped cobalt, examining the structure of the vanadium-doped cobalt clusters is particularly interesting.

The structures of gas-phase metal clusters can be determined by combining ion mobility or trapped ion electron diffraction experiments with theoretical calculations.[189-192] Information on the electronic structure can be determined using, e.g., photoelectron spectroscopy or optical photodissociation spectroscopy. An alternative technique for studying the geometry of bare clusters is infrared vibrational spectroscopy. However, in most cases, metal clusters are produced in molecular beams or ion traps; their low particle density makes direct absorption spectroscopy difficult. Although cavity ring-down spectroscopic studies, monitoring direct optical absorption, of size-selected clusters in ion traps exist,[193] such experiments remain challenging. Photofragmentation spectroscopy is a more robust technique, and infrared multiple-photon dissociation (IRMPD) spectroscopy is frequently used to study the structure of cluster-molecule complexes. [194, 195] For that to work, the clusters must be excited to sufficiently high energies so that they can dissociate, which becomes difficult when the binding energy of the system is high with respect to the employed photon energy. Therefore, a modified technique, infrared messenger-tagging spectroscopy, can be employed.[66, 116, 196, 197] Here, the spectrum of a weakly bound complex between a cluster and a messenger atom is recorded, and used as a proxy for the spectrum of the bare cluster, under the assumption that the messenger atom does not change the cluster geometry. The weak bond between cluster and messenger reduces the number of IR photons required for dissociation of the cluster-messenger complex, thereby increasing the sensitivity of the spectroscopy. This technique has been successfully used for monometallic as well as various bimetallic clusters.[117, 175, 197, 198]

The electronic and geometric structures of cobalt clusters have been previously studied. The electronic structure of anionic and cationic cobalt clusters was investigated using photoelectron and photodissociation spectroscopy of cobalt-Ar/Kr complexes,[149, 199, 200] respectively. Moreover, the geometry of cationic cobalt clusters was studied using messenger-tagging spectroscopy.[117] For vanadium-doped cobalt clusters, the stability of the clusters was investigated previously using photodissociation spectroscopy.[201] Also, the electronic properties and activity of vanadium-doped cobalt clusters have been examined using anionic photoelectron spectroscopy,[202] and it was found that size-selective activity is closely related to the

cluster geometry. In this work, we report the geometry of vanadium-doped cobalt clusters using far-infrared spectroscopy with argon as a messenger atom. The IR spectra of argon-tagged vanadium-doped cobalt clusters are benchmarked with the theoretical spectra predicted by density functional theory calculations, which allows a determination of the lowest-energy structures of the doped species.

5.2. Methods

5.2.1 Experimental

The experiments were carried out in a molecular beam setup coupled to the cavity of the Free Electron Laser FELICE,[123, 124] housed at HFML-FELIX. The cationic cobalt and vanadium-doped cobalt clusters were generated in a dual-target, dual-laser ablation source[87, 88] located in the source chamber of this setup, as explained elsewhere[173] and in Chapter 2. A mixture of 5% argon in helium is used as the carrier gas to promote cluster formation and to complex the cobalt- and vanadium-doped cobalt clusters with Ar. To efficiently adsorb Ar on the investigated cluster distribution, an additional cooling of the reaction channel, isolated from the clustering channel, was achieved by a combination of liquid nitrogen flow and resistive heating to maintain a stable temperature at -50 °C.

The mixture of clusters and cluster-argon complexes was then expanded into vacuum to produce a molecular beam. The beam was collimated by a 2-mm-diameter skimmer and further shaped by a 2-mm-high slit aperture, both of which were electronically grounded, to match the size of the molecular beam to that of the IR laser beam. The beam reached the interaction zone, where it was irradiated with the FELICE IR laser beam at frequencies ranging from 100 to 360 cm^{-1}. After irradiation, all ions were pulse-extracted into a perpendicular reflectron time-of-flight mass spectrometer (Jordan TOF Products, Inc.) by applying high voltages on two parallel plate electrodes surrounding the interaction zone, and detected on a microchannel plate-based detector.

When the IR laser was in resonance with the vibrational frequency of the cluster-argon complexes, one or more photons were absorbed, resulting in a breaking of the weak VCo_{n-1}^{+}-Ar (*n* is the number of cobalt atoms) bond. This fragmentation was registered as a decrease in the intensity of the VCo_{n-1}^{+}-Ar mass peak and a simultaneous increase in that of the VCo_{n-1}^{+} channel. IR spectra were obtained by recording the changes in intensity of these mass peaks across different IR wavelengths. To detect this intensity depletion, the experiment was operated at 10

Hz, while FELICE ran at a 5 Hz repetition rate. With each FELICE shot, mass spectra were recorded with and without IR irradiation.

The complexation of cobalt clusters and vanadium-doped clusters with Ar atoms is strongly affected by temperature and Ar concentration. Due to the relatively high concentration of argon in the carrier gas, multiple argon atoms could be attached to clusters with n ≤ 5. This was done deliberately to ensure Ar attaches to all cluster sizes studied. Complexes of clusters with multiple Ar atoms (VCo_{n-1}^{+}-Ar_m) may fragment at the same resonant frequency as that of the clusters with one Ar atom. This could result in the partial or complete suppression of the absorption band for VCo_{n-1}^{+}-Ar by the ingrowth of fragments of the larger complexes. To eliminate this contribution to the spectra of the VCo_{n-1}^{+}-Ar complexes, the branching ratio B_n (explained in detail in Chapter 2) of the summed mass-spectrometric intensities I_m of all cluster-Ar_m (m=1–4) complexes formed to the sum I_m including all clusters and cluster complexes (m=0–4) is used. The number of argon atoms used in the branching ratio equation for each cluster size is as follows: for cluster size n=4, four argon atoms (m=4); for n=5, two argon atoms (m=2); and from n=6 onwards, only one argon atom (m=1) is used. To compare the IR spectra of VCo_3^{+}-Ar and VCo_3^{+}-Ar_2 to the computational spectra (discussed in section 5.3), the spectrum for VCo_3^{+}-Ar is plotted by considering the branching ratio and for VCo_3^{+}-Ar_2, the spectrum is plotted without it.

5.2.2 Computational

Density functional theory calculations on VCo_3^{+}-Ar and VCo_4^{+}-Ar complexes were performed using the ORCA 6.01 software package.[203] First, a structural search for VCo_3^{+} and VCo_4^{+} was performed with the GOAT conformational search algorithm,[204] as implemented in ORCA, leading to 19 and 61 conformations for VCo_3^{+} and VCo_4^{+}, respectively. Of these set of structures, the five lowest in energy were subsequently reoptimized at the DFT level using the PBE functional in conjunction with the def2-TZVP basis set, at 2S+1 spin multiplicities of 2 and 4 for VCo_3^{+} and 3, 5 and 7 for VCo_4^{+}. This re-optimization leads to four distinct conformations for VCo_3^{+} and two for VCo_4^{+}, at the various spin multiplicities. Finally, calculations using the TPSSh/def2-TZVP[134, 145] functional/basis set combination was conducted, including Ar atoms at all possible coordination sites of the clusters, for which the DB3J dispersion correction was included. In this case, harmonic frequency calculations were performed, confirming that all conformations are true minima within the PES and allowing the comparison with experimental IR spectra.

5.3. Results and discussion

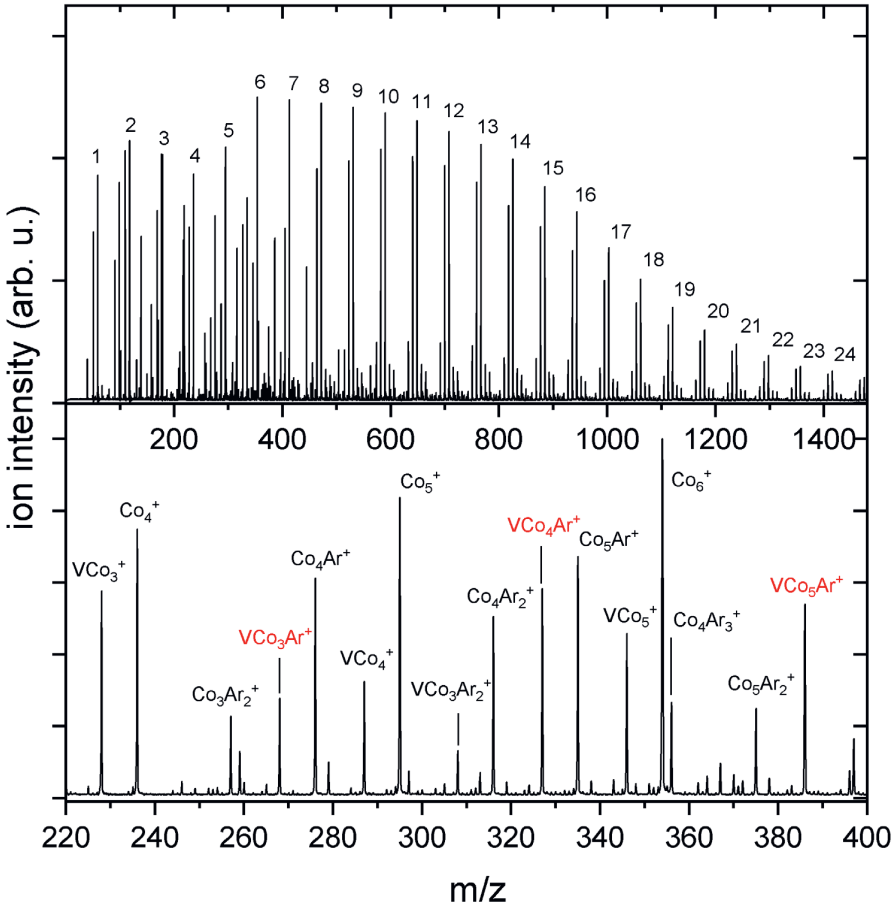

Figure 5.1: The top panel shows the mass spectrum of the distribution of the argon-tagged cationic cobalt and vanadium-doped cobalt clusters. The bottom panel shows the mass spectrum where masses formed near the Co_4^+, Co_5^+, and Co_6^+ mass channels are enlarged.

Figure 5.1 (top panel) illustrates a typical mass spectrum for argon-tagged cationic cobalt and vanadium-doped cobalt clusters. The bottom panel displays all the masses formed near the Co_4^+, Co_5^+, and Co_6^+ clusters, where one argon attached to the vanadium-doped cobalt clusters is denoted by red. It can be seen that under the current conditions, some Co_n^+ and VCo_{n-1}^+ clusters (especially the smaller clusters, like n=3, 4, and 5 shown in the bottom panel) bind two to four argon atoms.

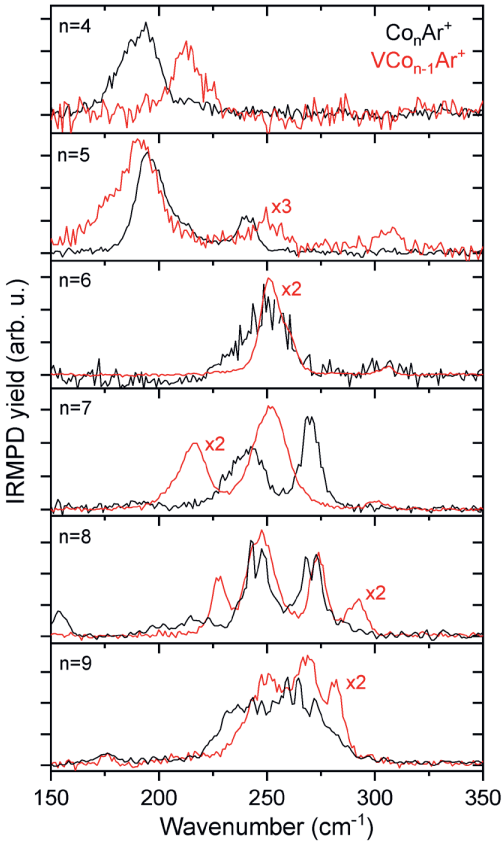

Figure 5.2: The infrared spectra of argon-tagged cationic cobalt (black) and vanadium-doped cobalt clusters (red) for cobalt sizes n=4 to 9.

Figure 5.2 presents the experimental infrared spectra for argon-tagged cationic cobalt (black line) and vanadium-cobalt (red line) clusters of sizes n = 4– 9. For cluster sizes n < 4, depletion is not observed, most likely due to the relatively high binding energy of the Ar to the cluster in these complexes. The spectra are recorded in the 150-350 cm^{-1} range. All spectra are the average of several individual scans, but no smoothing is done, except for Co_8^+-Ar and Co_9^+-Ar, where the IR spectra are smoothed using a five-point moving average. The IR spectra measured here for Co_n^+-Ar (n=4–8) correspond well with previously measured spectra by Gehrke et al.[117] In that work, the distributions were tuned such that ingrowth from larger clusters was reduced as much as possible. It can be seen that our use of the branching ratio to suppress such ingrowth effects yields very similar spectra as found for Co_n^+-Ar in that previous work, validating our choice.

As can be seen by comparing the spectra pairwise in **Figure 5.2**, substituting a cobalt atom by a vanadium atom does not significantly alter the IR spectra: most of the spectra for VCo_{n-1}^+-Ar are very similar to spectra for Co_n^+-Ar. The IR spectrum of Co_4^+-Ar (*n*=4, black line) shows a single, broad band at 194 cm^{-1}, whereas that for VCo_3^+-Ar (*n*=4, red line) shows a band at 213 cm^{-1}. The spectrum for Co_5^+-Ar (*n*=5) exhibits two peaks at 195 and 242 cm^{-1}. For VCo_4^+-Ar (*n*=5, red line), these bands are replicated by bands at 191 and 249 cm^{-1}, with an extra, weaker band appearing at 308 cm^{-1}. The spectrum of Co_6^+-Ar, is a little noisy, but a broad band maximum at 248 cm^{-1} and a weaker band at 303 cm^{-1} are observed. The IR spectrum of VCo_5^+-Ar, with a much higher signal-to-noise ratio shows a peak at 251 cm^{-1} and a weak band at 306 cm^{-1}. For Co_7^+-Ar, finally, the spectrum shows peaks at 243 and 269 cm^{-1}; the spectrum for VCo_6^+-Ar closely resembles that of Co_7^+-Ar, but the bands are significantly redshifted with the two major bands at 216 and 251 cm^{-1}. Additionally, a weaker band at 301 cm^{-1} appears. The spectra for *n*=8 show the largest difference upon introducing the dopant atom. The spectrum of Co_8^+-Ar shows two main bands at 244 and 270 cm^{-1}, with a weaker sideband at 215 cm^{-1} and a clear resonance at 154 cm^{-1}. Interestingly, the spectrum of VCo_7^+-Ar is radically different with bands at 227, 248, 273, and 292 cm^{-1}. The spectrum of Co_9^+-Ar is much broader than that for other cluster sizes, with a broad band with a maximum at 259 cm^{-1} that looks saturated, and a weaker band at 176 cm^{-1}. The spectrum of VCo_8^+-Ar has a similar structure but the broad band around 250-285 cm^{-1} has clear maxima at 249, 269, and 282 cm^{-1} and the weaker band remains at the same frequency 176 cm^{-1}.

To understand the difference in the geometry of VCo_3^+ compared to Co_4^+, the experimental IR spectrum (red) of VCo_3^+-Ar is compared to computational spectra of two of the four isomers calculated in **Figure 5.3** (left). The theoretical spectra are displayed as sticks (black) and convolutions (blue traces) using Gaussian line-shape functions with a FWHM of 0.4% of the central wavelength of FELICE to facilitate comparison with the experiment. The spectra are displayed within the 150-350 cm^{-1} range.

In the literature, for Co_4^+, the experimental IR spectrum matched the calculated spectrum for a distorted tetrahedron structure.[117] Here, in the case of VCo_3^+, four isomers are predicted: a tetrahedron, a distorted rhombus (vanadium on the short and long axes), and a planar rhombus. The tetrahedron (4T) and distorted rhombus (4R) with vanadium on the short axis have the lowest possible energies, even though the true lowest energy isomer was not found. Each isomer is calculated for doublet and quartet spin states. The tetrahedron structure with quartet spin state (^{4}4T) is

calculated to be the global minimum. The distorted rhombus with quartet spin state (^{4}4R) lies 0.1 eV above the ^{4}4T isomer. The tetrahedron, now with a doublet spin state (^{2}4T), has 0.4 eV more energy than the global minimum. After that, the other two isomers—a planar rhombus and a distorted rhombus (V on the long axis)—with doublet spin states have energies 0.7 and 0.8 eV higher than isomer ^{4}4T.

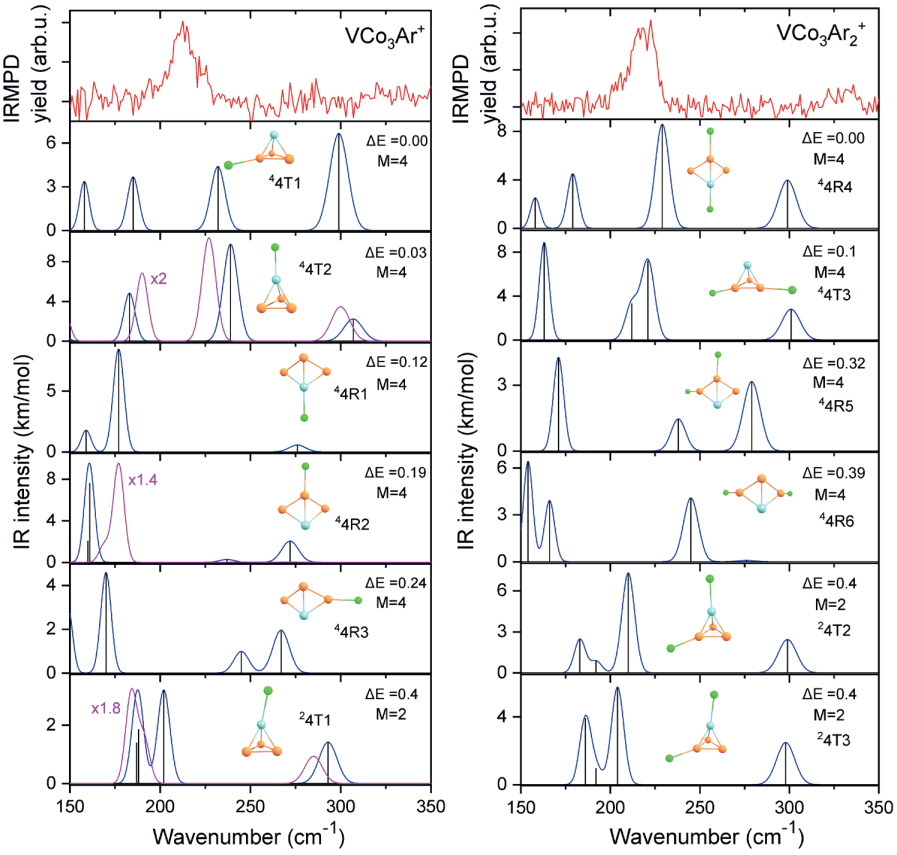

***Figure 5.3**: Experimental IR spectra of VCo_3^+-Ar and VCo_3^+-Ar_2 (top panels) and calculated spectra (stick and convoluted) of two isomers at spin multiplicities M=2S+1 of 2 and 4, where a single Ar atom (left column) and two Ar atoms (right column) are attached at different positions of the structures. The calculated vibrational spectra of bare clusters are shown in magenta. The relative energy (ΔE) with respect to the lowest energy structure is given in eV.*

To assign the cluster geometry, the experimental IR spectrum is compared with the calculated spectra of bare VCo_3^+ in **Figure 5.3** (left, magenta line). The IRMPD spectrum appears to have the best match with the calculated spectrum of the isomer ^{2}4T, where the experimental bands at 213 and 325 cm^{-1} closely match the computational bands at 184 and 285 cm^{-1}.

To compare the experimental spectrum of VCo_3^+-Ar to calculated spectra including the Ar atom, we introduce the following nomenclature: structures derived from these lowest energy isomers of the bare cluster are labelled with the corresponding capital, and a numeral describing their relative energies. Each isomer is calculated for the doublet and quartet spin multiplicities, as well as for various coordinations of the Ar atoms. For the tetrahedron isomer (4T), an Ar atom can bind either to the cobalt or the vanadium atom. The isomer on the quartet spin surface with Ar binding to the Co atom(^{4}4T1) has the lowest energy, followed by ^{4}4T2 (Ar binds to the V atom), which is only 0.03 eV higher. Now, on the doublet spin surface, Ar binds to the vanadium atom (^{2}4T1), which has an energy of 0.4 eV higher than ^{4}4T1. For the distorted rhombus isomer on the quartet spin surface, there are three possibilities: the Ar atom can bind either to the vanadium atom (^{4}4R1) or the cobalt atom on the short (^{4}4R2) or long axis (^{4}4R3). These structures have energy differences of 0.12, 0.19, and 0.24 eV relative to the ^{4}4T1 structure.

To determine whether Ar binding perturbs the system, the calculated spectra of tagged and bare clusters are shown next to each other. The tagging of an Ar atom to the vanadium atom does not change the spectra for bare VCo_3^+ in the case of ^{4}4T2 and ^{2}4T1, except for minor frequency shifts in the bands. The calculated binding energy between the vanadium and the Ar atom in structures ^{4}4T2 and ^{2}4T1 is 0.3 and 0.33 eV, and the attachment barely changes the cluster structure. For ^{4}4T1, an extra band appears in the IR spectrum when Ar is tagged to the cobalt atom and the binding energy between Co and Ar is calculated to be 0.33 eV. Upon Ar binding to the distorted rhombus VCo_3^+, the calculated spectra for the isomers ^{4}4R1, ^{4}4R2, and ^{4}4R3 are different from the bare cluster. Two additional bands appear relative to the bare VCo_3^+. The calculated binding energy for Ar attaching to the V atom in structure ^{4}4R1 is 0.32 eV, whereas Ar binds the Co atom in ^{4}4R2 and ^{4}4R3 structures with binding energies of 0.25 and 0.97 eV, respectively.

When comparing the experimental spectrum of VCo_3^+-Ar with the calculated spectrum of structure ^{4}4T1, none of the four computed bands at 158, 185, 232 and 299 cm^{-1} form a match for the experimental bands at 213 and 325 cm^{-1}. Similarly, the calculated bands for structure ^{4}4T2 at 183, 239, and 307 cm^{-1} do not match the experimental spectrum either. In contrast, the calculated spectrum for structure ^{2}4T1 matches the experimental spectrum reasonably well. Three bands are predicted at 188, 202, and 293 cm^{-1}, which are close to the experimental bands. It appears plausible that the – relatively broad – experimental band at 213 cm^{-1} is the result of the two vibrational modes. For the distorted rhombus structures ^{4}4R1, ^{4}4R2,

and ^{4}4R3, none of the calculated spectra matches the experimental spectrum. Again, three bands are predicted for structure ^{4}4R1, at 159, 177, and 276 cm^{-1}. For the ^{4}4R2 structure, the bands appear at 161, 238, and 272 cm^{-1}, while for the ^{4}4R3 structure, the peaks are at 170, 245, and 267 cm^{-1}. Therefore, at the current level of theory, we assign the spectrum of VCo_3^+ to a symmetric tetrahedron with a doublet spin multiplicity. This is consistent with the previous assignment of the spectrum of Co_4^+-Ar to a distorted tetrahedron structure.

Cluster	Structure	Relative Energy (eV)	Binding Energy (eV)
VCo_3^+	^{4}4T	0.00	
	^{4}4R	0.10	
	^{2}4T	0.40	
VCo_3^+-Ar	^{4}4T1	0.00	0.33
	^{4}4T2	0.03	0.30
	^{4}4R1	0.12	0.32
	^{4}4R2	0.19	0.25
	^{4}4R3	0.24	0.97
	^{2}4T1	0.40	0.33
VCo_4^+	^{7}5A	0.00	
	^{3}5A	0.20	
	^{5}5A	0.40	
VCo_4^+-Ar	^{7}5A1	0.00	0.31
	^{7}5A2	0.05	0.27
	^{7}5A3	0.15	0.17
	^{3}5A1	0.29	0.19
	^{3}5A2	0.36	0.13
	^{5}5A1	0.39	0.30
	^{5}5A2	0.47	0.22

***Table 5.1**: Relative energies between different isomers of bare and argon-tagged VCo_3^+ and VCo_4^+ clusters and binding energies of the Ar atom to the respective bare clusters.*

To confirm this assignment for VCo_3^+ and that the weak experimental band at 325 cm^{-1} really exists, the experimental spectrum of VCo_3^+-Ar_2 is compared with the calculated spectra of isomers with two Ar atoms in **Figure 5.3** (right). The experimental spectrum of VCo_3^+-Ar_2 is very similar to that of VCo_3^+-Ar, but the weaker band at 325 cm^{-1} is more pronounced. For VCo_3^+-Ar_2, the lowest energy structure calculated is ^{4}4R4, where Ar atoms bind to the diagonally opposite vanadium and cobalt atom. The tetrahedron structure (^{4}4T3) with Ar atoms tagged to the cobalt atoms on the base position has the next lowest energy, at 0.1 eV

relative to the ^{4}4R4 isomer. After that, the distorted rhombus structure ^{4}4R5 with two Ar atoms binding to the cobalt atoms in the short and long axes, has an energy of 0.32 eV higher than ^{4}4R4. Next, the isomer ^{4}4R6 with Ar atoms binding to the Co atoms in the long axis, is 0.39 eV higher in energy than ^{4}4R4. Finally, two structures having the same spin multiplicity, ^{2}4T2 and ^{2}4T3, with two Ar atoms binding to the cobalt and vanadium atom, have the same energy of 0.4 eV with respect to the lowest energy structure, ^{4}4R4. The only difference between them is the orientation of the Ar atom relative to the vanadium atom in their structures.

When comparing the experimental spectrum of VCo_3^+-Ar_2 with the calculated spectrum of ^{4}4R4, the calculated bands at 158, 178, 229, and 299 cm^{-1} do not correspond with the experimental bands at 219 and 332 cm^{-1}. Similarly, structure ^{4}4T3 with calculated bands at 163, 212, 221, and 301 cm^{-1} does not match the experimental spectrum well either. In both cases, the main band at 219 cm^{-1} is plausibly reproduced by the calculations, but no sign of the other relatively intense bands is seen experimentally. The same arguments exclude the presence of rhombic structures ^{4}4R5 and ^{4}4R6. In contrast, the band calculated for structure ^{2}4T2 at 183, 192, 210 and 299 cm^{-1} are pretty close to the experimental bands. The experimental band at 219 cm^{-1} may include the first three calculated bands, which are not well resolved. Additionally, the structure ^{2}4T3, similar to ^{2}4T2, predicted bands at 186, 192, 204, and 298 cm^{-1}, also providing a good match with the experimental bands. Therefore, we conclude that the structure of VCo_3^+ is most likely a tetrahedron with doublet spin multiplicity.

Similar to VCo_3^+, the structure of VCo_4^+ is elucidated by comparing the experimental IR spectrum of VCo_4^+-Ar with calculated stick (black) and convoluted (blue) spectra of isomers with different spin multiplicities and Ar binding sites, as shown in **Figure 5.4**. For Co_5^+, the experimental bands closely matched the computed spectrum for a distorted trigonal bipyramidal structure.[117] Without Ar binding, two isomers, a distorted trigonal bipyramid (5A) with vanadium at the apex position and the other with vanadium at the base position (5B), are evaluated for VCo_4^+. The trigonal bipyramidal structure on the septet spin surface (^{7}5A) is calculated to have the lowest possible energy. The same structures now on triplet (^{3}5A) and quintet (^{5}5A) surfaces have energies of 0.2 and 0.4 eV higher than structure ^{7}5A. Next, the 5B isomer with septet multiplicity (^{7}5B) is 0.45 eV higher in energy than isomer ^{7}5A. Similar isomers on the triplet (^{3}5B) and quintet (^{5}5B) spin surfaces have energies of 0.9 and 1.2 eV relative to the lower energy structure ^{7}5A. To compare with the experimental spectrum, the calculated spectra for bare VCo_4^+ are plotted in **Figure**

5.4 (magenta curves). The isomer with quintet spin multiplicity (^{5}5A), having calculated bands at 155, 168, 187, 261, and 292 cm^{-1}, is in good agreement with the experimental bands at 191, 249, and 308 cm^{-1} by considering that the broad band at 191 cm^{-1} could contain the first three computational bands.

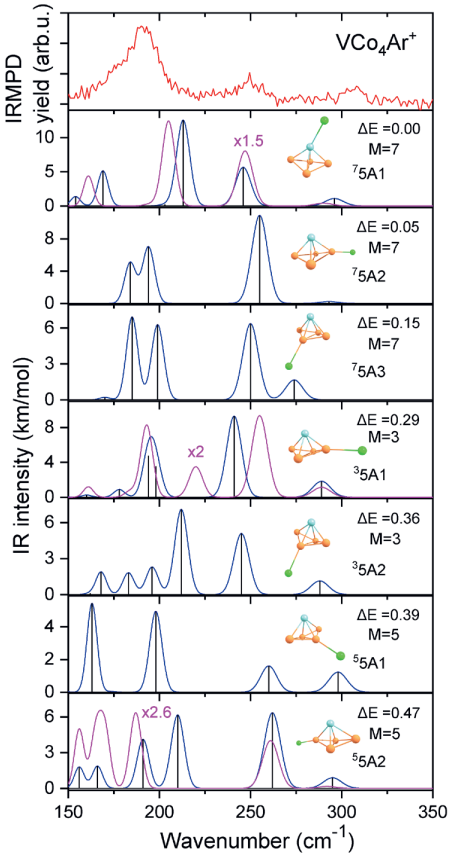

***Figure 5.4**: The experimental IR spectrum of VCo_4^+-Ar (red) is compared with the calculated spectra (stick and convoluted) of an isomer with different spin multiplicities (three, five, and seven) and an Ar atom binding to different sites. The relative energy (ΔE), measured in eV, is with respect to the lowest energy structure. The calculated vibrational spectra of bare clusters are shown in magenta.*

For Ar tagged species, each isomer is calculated for the triplet, quintet and septet spin multiplicities, as well as for various coordinations of the Ar atoms. The lowest energy structure is a trigonal bipyramid (^{7}5A1) with the Ar atom bound to the apex vanadium atom. The same structure and spin multiplicity, but with an Ar atom bound to the base cobalt atoms, ^{7}5A2 and ^{7}5A3, are 0.05 and 0.15 eV higher in energy than the ^{7}5A1 isomer. The same structure, but on the triplet spin surface, ^{3}5A1 and ^{3}5A2, with an Ar atom attached to the base cobalt atoms, have energies 0.29 and 0.36 eV

higher than ^{7}5A1. Finally, the same isomers and exact order of binding of the Ar atom, but now with a quintet spin multiplicities, ^{5}5A1 and ^{5}5A2, are at an energy difference of 0.39 and 0.47 eV compared to the ^{7}5A1 isomer.

Tagging of Ar on the vanadium atom in structure ^{7}5A1 does not significantly alter the calculated spectrum of bare VCo_4^+; only a small additional band is observed. The calculated binding energy of Ar to the vanadium atom in structure ^{7}5A1 is 0.31 eV. When Ar binds at cobalt sites (^{7}5A2 and ^{7}5A3), the spectrum of the bare cluster is drastically frequency shifted, and the calculated binding energies are 0.27 and 0.17 eV, respectively. The calculated spectrum of bare VCo_4^+ on the triplet spin surface is compared to the spectrum of ^{3}5A1; only minor differences are seen. The frequencies are shifted, and the peak-intensity distribution varies, but no additional bands are observed. Nevertheless, in comparison to isomer ^{3}5A2, in addition to frequency shifts and intensity variations, an additional band appears in the tagged spectrum. The binding energy of the Ar atom to the cobalt atom in structures ^{3}5A1 and ^{3}5A2 is 0.19 and 0.13 eV. Similarly, when comparing the spectrum of VCo_4^+ on the quintet spin surface to the spectrum of the ^{5}5A1 isomer, the spectrum for the bare cluster slightly changes, with a band that disappears in the tagged spectrum. However, an extra band appears in the spectrum of the isomer ^{5}5A2 in comparison to the bare cluster spectrum. The binding energies between Ar and Co atoms for the former and latter structures are calculated to be 0.3 and 0.22eV, respectively.

When comparing the experimental spectrum of VCo_4^+-Ar with the computed spectrum of ^{7}5A1, the calculated bands at 154, 169, 213, 246, and 296 cm^{-1} do not match the experimental bands, except for the 246 and 296 cm^{-1} bands, which are close to the experimental bands at 249 and 308 cm^{-1}. For structure ^{7}5A2, the calculated bands are at 184, 194, and 255 cm^{-1}, and a tiny band at 293 cm^{-1}. The first three bands are close to the experimental bands at 191 and 249 cm^{-1}, but the fourth one is relatively weak and does not match the 308 cm^{-1} experimental band. This is almost similar for the ^{7}5A3 isomer, in which the calculated bands are at 170, 185, 199, 250, and 274 cm^{-1}, and the final band at 274 cm^{-1} is far from the experimental. However, the bands predicted for structure ^{3}5A1 are even closer to the experimental bands, but the intensity distribution differs slightly. In the experimental spectrum, the band at 191 cm^{-1} is more intense than the other bands, but this is even more pronounced for the 241 cm^{-1} band in the computed spectrum with peaks at 160, 178, 194, 198, 241, and 289 cm^{-1}. However, for the ^{3}5A2 isomer, the calculated bands at 168, 183, 196, 212, 245, and 288 cm^{-1} match very well with the experimental bands in frequency and also in the intensity distribution, and the broadness of the

experimental band at 191 cm^{-1} is most likely due to the presence of the first four calculated bands. For the structure ^{5}5A1, the calculated bands are at 163, 198, 260, and 298 cm^{-1}; the final band is very close to the experimental band at 308 cm^{-1}, which is not seen in any other isomers. But the band corresponding to the calculated band at 163 cm^{-1} is not observed in the experimental spectrum. Finally, for structure ^{5}5A2, the experimental bands match the calculated ones, but the intensity distribution of the bands does not match. The calculated bands are at 157, 166, 191, 210, 262, and 295 cm^{-1}, and the band at 262 cm^{-1} is more intense than the others. Therefore, the structure of VCo_4^+ is most likely a distorted trigonal bipyramid with a triplet spin multiplicity, which is consistent with the previous assignment for Co_5^+ with a distorted trigonal bipyramidal structure.

5.4. Conclusions

The infrared spectra of cationic pure cobalt and vanadium-doped cobalt clusters are measured using far-infrared spectroscopy with argon as a messenger atom. The spectra of Co_n^+ clusters with sizes n=4-8 are in good agreement with the experimental spectra measured by Gehrke et al,[117] and the structures of Co_4^+ and Co_5^+ are assigned to a distorted tetrahedron and a distorted trigonal bipyramid, respectively. Replacing a cobalt atom with a vanadium atom in the Co_4^+ and Co_5^+ clusters does not change the IR spectrum drastically. The structures of VCo_3^+ and VCo_4^+ are elucidated by comparing the experimental spectra of VCo_3^+-Ar and VCo_4^+-Ar with the calculated spectra of different isomers. They are found to be a tetrahedron and a distorted trigonal bipyramid, respectively, which is not different from the pristine clusters. Therefore, including a vanadium atom in cobalt clusters does not alter the geometry of most cobalt clusters, apart from causing a shift in vibrational frequency. The increase in activity of vanadium-doped cobalt clusters compared to cobalt clusters most likely depends on a change in the electronic structure rather than their geometric structure.

6 Summary and outlook

The composition dependence of gas-phase metal clusters had not yet been experimentally explored in the context of CO_2 activation. Therefore, this thesis explored the bimetallic nature of the clusters and how they reacted when exposed to CO_2. The geometric structure of the clusters and cluster-CO_2 complexes was studied using infrared multiple photon dissociation spectroscopy in combination with density functional theory calculations.

Chapter 1 establishes the environmental context of the research, highlighting the urgent need to address rising atmospheric CO_2 levels through carbon capture and utilisation. Converting CO_2 into valuable chemicals like methanol is challenging due to the chemical inertness of the CO_2 molecule. This chapter introduces the gas-phase clusters as ideal model systems for studying these reactions, as they allow for precise control over size, charge and composition. The scope of the thesis is to investigate how doping cationic metal clusters with foreign atoms can facilitate CO_2 activation, a process usually seen only on anionic species.

Chapter 2 details the experimental and theoretical methods employed in the research. It begins with the fundamentals of infrared spectroscopy, detailing how molecular vibrations are modelled and detected through action spectroscopy techniques like infrared multiple photon dissociation (IRMPD) spectroscopy. The experimental section describes the FELICE molecular beam setup, where bimetallic clusters are produced via a dual-target dual-laser ablation source, reacted with molecules, irradiated with IR laser beam and detected using a reflectron time-of-flight mass spectrometer. The experimental results are complemented by density functional theory (DFT), which allows for the structural assignment of clusters and cluster-molecule complexes to understand the mechanisms for CO_2 activation.

Chapter 3 reports how the chemical activation of CO_2 can be achieved on cationic metal clusters, if they are modified with oxophilic dopants. The CO_2 adsorption on pure cationic cobalt clusters and vanadium-doped cobalt clusters has been studied. Experimental observations via infrared spectroscopy reveal that adsorption on pristine Co_n^+ clusters only leads to intact physisorption, in which the CO_2 molecule remains linear and weakly bound. However, Co_4^+ constitutes a unique exception, exhibiting a mixture of physisorbed and activated CO_2 species. The introduction of a single vanadium atom enables the clusters to activate or even dissociate the CO_2

molecule. Mass spectrometry and infrared spectroscopy reveal that VCo_3^+ and VCo_4^+ can fully dissociate CO_2, leading to CO elimination, whereas smaller complexes form stable O-VCo_n^+-CO complexes. These experimental findings are quantitatively supported by reaction pathway calculations, which confirm that the presence of vanadium significantly lowers the rate-limiting barrier for C-O bond cleavage. The results demonstrate that the oxophilic nature of the vanadium dopant is key to breaking the symmetry of the CO_2 molecule and facilitating its activation on a cationic center.

Building on the findings of the previous chapter, Chapter 4 examines the impact of different 3d transition metal dopants—iron, manganese, and chromium—on the activity of cobalt clusters. By measuring the infrared spectra of these various bimetallic complexes, the study aims to identify periodic trends in CO_2 activation. Iron doping of cobalt clusters does not affect their activity towards CO_2. However, a slight increase in activity is observed when a manganese atom is doped onto cobalt clusters, with one cluster size fully activating CO_2. Chromium doping on cobalt clusters increases the activity even better, enabling CO_2 dissociation in sizes such as $CrCo_2^+$ and $CrCo_4^+$. Density functional theory indicates that, for the Cr-doped system, the barrier is reduced to a level at which room-temperature thermal energy is sufficient to drive dissociation in a fraction of the cluster population. The results reveal that while several dopants influence the clusters, vanadium remains the most effective for promoting CO_2 activation among the tested elements. This systematic comparison helps elucidate how the electronic structure of the dopant dictates the chemical behaviour of the entire cluster.

Since vanadium performs well among the dopants discussed, Chapter 5 focuses on characterising the underlying geometric structures of the cationic bare and vanadium-doped cobalt clusters using far-infrared messenger tagging spectroscopy with argon. By comparing experimental spectra with theoretical predictions, the research identifies the lowest energy isomers for both pure and vanadium-doped cobalt clusters. The study assigns the geometries of Co_4^+ and Co_5^+ to a distorted tetrahedron and a distorted trigonal bipyramid based on the literature. Interestingly, the study concludes that substituting a cobalt atom with vanadium typically does not lead to a major geometric reorganisation. Instead, the dramatic shift in activity observed in earlier chapters is primarily attributed to changes in the electronic properties and the intrinsic oxophilicity provided by the vanadium site.

The work presented in this thesis demonstrates that CO_2 activation on transition-metal clusters can be significantly modified by changes in cluster composition, size,

and electronic structure. The results obtained for Co_n^+, VCo_n^+, $CrCo_n^+$, $MnCo_n^+$, and $FeCo_n^+$ show clear metal-dependent activity trends and further expand the current understanding of CO_2 interaction with cationic transition-metal clusters.

While several anionic clusters (Co_n^-, Pt_n^-, Rh_n^-, $AlRh_n^-$, CCu_n^-, OCu_n^-, $Mg_nO_m^-$) reported in the literature favour activated or dissociative adsorption over broad size ranges, the present cationic systems exhibit more selective size-dependent activity. These differences suggest that subtle changes in electronic structure strongly influence the cluster's ability to transfer charge to the antibonding orbitals of CO_2. Such findings demonstrate that controlled modification of the electronic structure through doping may provide an effective strategy for tuning catalytic activity.

Building on these results, one of the most important directions for future work is investigating subsequent hydrogenation reactions after the initial activation of CO_2. Although the present thesis focuses primarily on adsorption and activation, catalytic CO_2 conversion involves a complex network of elementary reaction steps. It would therefore be highly valuable to study the reactivity of the activated complexes toward hydrogen in order to identify intermediates relevant to methanol synthesis. In particular, future studies could focus on the formation of formate (HCOO), hydroxymethyl, formaldehyde-related, and methoxy (CH_3O) intermediates, which are frequently proposed in CO_2 hydrogenation pathways. Detecting such species under controlled gas-phase conditions would help establish direct mechanistic links between the activated adsorption structures identified in this work and industrially relevant catalytic cycles.

Another promising extension would involve time-resolved or kinetics-based investigations of the activation process. The present work identifies the adsorption products formed after reaction with CO_2, but the detailed reaction mechanisms and intermediates remain largely unexplored. Future experiments combining variable collision energies, temperature-dependent studies, or ion-trap approaches could provide insight into reaction barriers, intermediate lifetimes, and possible competing reaction channels. Complementary quantum-chemical calculations and reaction-pathway analyses could further clarify the transition states and electronic rearrangements involved in activation and bond cleavage.

A particularly relevant long-term perspective is the application of the present findings to copper-based catalytic systems. Copper remains one of the most important industrial catalysts for CO_2 hydrogenation to methanol, yet many details of the reaction mechanism remain unclear at the atomic scale. The gas-phase cluster

approach employed in this thesis provides a well-defined platform for isolating individual elementary reaction steps without the complexity of extended surfaces or supports. Applying the insights gained here to doped copper clusters may therefore improve understanding of how electronic modifications influence CO_2 activation and hydrogenation on industrially relevant catalysts. Such investigations may also help identify new dopant combinations capable of enhancing catalytic efficiency, selectivity, or stability.

Samenvatting

De afhankelijkheid van de elementaire samenstelling van metaalclusters op de activatie van CO_2 in de gasfase was nog niet experimenteel onderzocht. In dit proefschrift werd daarom onderzocht hoe CO_2 reageert wanneer het adsorbeert op bimetallische clusters. De geometrische structuren van de clusters en cluster-CO_2-complexen werd bestudeerd met behulp van infrarood fragmentatiespectroscopie in combinatie met berekeningen met dichtheidsfunctionaaltheorie (DFT).

Hoofdstuk 1 schetst de context van het onderzoek en benadrukt de dringende noodzaak om de stijgende atmosferische CO_2-concentraties aan te pakken door middel van koolstofafvang en -benutting. Het omzetten van CO_2 in waardevolle chemicaliën zoals methanol is een uitdaging vanwege de chemische inertheid van het CO_2-molecuul. Dit hoofdstuk introduceert geïsoleerde clusters als ideale modelsystemen voor het bestuderen van deze reacties, omdat hun gebruik een nauwkeurige controle over grootte, lading en elementaire samenstelling mogelijk maken. Meer specifiek wordt het onderwerp van dit proefschrift gedefinieerd als een onderzoek hoe het doteren van kationische metaalclusters met andere elementen de activering van CO_2 kan vergemakkelijken, een proces dat voor clusters van één enkel element gewoonlijk alleen wordt waargenomen voor anionische clusters.

Hoofdstuk 2 beschrijft de experimentele en theoretische methoden die in het onderzoek zijn gebruikt. Het begint met de grondbeginselen van infraroodspectroscopie, waarbij wordt uitgelegd hoe moleculaire vibraties worden gemodelleerd en gedetecteerd door middel van zogenaamde actiespectroscopie zoals infrarood-photodissociatiespectroscopie (IRMPD spectroscopie). Het experimentele gedeelte beschrijft de moleculaire bundelopstelling gekoppeld aan de FELICE vrije-elektronenlaser. In dit instrument worden positief geladen bimetallische clusters geproduceerd door middel van laserverdamping die na vorming reageren met CO_2 moleculen. Vervolgens worden ze bestraald met de infraroodlaser en gedetecteerd met behulp van een vluchttijdsmassaspectrometer. De experimentele resultaten worden geïnterpreteerd met behulp van DFT-berekeningen, die zowel de structuurbepaling van clusters en cluster-molecuulcomplexen als het begrip van de reactiemechanismen voor CO_2-activering mogelijk maken.

Hoofdstuk 3 beschrijft hoe CO_2 wordt geactiveerd door kationische metaalclusters mits deze zijn gedoteerd met oxofiele metaalelementen. Als voorbeeld wordt hier de adsorptiereactie van CO_2 op zowel zuivere als vanadium-gedoteerde kationische kobaltclusters bestudeerd. Experimentele waarnemingen met infraroodspectroscopie tonen aan dat adsorptie op zuivere kobaltclusters alleen leidt tot fysisorptie, waarbij het CO_2-molecuul zwak gebonden aan het clusteroppervlak is en zijn lineaire vorm behoudt. Co_4^+ vormt daarop een uitzondering omdat hier naast fysisorptie, ook indicaties voor geactiveerd CO_2 worden gezien. Het vervangen van een enkel kobaltatoom door een vanadiumatoom leidt bij de adsorptiereactie tot activatie van het CO2-molecuul of zelfs tot dissociatie. Massaspectrometrische metingen tonen aan dat CO_2 bij adsorptie op VCo_3^+ en VCo_4^+ volledig dissocieert waarbij het gevormde CO-molecuul wordt geëlimineerd. Infraroodspectroscopie toont dat de adsorptie van CO_2 op kleinere complexen leidt tot de vorming van stabiele O-VCo_n^+-CO-complexen. Deze experimentele bevindingen worden kwantitatief ondersteund door berekeningen van reactiepaden, die bevestigen dat de aanwezigheid van vanadium de snelheidsbeperkende reactiebarrière voor het breken van de C-O-binding significant verlaagt. De resultaten tonen aan dat het oxofiele karakter van het vanadiumatoom cruciaal is voor het activatieproces.

Voortbouwend op de bevindingen van het vorige hoofdstuk, wordt in hoofdstuk 4 de impact van andere 3d-overgangsmetaaldopanten – ijzer, mangaan en chroom – op de reactiviteit van kobaltclusters onderzocht. Door de infraroodspectra van het product van de adsorptiereactie van CO_2 op deze verschillende bimetallische complexen te meten, beoogt de studie periodieke trends in CO_2-activatie te identificeren. Het doteren van kobaltclusters met ijzeratomen heeft nauwelijks invloed op de reactiviteit van de kobaltclusters met CO_2. Er wordt echter een lichte toename in activiteit waargenomen wanneer een mangaanatoom aan kobaltclusters wordt toegevoegd, waarbij één specifieke clustergrootte CO_2 volledig activeert. Het doteren van kobaltclusters met chroom verhoogt de activiteit verder, waardoor CO_2-dissociatie mogelijk wordt bij groottes zoals $CrCo_2^+$ en $CrCo_4^+$. DFT berekeningen wijzen erop dat voor $CrCo_2^+$, in vergelijking met Co_3^+, de dissociatiereactiebarrière wordt verlaagd tot een niveau waarop de thermische energie bij kamertemperatuur voldoende is om dissociatie te bewerkstelligen in een fractie van de clusterpopulatie. De resultaten tonen aan dat, hoewel verschillende doteringselementen de reactiviteit van kobaltclusters beïnvloeden, onder de geteste elementen vanadium het effectiefst blijft in het bevorderen van CO_2-activatie. Deze systematische

vergelijking helpt te verduidelijken hoe de elektronische structuur van het doteringselement de reactieve eigenschappen van de gehele cluster bepaalt.

Omdat vanadium goed presteert onder de bestudeerde doteringselementen, richt hoofdstuk 5 zich op het karakteriseren van de onderliggende geometrische structuren van de kationische, ongedoteerde en met vanadium gedoteerde kobaltclusters met behulp van ver-infrarood spectroscopie. Hiertoe worden complexen van de clusters met één of meerdere argonatomen met infraroodlicht bestraalt, waar bij een resonance excitatie de argonatomen worden geëlimineerd. Door experimentele spectra te vergelijken met theoretische voorspellingen, identificeert het onderzoek de laagste-energie-isomeren voor zowel zuivere als met vanadium gedoteerde kobaltclusters. De studie kent op basis van de literatuur de geometrieën van Co_4^+ en Co_5^+ toe aan respectievelijk een vervormde tetraëder en een vervormde trigonale bipiramide. De vergelijking tussen experimentele spectra voor VCo_3^+ en VCo_4^+ en berekende spectra voor verschillende isomeren wijst erop dat dat het vervangen van een enkel kobaltatoom door een vanadiumatoom voor zowel Co_4^+ en Co_5^+ niet tot een grote geometrieverandering leidt. De drastische verandering in reactiviteit die in eerdere hoofdstukken werd waargenomen, moet daarom voornamelijk worden toegeschreven aan veranderingen in de elektronische eigenschappen die door het vanadiumatoom teweeggebracht worden.

Dit proefschrift belicht de succesvolle demonstratie van CO_2-activatie op kationische clusters door middel van dotering, en biedt mogelijke nieuwe routes voor het rationele ontwerp van nieuwe katalysatoren. Voortbouwend op de fundamentele inzichten die uit dit werk zijn verkregen, omvat de toekomstvisie het uitbreiden van dit onderzoek naar hydrogenatiereacties om voorlopers voor methanol te identificeren, zoals de vaak voorspelde formiaat- of methoxy-tussenproducten. Het is ook interessant om CO_2-activatie op zuivere en gedoteerde metaalclusters zonder lading te bestuderen en hun reactiviteit te vergelijken. Daarnaast is het toepassen van deze inzichten op kopergebaseerde systemen om industriële katalysatoren die worden gebruikt bij de CO_2-hydrogenatie tot methanol beter te begrijpen en te verbeteren.

References

(1) Houghton, J. T.; Meira Filho, L. G.; Griggs, D. J.; Maskell, K. *An introduction to simple climate models used in the IPCC Second Assessment Report*; WMO, **1997**.
(2) Deehan, M.; Renta, I.; Yaary, S.; Fillingham, J.; Sarkar, S.; Matlock, G.; Newcomb, L.; Bayler, E.; Ghirardelli, J.; Grasso, M. 2023 NOAA Science Report. **2024**.
(3) Keeling, C. D.; Bacastow, R. B.; Bainbridge, A. E.; Ekdahl, C. A.; Guenther, P. R.; Waterman, L. S.; Chin, J. F. S. Atmospheric carbon dioxide variations at Mauna Loa Observatory, Hawaii. *Tellus A: Dynamic Meteorology and Oceanography* **1976**, *28* (6), 538.
(4) Abdullatif, Y.; Sodiq, A.; Mir, N.; Bicer, Y.; Al-Ansari, T.; El-Naas, M. H.; Amhamed, A. I. Emerging trends in direct air capture of CO_2: a review of technology options targeting net-zero emissions. *RSC advances* **2023**, *13* (9), 5687-5722.
(5) Peres, C. B.; Resende, P. M.; Nunes, L. J.; Morais, L. C. d. Advances in carbon capture and use (CCU) technologies: a comprehensive review and CO_2 mitigation potential analysis. *Clean technologies* **2022**, *4* (4), 1193-1207.
(6) Olah, G. A.; Goeppert, A.; Prakash, G. S. *Beyond oil and gas: the methanol economy*; John Wiley & Sons, **2018**.
(7) Xie, S.; Zhang, Q.; Liu, G.; Wang, Y. Photocatalytic and photoelectrocatalytic reduction of CO_2 using heterogeneous catalysts with controlled nanostructures. *Chem. Commun.* **2016**, *52* (1), 35-59.
(8) Niquini, G. R.; Delgado, K. H.; Pitter, S.; Sauer, J. Kinetics of CO_2 hydrogenation to methanol on Cu/ZnO/ZrO_2 based on an extensive dataset. *Reaction Chemistry & Engineering* **2026**.
(9) Atkins, P. W.; De Paula, J.; Keeler, J. *Atkins' physical chemistry*; Oxford university press, **2023**.
(10) Somorjai, G. A.; Kliewer, C. J. Reaction selectivity in heterogeneous catalysis. *React. Kinet. Catal. Lett.* **2009**, *96* (2), 191-208.
(11) Zaera, F. Designing Sites in Heterogeneous Catalysis: Are We Reaching Selectivities Competitive With Those of Homogeneous Catalysts? *Chem. Rev.* **2022**, *122* (9), 8594-8757.
(12) Yang, B.; Chen, X.; Guo, L.; Zhang, L. Catalyst architecture for metal–support interactions and its effects on heterogeneous reactions. *J. Mater. Chem. A* **2024**, *12* (31), 19861-19884.
(13) Behrens, M.; Studt, F.; Kasatkin, I.; Kühl, S.; Hävecker, M.; Abild-Pedersen, F.; Zander, S.; Girgsdies, F.; Kurr, P.; Kniep, B.-L.; et al. The Active Site of Methanol Synthesis over Cu/ZnO/Al_2O_3 Industrial Catalysts. *Science* **2012**, *336* (6083), 893-897.
(14) Mikkelsen, M.; Jørgensen, M.; Krebs, F. C. The teraton challenge. A review of fixation and transformation of carbon dioxide. *Energy Environ. Sci.* **2010**, *3* (1), 43-81.

(15) Sun, J. T.; Metcalfe, I. S.; Sahibzada, M. Deactivation of $Cu/ZnO/Al_2O_3$ Methanol Synthesis Catalyst by Sintering. *Ind. Eng. Chem. Res.* **1999**, *38* (10), 3868-3872.
(16) Liang, B.; Ma, J.; Su, X.; Yang, C.; Duan, H.; Zhou, H.; Deng, S.; Li, L.; Huang, Y. Investigation on Deactivation of $Cu/ZnO/Al_2O_3$ Catalyst for CO_2 Hydrogenation to Methanol. *Ind. Eng. Chem. Res.* **2019**, *58* (21), 9030-9037.
(17) Kuld, S.; Thorhauge, M.; Falsig, H.; Elkjær, C. F.; Helveg, S.; Chorkendorff, I.; Sehested, J. Quantifying the promotion of Cu catalysts by ZnO for methanol synthesis. *Science* **2016**, *352* (6288), 969-974.
(18) Larmier, K.; Liao, W. C.; Tada, S.; Lam, E.; Verel, R.; Bansode, A.; Urakawa, A.; Comas-Vives, A.; Copéret, C. CO_2-to-Methanol Hydrogenation on Zirconia-Supported Copper Nanoparticles: Reaction Intermediates and the Role of the Metal–Support Interface. *Angew. Chem. Int. Ed.* **2017**, *56* (9), 2318-2323.
(19) Lam, E.; Larmier, K.; Wolf, P.; Tada, S.; Safonova, O. V.; Copéret, C. Isolated Zr surface sites on silica promote hydrogenation of CO_2 to CH_3OH in supported Cu catalysts. *Journal of the American Chemical Society* **2018**, *140* (33), 10530-10535.
(20) Ojelade, O. A.; Zaman, S. F. A Review on Pd Based Catalysts for CO_2 Hydrogenation to Methanol: In-Depth Activity and DRIFTS Mechanistic Study. *Catalysis Surveys from Asia* **2020**, *24* (1), 11-37.
(21) Xu, J.; Su, X.; Liu, X.; Pan, X.; Pei, G.; Huang, Y.; Wang, X.; Zhang, T.; Geng, H. Methanol synthesis from CO_2 and H_2 over $Pd/ZnO/Al_2O_3$: Catalyst structure dependence of methanol selectivity. *Applied Catalysis A: General* **2016**, *514*, 51-59.
(22) Fujitani, T.; Nakamura, J. The effect of ZnO in methanol synthesis catalysts on Cu dispersion and the specific activity. *Catal. Lett.* **1998**, *56* (2-3), 119-124.
(23) Bahruji, H.; Bowker, M.; Hutchings, G.; Dimitratos, N.; Wells, P.; Gibson, E.; Jones, W.; Brookes, C.; Morgan, D.; Lalev, G. Pd/ZnO catalysts for direct CO_2 hydrogenation to methanol. *J. Catal.* **2016**, *343*, 133-146.
(24) Studt, F.; Sharafutdinov, I.; Abild-Pedersen, F.; Elkjær, C. F.; Hummelshøj, J. S.; Dahl, S.; Chorkendorff, I.; Nørskov, J. K. Discovery of a Ni-Ga catalyst for carbon dioxide reduction to methanol. *Nature Chemistry* **2014**, *6* (4), 320-324.
(25) Zhong, J.; Yang, X.; Wu, Z.; Liang, B.; Huang, Y.; Zhang, T. State of the art and perspectives in heterogeneous catalysis of CO_2 hydrogenation to methanol. *Chem. Soc. Rev.* **2020**, *49* (5), 1385-1413.
(26) Liu, S.; He, Y.; Fu, W.; Chen, J.; Ren, J.; Liao, L.; Sun, R.; Tang, Z.; Mebrahtu, C.; Zeng, F. Hetero-site cobalt catalysts for higher alcohols synthesis by CO_2-hydrogenation: A review. *Journal of CO_2 Utilization* **2023**, *67*, 102322.
(27) Tu, J.; Wu, H.; Qian, Q.; Han, S.; Chu, M.; Jia, S.; Feng, R.; Zhai, J.; He, M.; Han, B. Low temperature methanation of CO_2 over an amorphous cobalt-based catalyst. *Chemical Science* **2021**, *12* (11), 3937-3943.
(28) Liang, C.; Tian, H.; Gao, G.; Zhang, S.; Liu, Q.; Dong, D.; Hu, X. Methanation of CO_2 over alumina-supported nickel or cobalt catalysts: Effects of the coordination between metal and support on formation of the reaction intermediates. *Int. J. Hydrogen Energy* **2020**, *45* (1), 531-543.

(29) Mafuné, F.; Wu, Y.; Yamaguchi, M.; Kudoh, S. Hydrogen Storage Capacity of Cobalt Cluster Ions. *J. Phys. Chem. A* **2024**, *128* (18), 3516-3528.
(30) Li, K.; Li, X.; Li, L.; Chang, X.; Wu, S.; Yang, C.; Song, X.; Zhao, Z.-J.; Gong, J. Nature of catalytic behavior of cobalt oxides for CO_2 hydrogenation. *Jacs Au* **2023**, *3* (2), 508-515.
(31) Díaz, J. A.; de la Osa, A. R.; Sánchez, P.; Romero, A.; Valverde, J. L. Influence of CO_2 co-feeding on Fischer–Tropsch fuels production over carbon nanofibers supported cobalt catalyst. *Catal. Commun.* **2014**, *44*, 57-61.
(32) Owen, R. E.; O'Byrne, J. P.; Mattia, D.; Plucinski, P.; Pascu, S. I.; Jones, M. D. Cobalt catalysts for the conversion of CO_2 to light hydrocarbons at atmospheric pressure. *Chem. Commun.* **2013**, *49* (99), 11683.
(33) He, Z.; Cui, M.; Qian, Q.; Zhang, J.; Liu, H.; Han, B. Synthesis of liquid fuel via direct hydrogenation of CO_2. *Proceedings of the National Academy of Sciences* **2019**, *116* (26), 12654-12659.
(34) Hwang, S.-M.; Han, S. J.; Park, H.-G.; Lee, H.; An, K.; Jun, K.-W.; Kim, S. K. Atomically Alloyed Fe–Co Catalyst Derived from a N-Coordinated Co Single-Atom Structure for CO_2 Hydrogenation. *ACS Catal.* **2021**, *11* (4), 2267-2278.
(35) Khodakov, A. Y.; Chu, W.; Fongarland, P. Advances in the Development of Novel Cobalt Fischer−Tropsch Catalysts for Synthesis of Long-Chain Hydrocarbons and Clean Fuels. *Chem. Rev.* **2007**, *107* (5), 1692-1744.
(36) He, X.; Wang, X.; Xu, H. Advancements in Cobalt-Based Catalysts for Enhanced CO_2 Hydrogenation: Mechanisms, Applications, and Future Directions: A Short Review. *Catalysts* **2024**, *14* (9), 560.
(37) Yang, Y.; Evans, J.; Rodriguez, J. A.; White, M. G.; Liu, P. Fundamental studies of methanol synthesis from CO_2 hydrogenation on Cu(111), Cu clusters, and Cu/ZnO(000$\bar{1}$). *Phys. Chem. Chem. Phys.* **2010**, *12* (33), 9909.
(38) Chorkendorff, I.; Niemantsverdriet, J. W. *Concepts of modern catalysis and kinetics*; John Wiley & Sons, **2017**.
(39) Kim, Y.; Trung, T. S. B.; Yang, S.; Kim, S.; Lee, H. Mechanism of the Surface Hydrogen Induced Conversion of CO_2 to Methanol at Cu(111) Step Sites. *ACS Catal.* **2016**, *6* (2), 1037-1044.
(40) Grabow, L.; Mavrikakis, M. Mechanism of methanol synthesis on Cu through CO_2 and CO hydrogenation. *ACS Catal.* **2011**, *1* (4), 365-384.
(41) Rodriguez, J. A.; Evans, J.; Feria, L.; Vidal, A. B.; Liu, P.; Nakamura, K.; Illas, F. CO_2 hydrogenation on Au/TiC, Cu/TiC, and Ni/TiC catalysts: Production of CO, methanol, and methane. *J. Catal.* **2013**, *307*, 162-169.
(42) Tang, Q.-L.; Hong, Q.-J.; Liu, Z.-P. CO_2 fixation into methanol at Cu/ZrO_2 interface from first principles kinetic Monte Carlo. *J. Catal.* **2009**, *263* (1), 114-122.
(43) Zhao, Y.-F.; Yang, Y.; Mims, C.; Peden, C. H.; Li, J.; Mei, D. Insight into methanol synthesis from CO_2 hydrogenation on Cu (1 1 1): Complex reaction network and the effects of H_2O. *J. Catal.* **2011**, *281* (2), 199-211.

(44) Kattel, S.; Liu, P.; Chen, J. G. Tuning Selectivity of CO_2 Hydrogenation Reactions at the Metal/Oxide Interface. *Journal of the American Chemical Society* **2017**, *139* (29), 9739-9754.
(45) Lu, Z.; Cheng, Y.; Li, S.; Yang, Z.; Wu, R. CO_2 thermoreduction to methanol on the MoS2-supported single Co atom catalyst: A DFT study. *Appl. Surf. Sci.* **2020**, *528*, 147047.
(46) Reber, A. C.; Khanna, S. N. Superatoms: Electronic and Geometric Effects on Reactivity. *Acc. Chem. Res.* **2017**, *50* (2), 255-263.
(47) Muetterties, E. L. Molecular Metal Clusters. *Science* **1977**, *196* (4292), 839-848.
(48) Hamilton, J. F.; Baetzold, R. C. Catalysis by Small Metal Clusters. *Science* **1979**, *205* (4412), 1213-1220.
(49) Sattler, K.; Mühlbach, J.; Recknagel, E. Generation of Metal Clusters Containing from 2 to 500 Atoms. *Phys. Rev. Lett.* **1980**, *45* (10), 821-824.
(50) Kappes, M. M.; Kunz, R. W.; Schumacher, E. Production of large sodium clusters (Na ,.x⩽65) by seeded beam expansions. *Chem. Phys. Lett.* **1982**, *91* (6), 413-418.
(51) Knight, W. D.; Clemenger, K.; de Heer, W. A.; Saunders, W. A.; Chou, M. Y.; Cohen, M. L. Electronic Shell Structure and Abundances of Sodium Clusters. *Phys. Rev. Lett.* **1984**, *52* (24), 2141-2143.
(52) Haruta, M.; Kobayashi, T.; Sano, H.; Yamada, N. Novel gold catalysts for the oxidation of carbon monoxide at a temperature far below 0 C. *Chem. Lett.* **1987**, *16* (2), 405-408.
(53) Haruta, M.; Yamada, N.; Kobayashi, T.; Iijima, S. Gold catalysts prepared by coprecipitation for low-temperature oxidation of hydrogen and of carbon monoxide. *J. Catal.* **1989**, *115* (2), 301-309.
(54) Luo, Z.; Castleman, A. W., Jr.; Khanna, S. N. Reactivity of Metal Clusters. *Chem. Rev.* **2016**, *116* (23), 14456-14492.
(55) de Heer, W. A. The physics of simple metal clusters: experimental aspects and simple models. *Rev. Mod. Phys.* **1993**, *65* (3), 611-676.
(56) Leybo, D.; Etim, U. J.; Monai, M.; Bare, S. R.; Zhong, Z.; Vogt, C. Metal–support interactions in metal oxide-supported atomic, cluster, and nanoparticle catalysis. *Chem. Soc. Rev.* **2024**, *53* (21), 10450-10490.
(57) Lang, S. M.; Bernhardt, T. M. Gas phase metal cluster model systems for heterogeneous catalysis. *Phys. Chem. Chem. Phys.* **2012**, *14* (26), 9255.
(58) Böhme, D. K.; Schwarz, H. Gas-Phase Catalysis by Atomic and Cluster Metal Ions: The Ultimate Single-Site Catalysts. *Angew. Chem. Int. Ed.* **2005**, *44* (16), 2336-2354.
(59) Kleis, J.; Greeley, J.; Romero, N. A.; Morozov, V. A.; Falsig, H.; Larsen, A. H.; Lu, J.; Mortensen, J. J.; Dułak, M.; Thygesen, K. S.; et al. Finite Size Effects in Chemical Bonding: From Small Clusters to Solids. *Catal. Lett.* **2011**, *141* (8), 1067-1071.
(60) Dietz, T. G.; Duncan, M. A.; Powers, D. E.; Smalley, R. E. Laser production of supersonic metal cluster beams. *J. Chem. Phys.* **1981**, *74* (11), 6511-6512.
(61) Bondybey, V. E.; English, J. H. Laser induced fluorescence of metal clusters produced by laser vaporization: Gas phase spectrum of Pb_2. *J. Chem. Phys.* **1981**, *74* (12), 6978-6979.

(62) Knickelbein, M. B. Reactions of transition metal clusters with small molecules. *Annu. Rev. Phys. Chem.* **1999**, *50* (1), 79-115.
(63) Loh, S.; Hales, D. A.; Lian, L.; Armentrout, P. Collision-induced dissociation of Fe_n^+ (n= 2–10) with Xe: Ionic and neutral iron binding energies. *J. Chem. Phys.* **1989**, *90* (10), 5466-5485.
(64) Weis, P.; Gilb, S.; Gerhardt, P.; Kappes, M. M. A time-of-flight, drift cell, quadrupole apparatus for ion mobility measurements. *Int. J. Mass spectrom.* **2002**, *216* (1), 59-73.
(65) Cheshnovsky, O.; Yang, S. H.; Pettiette, C. L.; Craycraft, M. J.; Smalley, R. E. Magnetic time-of-flight photoelectron spectrometer for mass-selected negative cluster ions. *Rev. Sci. Instrum.* **1987**, *58* (11), 2131-2137.
(66) Fielicke, A. Probing the binding and activation of small molecules by gas-phase transition metal clusters via IR spectroscopy. *Chem. Soc. Rev.* **2023**, *52* (11), 3778-3841.
(67) Liu, C.; Yang, B.; Tyo, E.; Seifert, S.; Debartolo, J.; Von Issendorff, B.; Zapol, P.; Vajda, S.; Curtiss, L. A. Carbon Dioxide Conversion to Methanol over Size-Selected Cu_4 Clusters at Low Pressures. *Journal of the American Chemical Society* **2015**, *137* (27), 8676-8679.
(68) Yang, B.; Liu, C.; Halder, A.; Tyo, E. C.; Martinson, A. B. F.; Seifert, S.; Zapol, P.; Curtiss, L. A.; Vajda, S. Copper Cluster Size Effect in Methanol Synthesis from CO_2. *J. Phys. Chem. C* **2017**, *121* (19), 10406-10412.
(69) Cai, X.; Li, G.; Hu, W.; Zhu, Y. Catalytic Conversion of CO_2 over Atomically Precise Gold-Based Cluster Catalysts. *ACS Catal.* **2022**, *12* (17), 10638-10653.
(70) Xiong, Y.; Chen, H.; Hu, Y.; Yang, S.; Xue, X.; He, L.; Liu, X.; Ma, J.; Jin, Z. Photodriven Catalytic Hydrogenation of CO_2 to CH_4 with Nearly 100% Selectivity over Ag_{25} Clusters. *Nano Lett.* **2021**, *21* (20), 8693-8700.
(71) Yang, D.; Pei, W.; Zhou, S.; Zhao, J.; Ding, W.; Zhu, Y. Controllable Conversion of CO_2 on Non-Metallic Gold Clusters. *Angew. Chem. Int. Ed.* **2020**, *59* (5), 1919-1924.
(72) Duncan, M. A. Infrared spectroscopy to probe structure and dynamics in metal ion-molecule complexes. *Int. Rev. Phys. Chem.* **2003**, *22* (2), 407-435.
(73) Weber, J. M. The interaction of negative charge with carbon dioxide – insight into solvation, speciation and reductive activation from cluster studies. *Int. Rev. Phys. Chem.* **2014**, *33* (4), 489-519.
(74) Lushchikova, O. V.; Szalay, M.; Tahmasbi, H.; Juurlink, L. B. F.; Meyer, J.; Höltzl, T.; Bakker, J. M. IR spectroscopic characterization of the co-adsorption of CO_2 and H_2 onto cationic Cu_n^+ clusters. *Phys. Chem. Chem. Phys.* **2021**, *23* (47), 26661-26673.
(75) Green, A. E.; Justen, J.; Schöllkopf, W.; Gentleman, A. S.; Fielicke, A.; Mackenzie, S. R. IR Signature of Size-Selective CO_2 Activation on Small Platinum Cluster Anions, Pt_n^- (n=4–7). *Angew. Chem. Int. Ed.* **2018**, *57* (45), 14822-14826.
(76) Yanagimachi, A.; Koyasu, K.; Valdivielso, D. Y.; Gewinner, S.; Schöllkopf, W.; Fielicke, A.; Tsukuda, T. Size-Specific, Dissociative Activation of Carbon Dioxide by Cobalt Cluster Anions. *J. Phys. Chem. C* **2016**, *120* (26), 14209-14215.

(77) Mikolaj, P.; Zamora Yusti, B.; Nyulászi, L.; Bakker, J. M.; Höltzl, T.; Lang, S. M. CO_2 activation by copper oxide clusters: size, composition, and charge state dependence. *Phys. Chem. Chem. Phys.* **2024**, *26* (36), 24126-24134.
(78) Zimmermann, N.; Bernhardt, T. M.; Bakker, J. M.; Barnett, R. N.; Landman, U.; Lang, S. M. Infrared Spectroscopy of Gas-Phase $Mn_xO_y(CO_2)_z^+$ Complexes. *J. Phys. Chem. A* **2020**, *124* (8), 1561-1566.
(79) Lushchikova, O. V.; Szalay, M.; Höltzl, T.; Bakker, J. M. Tuning the degree of CO_2 activation by carbon doping Cu_n^- (n=3–10) clusters: an IR spectroscopic study. *Faraday Discuss.* **2023**, *242*, 252-268.
(80) Liu, G.; Zhu, Z.; Marshall, M.; Blankenhorn, M.; Bowen, K. H. CO_2 Activation and Hydrogenation by Palladium Hydride Cluster Anions. *J. Phys. Chem. A* **2021**, *125* (8), 1747-1753.
(81) Iskra, A.; Gentleman, A. S.; Kartouzian, A.; Kent, M. J.; Sharp, A. P.; Mackenzie, S. R. Infrared Spectroscopy of Gas-Phase $M^+(CO_2)_n$ (M = Co, Rh, Ir) Ion–Molecule Complexes. *J. Phys. Chem. A* **2017**, *121* (1), 133-140.
(82) Johnson, G. E.; Priest, T.; Laskin, J. Coverage-Dependent Charge Reduction of Cationic Gold Clusters on Surfaces Prepared Using Soft Landing of Mass-Selected Ions. *J. Phys. Chem. C* **2012**, *116* (47), 24977-24986.
(83) Kattel, S.; Ramírez, P. J.; Chen, J. G.; Rodriguez, J. A.; Liu, P. Active sites for CO_2 hydrogenation to methanol on Cu/ZnO catalysts. *Science* **2017**, *355* (6331), 1296-1299.
(84) Ferrari, P.; Vanbuel, J.; Janssens, E.; Lievens, P. Tuning the Reactivity of Small Metal Clusters by Heteroatom Doping. *Acc. Chem. Res.* **2018**, *51* (12), 3174-3182.
(85) Alotaibi, T.; Alotaibi, M.; Alhawiti, F.; Aldosari, N.; Alsunaid, M.; Aldawas, L.; Qahtan, T. F.; Ismael, A. K. Tuning the Electronic Properties of Cu_mAg_n Bimetallic Clusters for Enhanced CO_2 Activation. *Int. J. Mol. Sci.* **2024**, *25* (22), 12053.
(86) Nonose, S.; Sone, Y.; Onodera, K.; Sudo, S.; Kaya, K. Structure and reactivity of bimetallic cobalt-vanadium (Co_nV_m) clusters. *J. Phys. Chem.* **1990**, *94* (7), 2744-2746.
(87) Bouwen, W.; Thoen, P.; Vanhoutte, F.; Bouckaert, S.; Despa, F.; Weidele, H.; Silverans, R. E.; Lievens, P. Production of bimetallic clusters by a dual-target dual-laser vaporization source. *Rev. Sci. Instrum.* **2000**, *71* (1), 54-58.
(88) Ferrari, P.; Vanbuel, J.; Li, Y.; Liao, T. W.; Janssens, E.; Lievens, P. The Double-Laser Ablation Source Approach. *Gas-Phase Synthesis of Nanoparticles* **2017**, 59-78.
(89) Truong, N. X.; Haertelt, M.; Jaeger, B. K.; Gewinner, S.; Schöllkopf, W.; Fielicke, A.; Dopfer, O. Characterization of neutral boron-silicon clusters using infrared spectroscopy: the case of Si_6B. *Int. J. Mass spectrom.* **2016**, *395*, 1-6.
(90) Nakajima, A.; Kishi, T.; Sugioka, T.; Sone, Y.; Kaya, K. Structure and reactivity of bimetallic cobalt-vanadium ($Co_nV_m^+$) cluster ions. *J. Phys. Chem.* **1991**, *95* (18), 6833-6835.
(91) Ferrari, P.; Molina, L. M.; Kaydashev, V. E.; Alonso, J. A.; Lievens, P.; Janssens, E. Controlling the Adsorption of Carbon Monoxide on Platinum Clusters by Dopant-Induced Electronic Structure Modification. *Angew. Chem.* **2016**, *128* (37), 11225-11229.

(92) De Haeck, J.; Veldeman, N.; Claes, P.; Janssens, E.; Andersson, M.; Lievens, P. Carbon Monoxide Adsorption on Silver Doped Gold Clusters. *J. Phys. Chem. A* **2011**, *115* (11), 2103-2109.
(93) Gruene, P.; Fielicke, A.; Meijer, G.; Janssens, E.; Ngan, V. T.; Nguyen, M. T.; Lievens, P. Tuning the geometric structure by doping silicon clusters. *ChemPhysChem* **2008**, *9* (5), 703-706.
(94) Bouwen, W.; Vanhoutte, F.; Despa, F.; Bouckaert, S.; Neukermans, S.; Theil Kuhn, L.; Weidele, H.; Lievens, P.; Silverans, R. E. Stability effects of $Au_nX_m^+$ (X=Cu, Al, Y, In) clusters. *Chem. Phys. Lett.* **1999**, *314* (3), 227-233.
(95) Tanaka, H.; Neukermans, S.; Janssens, E.; Silverans, R. E.; Lievens, P. σ Aromaticity of the Bimetallic Au_5Zn^+ Cluster. *Journal of the American Chemical Society* **2003**, *125* (10), 2862-2863.
(96) Hou, G. L.; Yang, T.; Li, M.; Vanbuel, J.; Lushchikova, O. V.; Ferrari, P.; Bakker, J. M.; Janssens, E. Water Splitting by C_{60}-Supported Vanadium Single Atoms. *Angew. Chem. Int. Ed.* **2021**, *60* (52), 27095-27101.
(97) Du, S.; Liu, X.; Liu, Z.; Li, G.; Fan, H.; Xie, H.; Jiang, L. Dinitrogen Activation by Heteronuclear Bimetallic Cluster Anion FeV^- in the Gas Phase. *JACS Au* **2023**, *3* (6), 1723-1727.
(98) Yamaguchi, M.; Kudoh, S.; Miyajima, K.; Lushchikova, O. V.; Bakker, J. M.; Mafuné, F. Tuning the Dissociative Action of Cationic Rh Clusters Toward NO by Substituting a Single Ta Atom. *J. Phys. Chem. C* **2019**, *123* (6), 3476-3481.
(99) Zhang, Y.; Yamaguchi, M.; Kawada, K.; Kudoh, S.; Lushchikova, O. V.; Bakker, J. M.; Mafuné, F. Adsorption Forms of NO on Iridium-Doped Rhodium Clusters in the Gas Phase Revealed by Infrared Multiple Photon Dissociation Spectroscopy. *J. Phys. Chem. A* **2022**, *126* (1), 36-43.
(100) van der Linden, M.; van Bunningen, A. J.; Amidani, L.; Bransen, M.; Elnaggar, H.; Glatzel, P.; Meijerink, A.; de Groot, F. M. F. Single Au Atom Doping of Silver Nanoclusters. *ACS Nano* **2018**, *12* (12), 12751-12760.
(101) Ticknor, B. W.; Bandyopadhyay, B.; Duncan, M. A. Photodissociation of Noble Metal-Doped Carbon Clusters. *J. Phys. Chem. A* **2008**, *112* (48), 12355-12366.
(102) Zamudio-Bayer, V.; Hirsch, K.; Ma, L.; De Knijf, K.; Xu, X.; Ławicki, A.; Terasaki, A.; Ferrari, P.; von Issendorff, B.; Lievens, P.; et al. Magnetic nanodoping: Atomic control of spin states in cobalt doped silver clusters. *Physical Review Research* **2023**, *5* (3), 033103.
(103) Szalay, M.; Buzsáki, D.; Barabás, J.; Faragó, E.; Janssens, E.; Nyulászi, L.; Höltzl, T. Screening of transition metal-doped copper clusters for CO_2 activation. *Phys. Chem. Chem. Phys.* **2021**, *23* (38), 21738-21747.
(104) Alvarez-Garcia, A.; Flórez, E.; Moreno, A.; Jimenez-Orozco, C. CO_2 activation on small Cu-Ni and Cu-Pd bimetallic clusters. *Molecular Catalysis* **2020**, *484*, 110733.
(105) Megha; Mondal, K.; Ghanty, T. K.; Banerjee, A. Adsorption and Activation of CO_2 on Small-Sized Cu–Zr Bimetallic Clusters. *J. Phys. Chem. A* **2021**, *125* (12), 2558-2572.

(106) Zamora, B.; Nyulászi, L.; Höltzl, T. CO_2 and H_2 Activation on Zinc-Doped Copper Clusters. *ChemPhysChem* **2023**.
(107) Swart, I.; Fielicke, A.; Rayner, D. M.; Meijer, G.; Weckhuysen, B. M.; de Groot, F. M. Controlling the Bonding of CO on Cobalt Clusters by Coadsorption of H_2. *Angew. Chem. Int. Ed.* **2007**, *46* (28), 5317-5320.
(108) Fisher, E. R.; Elkind, J. L.; Clemmer, D. E.; Georgiadis, R.; Loh, S. K.; Aristov, N.; Sunderlin, L. S.; Armentrout, P. B. Reactions of fourth-period metal ions (Ca^+–Zn^+) with O_2: Metal-oxide ion bond energies. *J. Chem. Phys.* **1990**, *93* (4), 2676-2691.
(109) Sode, O.; Keçeli, M.; Yagi, K.; Hirata, S. Fermi resonance in solid CO_2 under pressure. *J. Chem. Phys.* **2013**, *138* (7), 074501.
(110) Nosenko, V. V.; Rudko, G. Y.; Yaremko, A. M.; Yukhymchuk, V. O.; Hreshchuk, O. M. Anharmonicity and Fermi resonance in the vibrational spectra of a CO_2 molecule and CO_2 molecular crystal: Similarity and distinctions. *Journal of Raman Spectroscopy* **2018**, *49* (3), 559-568.
(111) Borisova, S.; Eremeev, S. V.; Rusina, G.; Stepanyuk, V.; Bruno, P.; Chulkov, E. V. Vibrations of small cobalt clusters on low-index surfaces of copper: Tight-binding simulations. *Phys. Rev. B* **2008**, *78* (7), 075428.
(112) McNary, C. P.; Armentrout, P. Iron cluster–CO bond energies from the kinetic energy dependence of the Fe_n^+(n= 4–17)+ CO association reactions. *Phys. Chem. Chem. Phys.* **2014**, *16* (48), 26467-26477.
(113) Black, J. G.; Yablonovitch, E.; Bloembergen, N.; Mukamel, S. Collisionless Multiphoton Dissociation of SF_6: A Statistical Thermodynamic Process. *Phys. Rev. Lett.* **1977**, *38* (20), 1131-1134.
(114) Oomens, J.; Moehlig, A. R.; Morton, T. H. Infrared Multiple Photon Dissociation (IRMPD) Spectroscopy of the Proton-Bound Dimer of 1-Methylcytosine in the Gas Phase. *J. Phys. Chem. Lett.* **2010**, *1* (19), 2891-2897.
(115) Polfer, N. C.; Oomens, J.; Dunbar, R. C. IRMPD spectroscopy of metal-ion/tryptophan complexes. *Phys. Chem. Chem. Phys.* **2006**, *8* (23), 2744.
(116) Fielicke, A.; Kirilyuk, A.; Ratsch, C.; Behler, J.; Scheffler, M.; von Helden, G.; Meijer, G. Structure Determination of Isolated Metal Clusters via Far-Infrared Spectroscopy. *Phys. Rev. Lett.* **2004**, *93* (2).
(117) Gehrke, R.; Gruene, P.; Fielicke, A.; Meijer, G.; Reuter, K. Nature of Ar bonding to small Co_n^+ clusters and its effect on the structure determination by far-infrared absorption spectroscopy. *J. Chem. Phys.* **2009**, *130* (3), 034306.
(118) Müller, F.; Sauer, J.; Song, X.; Asmis, K. R. The Chemical Nature of $Ti_4O_{10}^-$: Vibrational Predissociation Spectroscopy Combined with Global Structure Optimization. *J. Phys. Chem. A* **2021**, *125* (44), 9571-9577.
(119) Fielicke, A.; Ratsch, C.; von Helden, G.; Meijer, G. Isomer selective infrared spectroscopy of neutral metal clusters. *J. Chem. Phys.* **2005**, *122* (9), 091105.
(120) Newnam, B. E.; Early, J. W.; Lyman, J. L. Infrared FEL photochemistry: multiple-photon dissociation of Freon gas. *Nuclear Instruments and Methods in Physics Research Section A: Accelerators, Spectrometers, Detectors and Associated Equipment* **1994**, *341* (1-3), 142-145.

(121) Felker, P. M.; Zewail, A. H. Dynamics of intramolecular vibrational-energy redistribution (IVR). I. Coherence effects. *J. Chem. Phys.* **1985**, *82* (7), 2961-2974.
(122) Polfer, N. C.; Oomens, J. Vibrational spectroscopy of bare and solvated ionic complexes of biological relevance. *Mass Spectrom. Rev.* **2009**, *28* (3), 468-494.
(123) Bakker, J. M.; Lapoutre, V. J. F.; Redlich, B.; Oomens, J.; Sartakov, B. G.; Fielicke, A.; Von Helden, G.; Meijer, G.; Van Der Meer, A. F. G. Intensity-resolved IR multiple photon ionization and fragmentation of C_{60}. *J. Chem. Phys.* **2010**, *132* (7), 074305.
(124) Haertelt, M.; Lapoutre, V. J. F.; Bakker, J. M.; Redlich, B.; Harding, D. J.; Fielicke, A.; Meijer, G. Structure Determination of Anionic Metal Clusters via Infrared Resonance Enhanced Multiple Photon Electron Detachment Spectroscopy. *J. Phys. Chem. Lett.* **2011**, *2* (14), 1720-1724.
(125) Bondybey, V. E.; Smith, A. M.; Agreiter, J. New Developments in Matrix Isolation Spectroscopy. *Chem. Rev.* **1996**, *96* (6), 2113-2134.
(126) Wiley, W.; McLaren, I. H. Time-of-flight mass spectrometer with improved resolution. *Rev. Sci. Instrum.* **1955**, *26* (12), 1150-1157.
(127) Mamyrin, B.; Karataev, V.; Shmikk, D.; Zagulin, V. The mass-reflectron, a new nonmagnetic time-of-flight mass spectrometer with high resolution. *Zh. Eksp. Teor. Fiz* **1973**, *64* (1), 82-89.
(128) De Hoffmann, E.; Stroobant, V. *Mass spectrometry: principles and applications*; John Wiley & Sons, **2007**.
(129) Duncan, M. A. Invited Review Article: Laser vaporization cluster sources. *Rev. Sci. Instrum.* **2012**, *83* (4), 041101.
(130) Ready, J. *Effects of high-power laser radiation*; Elsevier, **2012**.
(131) Sengupta, T.; Das, S.; Pal, S. Transition Metal Doped Aluminum Clusters: An Account of Spin. *J. Phys. Chem. C* **2016**, *120* (18), 10027-10040.
(132) Hohenberg, P.; Kohn, W. Inhomogeneous electron gas. *Phys. Rev.* **1964**, *136* (3B), B864.
(133) Kohn, W.; Sham, L. J. Self-consistent equations including exchange and correlation effects. *Phys. Rev.* **1965**, *140* (4A), A1133.
(134) Tao, J.; Perdew, J. P.; Staroverov, V. N.; Scuseria, G. E. Climbing the Density Functional Ladder: Nonempirical Meta--Generalized Gradient Approximation Designed for Molecules and Solids. *Phys. Rev. Lett.* **2003**, *91* (14), 146401.
(135) Veszprémi, T.; Fehér, M. *Quantum chemistry: fundamentals to applications*; Springer Science & Business Media, **2012**.
(136) Johnson, G. E.; Mitrić, R.; Bonačić-Koutecký, V.; Castleman, A. W. Clusters as model systems for investigating nanoscale oxidation catalysis. *Chem. Phys. Lett.* **2009**, *475* (1-3), 1-9.
(137) Ye, J.; Dimitratos, N.; Rossi, L. M.; Thonemann, N.; Beale, A. M.; Wojcieszak, R. Hydrogenation of CO_2 for sustainable fuel and chemical production. *Science* **2025**, *387* (6737).
(138) *Gaussian 16 Rev. C.01*; Wallingford, CT, **2016**.
(139) Becke, A. D. Density-functional exchange-energy approximation with correct asymptotic behavior. *Phys. Rev. A* **1988**, *38* (6), 3098-3100.

(140) Hay, P. J.; Wadt, W. R. Ab initio effective core potentials for molecular calculations. Potentials for K to Au including the outermost core orbitals. *J. Chem. Phys.* **1985**, *82* (1), 299-310.
(141) Castro, M.; Salahub, D. R. Density-functional calculations for small iron clusters: Fe_n, Fe_n^+, and Fe_n^- for n≤5. *Phys. Rev. B* **1994**, *49* (17), 11842-11852.
(142) Facio-Muñoz, J. G.; Hernández-Velázquez, D. A.; Guzmán-Ramírez, G.; Flores-Moreno, R.; Rodríguez-Zavala, J. G.; Tenorio, F. J. Electronic structure and reactivity indexes of cobalt clusters, both pure and mixed with NO and N_2O (Co_n^q, q = 0, 1 and n = 4 − 9). *J. Mol. Model.* **2022**, *28* (7).
(143) Wang, Y.; Lv, J.; Zhu, L.; Ma, Y. CALYPSO: A method for crystal structure prediction. *Comput. Phys. Commun.* **2012**, *183* (10), 2063-2070.
(144) Eberhart, R.; Kennedy, J. A new optimizer using particle swarm theory. In *MHS'95. Proceedings of the sixth international symposium on micro machine and human science*, **1995**; Ieee: pp 39-43.
(145) Weigend, F.; Ahlrichs, R. Balanced basis sets of split valence, triple zeta valence and quadruple zeta valence quality for H to Rn: Design and assessment of accuracy. *Phys. Chem. Chem. Phys.* **2005**, *7* (18), 3297.
(146) Behn, A.; Zimmerman, P. M.; Bell, A. T.; Head-Gordon, M. Efficient exploration of reaction paths via a freezing string method. *J. Chem. Phys.* **2011**, *135* (22), 224108.
(147) Shimanouchi, T.; Matsuura, H.; Ogawa, Y.; Harada, I. J. J. o. P.; Data, C. R. Tables of molecular vibrational frequencies part 10. **1980**, *9* (4), 1149-1254.
(148) Green, A. E.; Gentleman, A. S.; Schöllkopf, W.; Fielicke, A.; Mackenzie, S. R. Atomic Cluster Au_{10}^+ Is a Strong Broadband Midinfrared Chromophore. *Phys. Rev. Lett.* **2021**, *127* (3).
(149) Kaw, K. A.; Louwerse, R. J.; Bakker, J. M.; Lievens, P.; Janssens, E.; Ferrari, P. Direct probing of low-energy intra d-band transitions in gas-phase cobalt clusters. *Commun. Chem* **2024**, *7* (1).
(150) Linstrom, P. J.; Mallard, W. G. The NIST Chemistry WebBook: A Chemical Data Resource on the Internet. *J. Chem. Eng. Data* **2001**, *46* (5), 1059-1063.
(151) Mina-Camilde, N.; Manzanares I, C.; Caballero, J. F. Molecular Constants of Carbon Monoxide at v = 0, 1, 2, and 3: A Vibrational Spectroscopy Experiment in Physical Chemistry. *J. Chem. Educ.* **1996**, *73* (8), 804.
(152) Olah, G. A. Towards Oil Independence Through Renewable Methanol Chemistry. *Angew. Chem. Int. Ed.* **2013**, *52* (1), 104-107.
(153) Artz, J.; Müller, T. E.; Thenert, K.; Kleinekorte, J.; Meys, R.; Sternberg, A.; Bardow, A.; Leitner, W. Sustainable Conversion of Carbon Dioxide: An Integrated Review of Catalysis and Life Cycle Assessment. *Chem. Rev.* **2018**, *118* (2), 434-504.
(154) Gregoire, G.; Duncan, M. A. Infrared spectroscopy to probe structure and growth dynamics in Fe^+-$(CO_2)_n$ clusters. *J. Chem. Phys.* **2002**, *117* (5), 2120-2130.
(155) Walker, N. R.; Grieves, G. A.; Walters, R. S.; Duncan, M. A. The metal coordination in $Ni^+(CO2)_n$ and $NiO_2^+(CO_2)_m$ complexes. *Chem. Phys. Lett.* **2003**, *380* (1-2), 230-236.

(156) Walker, N. R.; Walters, R. S.; Duncan, M. A. Infrared photodissociation spectroscopy of $V^+(CO_2)_n$ and $V^+(CO_2)_nAr$ complexes. *J. Chem. Phys.* **2004**, *120* (21), 10037-10045.
(157) Xing, X.-P.; Wang, G.-J.; Wang, C.-X.; Zhou, M.-F. Infrared Photodissociation Spectroscopy of $Ti^+(CO_2)_2Ar$ and $Ti^+(CO_2)_n$ (n=3–7) Complexes. *Chin. J. Chem. Phys.* **2013**, *26* (6), 687-687.
(158) Gregoire, G.; Brinkmann, N. R.; Van Heijnsbergen, D.; Schaefer, H. F.; Duncan, M. A. Infrared Photodissociation Spectroscopy of $Mg^+(CO_2)_n$ and $Mg^+(CO_2)_nAr$ Clusters. *J. Phys. Chem. A* **2003**, *107* (2), 218-227.
(159) Walters, R. S.; Brinkmann, N. R.; Schaefer, H. F.; Duncan, M. A. Infrared Photodissociation Spectroscopy of Mass-Selected $Al^+(CO_2)_n$ and $Al^+(CO_2)_nAr$ Clusters. *J. Phys. Chem. A* **2003**, *107* (38), 7396-7405.
(160) Jaeger, J.; Jaeger, T.; Brinkmann, N.; Schaefer, H.; Duncan, M. Infrared photodissociation spectroscopy of $Si^+(CO_2)_n$ and $Si^+(CO_2)_nAr$ complexes Evidence for unanticipated intracluster reactions. *Can. J. Chem.* **2004**, *82* (6), 934-946.
(161) Boese, A. D.; Schneider, H.; Glöß, A. N.; Weber, J. M. The infrared spectrum of $Au^-\cdot CO_2$. *J. Chem. Phys.* **2005**, *122* (15).
(162) Knurr, B. J.; Weber, J. M. Solvent-Driven Reductive Activation of Carbon Dioxide by Gold Anions. *Journal of the American Chemical Society* **2012**, *134* (45), 18804-18808.
(163) Knurr, B. J.; Weber, J. M. Structural diversity of copper–CO_2 complexes: infrared spectra and structures of $[Cu(CO_2)_n]^-$ clusters. *J. Phys. Chem. A* **2014**, *118* (44), 10246-10251.
(164) Knurr, B. J.; Weber, J. M. Interaction of nickel with carbon dioxide in $[Ni(CO_2)_n]^-$ clusters studied by infrared spectroscopy. *J. Phys. Chem. A* **2014**, *118* (38), 8753-8757.
(165) Knurr, B. J.; Weber, J. M. Infrared Spectra and Structures of Anionic Complexes of Cobalt with Carbon Dioxide Ligands. *J. Phys. Chem. A* **2014**, *118* (23), 4056-4062.
(166) Thompson, M. C.; Dodson, L. G.; Weber, J. M. Structural Motifs of $[Fe(CO_2)_n]^-$ Clusters (n = 3–7). *J. Phys. Chem. A* **2017**, *121* (21), 4132-4138.
(167) Walsh, A. D. 467. The electronic orbitals, shapes, and spectra of polyatomic molecules. Part II. Non-hydride AB2 and BAC molecules. *Journal of the Chemical Society (Resumed)* **1953**, 2266.
(168) Lang, S. M.; Bernhardt, T. M.; Bakker, J. M. On the Active Sites of Mg-bearing Interstellar Dust Grains: An Experimental and Theoretical Model Study of CO_2 Activation. *Astrophys. J.* **2026**, *999* (2), 154.
(169) Fujitani, T.; Nakamura, I.; Uchijima, T.; Nakamura, J. The kinetics and mechanism of methanol synthesis by hydrogenation of CO_2 over a Zn-deposited Cu (111) surface. *Surface Science* **1997**, *383* (2-3), 285-298.
(170) Nakamura, J. *Top. Catal.* **2003**, *22* (3/4), 277-285.
(171) Laudenschleger, D.; Ruland, H.; Muhler, M. Identifying the nature of the active sites in methanol synthesis over $Cu/ZnO/Al_2O_3$ catalysts. *Nat. Commun* **2020**, *11* (1).

(172) Amann, P.; Klötzer, B.; Degerman, D.; Köpfle, N.; Götsch, T.; Lömker, P.; Rameshan, C.; Ploner, K.; Bikaljevic, D.; Wang, H.-Y.; et al. The state of zinc in methanol synthesis over a Zn/ZnO/Cu(211) model catalyst. *Science* **2022**, *376* (6593), 603-608.
(173) Pradeep, D.; Yusti, B. Z.; Zijlstra, R. T.; Szalay, M.; Höltzl, T.; Nyulászi, L.; Bakker, J. M. Size-selective CO_2 activation by vanadium-doped cobalt clusters. *J. Phys. Chem. Lett.* **2026**, 17 (31), 9008-9015.
(174) Wang, L.; Wang, L.; Zhang, J.; Liu, X.; Wang, H.; Zhang, W.; Yang, Q.; Ma, J.; Dong, X.; Yoo, S. J.; et al. Selective Hydrogenation of CO_2 to Ethanol over Cobalt Catalysts. *Angew. Chem. Int. Ed.* **2018**, *57* (21), 6104-6108.
(175) Ferrari, P.; Hou, G.-L.; Lushchikova, O. V.; Calvo, F.; Bakker, J. M.; Janssens, E. The structures of cationic gold clusters probed by far-infrared spectroscopy. *Phys. Chem. Chem. Phys.* **2020**, *22* (20), 11572-11577.
(176) Epifanovsky, E.; Gilbert, A. T. B.; Feng, X.; Lee, J.; Mao, Y.; Mardirossian, N.; Pokhilko, P.; White, A. F.; Coons, M. P.; Dempwolff, A. L.; et al. Software for the frontiers of quantum chemistry: An overview of developments in the Q-Chem 5 package. *J. Chem. Phys.* **2021**, *155* (8), 084801.
(177) Wiesenfeld, J. M.; Stone, J.; Marcuse, D.; Burrus, C. A.; Yang, S. Temperature dependence of hydroxyl formation in the reaction of hydrogen with silica glass. *J. Appl. Phys.* **1987**, *61* (12), 5447-5454.
(178) Geng, L.; Cui, C.; Jia, Y.; Yin, B.; Zhang, H.; Sun, Z.-D.; Luo, Z. Reactivity of cobalt clusters $Co_n^{\pm/0}$ with dinitrogen: Superatom Co_6^+ and superatomic complex $Co_5N_6^+$. *J. Phys. Chem. A* **2021**, *125* (10), 2130-2138.
(179) Barabás, J.; Ferrari, P.; Kaydashev, V.; Vanbuel, J.; Janssens, E.; Höltzl, T. The effect of size, charge state and composition on the binding of propene to yttrium-doped gold clusters. *RSC Advances* **2021**, *11* (47), 29186-29195.
(180) Barabás, J.; Höltzl, T. Reaction of N_2O and CO Catalyzed with Small Copper Clusters: Mechanism and Design. *J. Phys. Chem. A* **2016**, *120* (44), 8862-8870.
(181) Hou, G. L.; Faragó, E.; Buzsáki, D.; Nyulászi, L.; Höltzl, T.; Janssens, E. Observation of the Reaction Intermediates of Methanol Dehydrogenation by Cationic Vanadium Clusters. *Angew. Chem. Int. Ed.* **2021**, *60* (9), 4756-4763.
(182) Reider, A. M.; Szalay, M.; Reichegger, J.; Barabás, J.; Schmidt, M.; Kappe, M.; Höltzl, T.; Scheier, P.; Lushchikova, O. V. Spectroscopic investigation of size-dependent CO_2 binding on cationic copper clusters: analysis of the CO_2 asymmetric stretch. *Phys. Chem. Chem. Phys.* **2024**, *26* (30), 20355-20364.
(183) Luo, Y.-R. *Comprehensive handbook of chemical bond energies*; CRC press, **2007**.
(184) Alonso, J. A. Electronic and Atomic Structure, and Magnetism of Transition-Metal Clusters. *Chem. Rev.* **2000**, *100* (2), 637-678.
(185) Nakamura, J.; Choi, Y.; Fujitani, T. On the Issue of the Active Site and the Role of ZnO in Cu/ZnO Methanol Synthesis Catalysts. *Top. Catal.* **2003**, *22* (3-4), 277-285.
(186) Knickelbein, M. B. Magnetic moments of bare and benzene-capped cobalt clusters. *J. Chem. Phys.* **2006**, *125* (4).

(187) Jia, M.; Van Der Tol, J.; Li, Y.; Chernyy, V.; Bakker, J. M.; Pham, L. N.; Nguyen, M. T.; Janssens, E. Structures and magnetic properties of small Co_n^+ and $Co_{n-1}Cr^+$ (n = 3–5) clusters. *J. Phys.: Condens. Matter* **2018**, *30* (47), 474002.
(188) Pradeep, D.; Szalay, M.; Höltzl, T.; Nyulászi, L.; Bakker, J. M. IR spectroscopy of cationic MCo_n^+–CO_2 (M=Fe, Mn, Cr; n=2-7) cluster complexes. in preparation.
(189) Weis, P. Structure determination of gaseous metal and semi-metal cluster ions by ion mobility spectrometry. *Int. J. Mass spectrom.* **2005**, *245* (1-3), 1-13.
(190) Weis, P.; Bierweiler, T.; Gilb, S.; Kappes, M. M. Structures of small silver cluster cations (Ag_n^+, n< 12): ion mobility measurements versus density functional and MP2 calculations. *Chem. Phys. Lett.* **2002**, *355* (3-4), 355-364.
(191) Furche, F.; Ahlrichs, R.; Weis, P.; Jacob, C.; Gilb, S.; Bierweiler, T.; Kappes, M. M. The structures of small gold cluster anions as determined by a combination of ion mobility measurements and density functional calculations. *J. Chem. Phys.* **2002**, *117* (15), 6982-6990.
(192) Schooss, D.; Blom, M. N.; Parks, J. H.; Issendorff, B. v.; Haberland, H.; Kappes, M. M. The structures of Ag_{55}^+ and Ag_{55}^-: trapped ion electron diffraction and density functional theory. *Nano Lett.* **2005**, *5* (10), 1972-1977.
(193) Terasaki, A.; Majima, T.; Kasai, C.; Kondow, T. Photon-trap spectroscopy of size-selected free cluster ions: “direct” measurement of optical absorption of Ag_9^+. *Eur. Phys. J. D* **2009**, *52* (1-3), 43-46.
(194) Polfer, N. C. Infrared multiple photon dissociation spectroscopy of trapped ions. *Chem. Soc. Rev.* **2011**, *40* (5), 2211-2221.
(195) Oomens, J.; Sartakov, B. G.; Meijer, G.; von Helden, G. Gas-phase infrared multiple photon dissociation spectroscopy of mass-selected molecular ions. *Int. J. Mass spectrom.* **2006**, *254* (1-2), 1-19.
(196) Gruene, P.; Rayner, D. M.; Redlich, B.; Van Der Meer, A. F. G.; Lyon, J. T.; Meijer, G.; Fielicke, A. Structures of Neutral Au_7, Au_{19}, and Au_{20} Clusters in the Gas Phase. *Science* **2008**, *321* (5889), 674-676.
(197) Lushchikova, O. V.; Huitema, D. M. M.; López-Tarifa, P.; Visscher, L.; Jamshidi, Z.; Bakker, J. M. Structures of Cu_n^+ (n =3−10) Clusters Obtained by Infrared Action Spectroscopy. *J. Phys. Chem. Lett.* **2019**, *10* (9), 2151-2155.
(198) Claes, P.; Janssens, E.; Ngan, V. T.; Gruene, P.; Lyon, J. T.; Harding, D. J.; Fielicke, A.; Nguyen, M. T.; Lievens, P. Structural Identification of Caged Vanadium Doped Silicon Clusters. *Phys. Rev. Lett.* **2011**, *107* (17), 173401.
(199) Minemoto, S.; Terasaki, A.; Kondow, T. Electronic structures of cobalt cluster cations: Photodissociation spectroscopy of Co_n^+Ar (n=3–5) in the visible to near-infrared range. *J. Chem. Phys.* **1996**, *104* (15), 5770-5775.
(200) Yoshida, H.; Terasaki, A.; Kobayashi, K.; Tsukada, M.; Kondow, T. Spin-polarized electronic structure of cobalt cluster anions studied by photoelectron spectroscopy. *J. Chem. Phys.* **1995**, *102* (15), 5960-5965.
(201) Tung, N. T.; Janssens, E.; Bhattacharyya, S.; Lievens, P. Photofragmentation of mass-selected vanadium doped cobalt cluster cations. *Eur. Phys. J. D* **2013**, *67* (2).

(202) Pramann, A.; Koyasu, K.; Nakajima, A.; Kaya, K. Anion Photoelectron Spectroscopy of Vanadium-Doped Cobalt Clusters. *J. Phys. Chem. A* **2002**, *106* (11), 2483-2488.
(203) Neese, F.; Wennmohs, F.; Becker, U.; Riplinger, C. The ORCA quantum chemistry program package. *J. Chem. Phys.* **2020**, *152* (22).
(204) de Souza, B. GOAT: A Global Optimization Algorithm for Molecules and Atomic Clusters. *Angew. Chem. Int. Ed.* **2025**, *64* (18), e202500393.

Research data management

This thesis research has been carried out following the research data management policy of HFML-FELIX and Radboud University, the Netherlands.

Data sets for the results presented in the research chapters of this thesis are available at the Radboud Data Repository. The data sets are available at the following URL: https://doi.org/10.34973/jkwc-gf82.

List of Publications

- **Size-selective CO_2 activation by vanadium-doped cobalt clusters**
  Pradeep, D.; Yusti, B. Z.; Zijlstra, R. T.; Szalay, M.; Höltzl, T.; Nyulászi, L.; Bakker, J. M.
  J. Phys. Chem. Lett., 17 (31), 9008-9015 (2026)
  doi: 10.1021/acs.jpclett.6c01792

- **IR spectroscopy of cationic MCo_n^+–CO_2 (M=Fe, Mn, Cr; n=2-7) cluster complexes**
  Pradeep, D.; Szalay, M.; Höltzl, T.; Nyulászi, L.; Bakker, J. M.
  in preparation

- **Far-infrared spectroscopy of cationic vanadium-doped cobalt clusters**
  Pradeep, D.; Ferrari, P.; Yusti, B. Z.; Höltzl, T.; Bakker, J. M.
  in preparation

- **IR spectroscopic characterization of products of methane and cyclopropane activation by Ru cations**
  Wensink, F. J.; Pradeep, D.; Armentrout, P.; Bakker, J. M.
  Int. J. Mass spectrom., 495, 117165 (2024)
  doi: 10.1016/j.ijms.2023.117165

- **Resolving spin state discrepancies of small cationic iron clusters by far-infrared vibrational spectroscopy**
  Kaw, K. A.; Lacinbala, O.; Pradeep, D.; Bakker, J. M.; Janssens, E.; Lievens, P.; Ferrari, P.
  Phys. Rev. Lett. 137, 013002 (2026)
  doi: 10.1103/sqvn-3n9g

- **Vibrational spectroscopy, structure and bonding in the family of aluminium-doped niobium clusters, $AlNb_n^+$, n = 5–9**
  Singh, R.; Ferrari, P.; Pradeep, D.; Bakker, J. M.; Fielicke, A.; Janssens, E.; Lievens, P.; McGrady, J. E.
  Phys. Chem. Chem. Phys. 28 (30): 18541–18552 (2026)
  doi: 10.1039/d6cp01125j

Acknowledgements

This thesis would not have been possible without the support, guidance, and encouragement of many people, to whom I owe a great debt of gratitude.

First and foremost, I am deeply grateful to my supervisor, Joost, for his unwavering guidance, intellectual generosity, and patient mentorship throughout this journey. He gave me the freedom to explore and work independently in the lab, while always remaining open to my questions, no matter how basic, which made me feel at ease and helped me grow as a researcher. His insightful feedback and thoughtful questions have shaped both this work and my development as a researcher. I am also deeply grateful to my co-supervisor, Piero, who, despite formally taking on this role only last year, has been a guiding presence from the very start, contributing to lab work, scientific discussions, and theoretical calculations, and offering feedback and comments on this thesis that have meaningfully shaped this research. I am sincerely grateful to Andrei, Head of our Condensed Matter Physics group, who guided me from the very beginning, from the initial interview panel through to annual evaluations, providing consistent support and feedback throughout my PhD.

My gratitude also extends to my collaborators and thesis committee. Tibor and László, thank you for your theoretical support in interpreting our experimental findings, for many meaningful scientific discussions, and for introducing me to DFT during my secondment at BME. Sandra, thank you for teaching me kinetics during my secondment at Ulm University and for the stimulating discussions during shifts at FELIX. Ewald, thank you for generously hosting me during my secondment at KU Leuven and for the opportunity to join the CATCHY network. I am grateful to Sandra, Ewald, and Hans for also serving on my thesis committee. Their time, expertise, and constructive critiques significantly strengthened this dissertation.

I would like to extend my heartfelt thanks to all the technicians at HFML-FELIX, without whom this work would simply not have been possible. Arjan, thank you for all the mechanical work, the help with Inventor, and for always being the go-to person I could count on. You never once made me feel silly for asking what must have seemed like very basic questions, and that meant more than you know. Bryan, thank you for handling all things electronic, for teaching me to solder and wire, and for doing it all with such warmth. René, thank you for guiding me through the vacuum systems, teaching me to clean pressure gauges, and managing the liquid

helium orders. Together, Arjan, Bryan, and René were a constant, friendly presence that made the lab feel like a welcoming place from day one. Victor, thank you for all the software support and for the clever touch of integrating the liquid helium readings into Telegram, which saved me more than a few unnecessary trips to the lab. Thijs from Technocentrum, thank you for crafting the cluster source parts with such skill; Marcel, for fixing the gas valve controller at just the right moment; Frits, for faithfully delivering helium to keep the magnets cold; Paul, for the careful technical drawings; and Lijnis, for filing the new metal targets. A special thank you to René, Bryan, Paul, Victor, Wouter, Michel, Bouke, and Reza for providing the wonderful light from FELICE that was central to this work. I also want to thank Guus, Marije, Max, Lex, and Bas for their broader technical support throughout. The technicians at HFML-FELIX gave me not just a functioning experiment, but a real appreciation for the craft and dedication that underpin every scientific result.

I would also like to thank the other PIs at HFML-FELIX for their kindness and collegiality. Jos, you are simply one of the happiest people I have ever met, and your cheerful presence always brightened the day. Giel, thank you for the great conversations and for taking the time to give me laser safety instructions. Sandra, thank you for the many shared gaskets and gas bottles, the small acts of generosity that keep a lab running. Carl, our chats about liquid helium and the FELICE table position may have seemed technical, but they were always a pleasure. I would also like to thank Nils and Jonathan for helping make FELIX such a good place to work.

The wonderful office team at HFML-FELIX deserves equal recognition for keeping everything running smoothly behind the scenes. Thera and Ineke, thank you for organising events and handling all the paperwork so cheerfully. A special thank you to Erna, our former secretary, for arranging accommodation and making my arrival so much easier. I am grateful to our former director, Britta, for her genuine care for everyone's well-being at the institute, and to our current director, Marc, for making HFML-FELIX such a wonderful place to work. I also extend my gratitude to all the current and former office team members I may not have mentioned by name. Your support was felt and deeply appreciated.

I would also like to thank the CATCHY network for making this journey so much more enjoyable. Barbara and Pavol, thank you for the fun conversations during secondments and shifts, and for your help and support throughout my research. Your company made even the long days at FELIX something to look forward to. A

special thank you to Máté for the DFT support, for his help during the shifts, and for being such a wonderful host during my visit to Budapest. Working alongside Kevin, Yufei, and Bart at KU Leuven was a real pleasure, and sharing shifts together at FELIX made those long days all the more enjoyable. To Deema, Esperanza, Bao, Dimitra, Filippo, Imran, João, Maximilian, Wenjian, and Sumant, thank you for all the laughter and good memories shared during CATCHY meetings and conferences around Europe. A special mention to Waqas, who started this journey at the same time as me. You were incredibly helpful during that uncertain first year, and having you by my side at every CATCHY event made the whole experience so much warmer and more fun. I am lucky to have shared this network with all of you.

I would also like to thank all my colleagues at HFML-FELIX who made this journey so memorable. Frank, thank you for all the hours we spent filling liquid helium and nitrogen together, and for always being there. Olga D, sharing an office with you from nearly the very beginning was a joy. You are fun, caring, and generous, and I will always be grateful for your help and for the plants! Rick, thank you for patiently teaching me how to work with the FELIX cluster machine. You gave me the foundation I needed. Laura W, we joined forces on the cluster machine as learners together, and I really valued figuring things out side by side. Rutger, you were a great master's student; you learned quickly, helped resolve the stability issue with the cluster source, and I am so glad you later joined our group. I would also like to thank my office mates Maxime, Aravindh, Niels, Maarten, Michiel, and Sanne for making our shared space such a pleasant place to be. Maarten, our conversations about chess and survival running were always a highlight of the day, and thank you for teaching me a little Dutch along the way. Niels, thank you for your warm and fun presence, for the spicy Korean noodles, and for bringing the coffee machine into the office, a contribution that benefited everyone more than you probably realise. Thanks also to Bastiaan for the great talks about cooking, and to Teun and Jelle for making the "Illuminati" song a beloved part of FELIX culture. Laura F, thank you for the yoga classes that gave us all a chance to breathe; Thom, for your help with Inventor, and for sharing FELICE with me for a while; and Dian, for the fascinating conversations about liquid nitrogen. Olga L, I began my PhD by reading your thesis, and I am glad you later joined our group as a researcher. I would also like to thank Lara, Matthias, Kim, Julianna, Pavel, Kas, Daniel, Daniël, Rianna, Héloïse, Marius, Vera, Takeshi, Jens, Kilian, Rick, Lorena, Prateek, Long, Alexander, Tomasz, Justyna, Noël, Sara, and all other colleagues at HFML-FELIX whose names I may not have

mentioned, for making HFML-FELIX such a warm and welcoming place to work every day.

A heartfelt thank you to Aravindh, Hunar, and Priyanka for making me feel at home, even though I'm so far from home. We shared so many dinners and movie nights together that became some of my fondest memories outside the lab. What I treasure most is that we each carried a different piece of India with us — I speak Malayalam, Aravindh Tamil, Priyanka Marathi, and Hunar Punjabi — yet despite coming from different corners of the country, together we created a warmth and familiarity that made the distance from home feel so much smaller.

I would also like to thank my friends in Nijmegen and across the Netherlands for giving me a life outside the PhD. Devaraj, Krishna, Nikhila, and Merin, thank you for all the fun we had together. You made Nijmegen feel like home. Dipanshu, Priyanshu, and Souvik, thank you for the small talks during lunch breaks that always gave me a moment to breathe and recharge. To Harith, Aghil, Deepak and Rahul, thank you for always being there whenever I needed you. To Gokul, Premjith, Sam, Archith, and all other friends further afield, thank you for all the fun and laughter we shared whenever we got together. A special mention to Aswan, my companion from our master's days. Thank you for making the journey all the way from Hamburg to visit me; those visits always felt like a little piece of home.

Finally, on a personal note, I am profoundly thankful to my family, whose unconditional love, patience, and belief in me have been my bedrock throughout this journey. To my friends, thank you for reminding me of life beyond the thesis.

Curriculum Vitae

Deepak Pradeep

05-01-1997 Born in Kottayam, Kerala, India.

Education

2021 – 2025 PhD candidate in Experimental Molecular Physics
HFML-FELIX Laboratory, Radboud University,
Nijmegen, The Netherlands

2015 – 2020 Bachelor's and Master's in Photonics (dual-degree),
International School of Photonics,
Cochin University of Science & Technology,
Cochin, Kerala, India

2012 – 2014 Higher Secondary School,
Gayathri Central School,
Kottayam, Kerala, India

